THESIS FOR THE DEGREE OF DOCTOR OF PHILOSOPHY

Modification of microcapsules for controlled release

Markus Andersson Trojer

CHALMERS

Department of Chemical and Biological Engineering

CHALMERS UNIVERSITY OF TECHNOLOGY

Göteborg, Sweden 2012

Modification of microcapsules for controlled release

Markus Andersson Trojer

ISBN: 978-91-7385-666-9

Doktorsavhandlingar vid Chalmers Tekniska Högskola

Ny Serie Nr: 3347

ISSN: 0346-718X

Department of Chemical and Biological Engineering

Chalmers University of Technology

SE-412 96

Sweden

Telephone +46 (0)31-772 1000

Cover: A SEM image of a microcapsule with schematic modifications

Printed by:

Chalmers Reproservice

Göteborg, Sweden 2012

Modification of microcapsules for controlled release

Markus Andersson Trojer

Department of Chemical and Biological Engineering

Chalmers University of Technology

Abstract

Fouling of marine organisms such as algae and barnacles on the boat hull is an enormous problem for the shipping industry. The negative consequences for the society are both economic and environmental. To prevent fouling in general, biocides are typically incorporated directly into the paint. Premature leakage of the biocides is a drawback which reduces the lifetime of the coating and pollutes the surrounding ecosystems.

Microencapsulation is an efficient way of encapsulating active substances for controlling the release and thereby prolonging the antifouling properties of the coating. The microcapsules used in this work consist of an oil core and a hydrophobic polymer shell. The rate of release into the marine environment may be further tailored by modifying the microcapsules. *Triggered release* is achieved by rendering the microcapsule shell water sensitive. This may be accomplished by incorporating salt into the shell using imidazole coordination chemistry. On the other hand, *extended release* is achieved by improving the barrier properties of the microcapsule. This may be realized by providing the microcapsule with an additional shell, such as a highly charged polyelectrolyte multilayer or a lipid bilayer.

The objective of this thesis is subsequently twofold: 1) To synthesize and characterize imidazole containing shell materials with a view to obtain triggered release. 2) To surface modify microcapsules with polyelectrolyte multilayers and lipid bilayers toward extended release.

Imidazole containing polymers were synthesized using vinyl and maleimide radical polymerization, as well as *grafting* techniques comprising maleimide bond formation and epoxide ring opening. The imidazole-containing polymeric materials, with and without the salts $CuCl_2$ or $ZnCl_2$, were characterized using differential scanning calorimetry, electron paramagnetic resonance (EPR) and vibrational spectroscopy. The coordination chemistry of the imidazole-metal ion complex was investigated using vibrational spectroscopy, EPR and *ab initio* calculations.

The imidazole coordination to the transition metal ions Cu^{2+} and Zn^{2+} in polymeric materials generates cross-links. The interaction between the imidazole moiety and the transition metal ions is very strong and specific. As a consequence, the coordinating polymer is rendered insoluble in conventional solvents, excluding only strongly coordinating solvents.

The specificity and strength of the imidazole-transition metal ion interaction may be used for a variety of applications. However, with respect to the microencapsulation route used in this project, the limited solubility of the coordinating polymer material is unfortunate. The use of strongly coordinating solvents during the microencapsulation results in aggregation and phase separation instead of microcapsule formation.

Routes for synthesising highly charged microcapsules for further surface modification were investigated using three types of ionic dispersants; a weak polyacid, a small set of amphiphilic block copolymers and a hydrophobic anionic surfactant in combination with a polycation. The charged microcapsules were subsequently modified with polyelectrolyte multilayers using the Layer-by-Layer technique and with lipid bilayers using lipid vesicle spreading. The microcapsules and model systems thereof were characterized mainly using micro-electrophoresis, light microscopy, optical tensiometry and quartz crystal microbalance with dissipation (QCM-D). The release behaviour in aqueous suspension of a hydrophobic model compound was investigated using UV-Vis spectroscopy.

The use of the ionic dispersants facilitated the formation of highly charged microcapsules and the subsequent polyelectrolyte multilayer assembly and lipid bilayer formation were also successful. In particular, the block copolymer based microcapsules displayed excellent properties with respect to high and stable surface charge, as well as long term colloidal stability through electrostatic and steric stabilization. The release of the hydrophobic model compound was considerably reduced after modification with polyelectrolyte multilayers. In addition, the type of dispersant had a significant impact on the release. The block copolymer based microcapsules with a higher charge density had a much lower release compared to the weak polyelectrolyte based microcapsules.

The polyelectrolyte multilayer is an efficient barrier against hydrophobic molecules and the low permeability is clearly a result of the high charge density. The polyelectrolyte multilayer assembly is a versatile process and the permeability of the multilayer may therefore be tailored according to the need. As of yet, the effect of the lipid bilayers on the release has not been investigated but has a large potential since the permeability may be altered by the lipid composition. A microcapsule consisting of an oil core, a hydrophobic polymer shell, a polyelectrolyte multilayer and a lipid bilayer is a complex release system with large degrees of freedom for tailoring the release behaviour.

Keywords; Microcapsule, imidazole, coordination chemistry, cross-linking, vibrational spectroscopy, electron paramagnetic resonance, quartz crystal microbalance with dissipation monitoring, polyelectrolyte multilayer, block copolymer, colloidal stability, controlled release

List of Papers

I Vinylimidazole copolymers: coordination geometry, solubility and cross-linking as function of Cu^{2+} and Zn^{2+} complexation

Markus Andersson, Örjan Hansson, Lars Öhrström, Alexander Idström and Magnus Nydén

Colloid and Polymer Science **2011***,* 289(12), 1361-1372

II Coordination of Imidazoles by Cu(II) and Zn(II) as Studied by NMR Relaxometry, EPR, Far-FTIR Vibrational Spectroscopy and Ab Initio Calculations: Effect of Methyl Substitution

Markus Andersson, Jesper Hedin, Patrik Johansson, Jonas Nordström and Magnus Nydén

Journal of Physical Chemistry A **2010***,* 114(50), 13146-13153

III Synthesis and polymerisation of maleoyl-L-histidine monomers and addition of histidine to an ethylene-alt-maleic co-polymer.

Markus Andersson Trojer, Dan Isaksson, Magnus Nydén

Journal of Polymer Research **2012**, 19(2), 9821-9829

IV Bi-layer formation of imidazole-modified ethyl(hydroxyethyl)cellulose at a hydrophobic surface as monitored by QCM-D

Jesper Hedin, Dan Isaksson, Markus Andersson and Magnus Nydén

Journal of Colloid and Interface Science **2009**, 336(2), 388-392

V The effect of pH on charge, swelling and desorption of the dispersant poly(methacrylic acid) from poly(methyl methacrylate) microcapsules

Markus Andersson Trojer, Anne Wendel, Krister Holmberg and Magnus Nydén

Colloid and Interface Science **2012**, in press, doi: 10.1016/j.jcis.2012.02.026

VI The Importance of Proper Anchoring of an Amphiphilic Dispersant for Colloidal Stability

Markus Andersson Trojer, Krister Holmberg and Magnus Nydén

Langmuir **2012**, 28(9), 4047–4050

VII Charged microcapsules for controlled release of hydrophobic actives
Part I: Synthesis and characterization

Markus Andersson Trojer, Ye Li, Christoffer Abrahamsson, Azmi Mohamed, Julian Eastoe, Krister Holmberg and Magnus Nydén

Manuscript

VIII Charged microcapsules for controlled release of hydrophobic actives
Part II: Surface modification by LbL adsorption and lipid bilayer formation

Markus Andersson Trojer, Maria Claesson, Ye Li, Julian Eastoe, Krister Holmberg and Magnus Nydén

Manuscript

IX Charged microcapsules for controlled release of hydrophobic actives
Part III: Sustained release of a hydrophobic model compound

Markus Andersson Trojer, Helena Andersson, Ye Li, Lars Nordstierna, Krister Holmberg and Magnus Nydén

Manuscript

Contribution Report

I	All experimental and major analytical work. Responsible for writing and submitting the manuscript.
II	Major part of experimental and analytical work. Responsible for writing the major part of and submitting the manuscript.
III	Some experimental and analytical work. Responsible for concluding and submitting the manuscript.
IV	Responsible for writing certain parts of the discussion
V	Most experimental and major analytical work. Responsible for writing and submitting the manuscript.
VI	Most experimental and major analytical work. Responsible for writing and submitting the manuscript.
VII	Most experimental and major analytical work. Responsible for writing the manuscript.
VIII	Most experimental and major analytical work. Responsible for writing the manuscript.
IX	Some experimental and some analytical work. Responsible for writing the manuscript.

List of Publications Not Included in this Thesis

I Replacement of H-bonded bridged water by transition metal ions in poly(1-vinylimidazole-co-methylmethacrylate) copolymers: a vibrational spectroscopy study using mid-FTIR, far-FTIR and ab initio calculations

Markus Andersson Trojer, Anders Mårtensson and Magnus Nydén

Vibrational Spectroscopy **2012**, in press, doi: 10.1016/j.vibspec.2012.02.017

Table of Contents

CHAPTER 1

Introduction

Fouling of ships by marine organisms has, throughout the history of sea transportation, been a serious complication for the shipping industry. The problem is particularly difficult to solve, both from an economic and environmental perspective, due to its multi-faceted nature, where countermeasures often result in new unpredictable problems. The countermeasures typically consist of antifouling biocides incorporated in a paint system. Regarding the biocides, target specificity is a complex dilemma. Highly target specific biocides will only affect a narrow spectrum of the fouling organisms whereas a biocide with broad toxicity will affect non-target organisms. The formulation and controlled release of these biocides is another unsolved problem.

To overcome these problems, the solution calls for fundamental research. Furthermore, multidisciplinary science is needed in order to understand the problem and to innovate new antifouling methodologies. One method is to encapsulate a cocktail of different target specific biocides in microcapsules. The material of the microcapsules is of outmost importance for the release characteristics. The development and characterization of such materials has been the scope of this thesis.

1.1 Background

A major problem for the shipping industry is fouling of marine organisms, such as algae, muscles and barnacles on a ship's hulls (see Figure 1.1)[1-5]. As the ship moves through the water, the hull is subjected to *form drag* and *skin friction drag*[a]. Since fouling increases the surface roughness, the skin friction drag is increased, which subsequently results in increased fuel consumption and reduced manoeuvrability[3].

Figure 1.1. Barnacles, a severe fouling problem (Photo by Alexandra Wattwil)

[a] Skin friction drag arises from the viscous drag in the boundary layer of the object.

A ship without antifouling coating may increase its fuel consumptions by 40% within six months[1, 6] (see Figure 1.2). In addition to the increased fuel consumption, fouling necessitates maintenance which leads to more frequent dry docking, surface treatments and/or repainting of the surface.

Figure 1.2. Effect of Fouling (From *International Paint*)

For the shipping companies this entails large costs. The US navy faces annual costs of over 1 billion € as a result of fouling, including maintenance costs and the costs of increased fuel consumption. To prevent fouling, approximately 80 000 tons of antifouling paint is consumed annually to a value of 1 million €[1].

Apart from economic implications, the increased fuel consumption impacts the climate due to the increased emissions of CO_2. In addition, the emissions contain high amounts of hydrocarbons, particles, NO_x and especially SO_x causing pollution of the environment[1]. Traditional countermeasures against marine fouling are coatings containing antifouling toxicants which have had severe environmental consequences on the marine ecosystems.

There are 50 000 commercial vessels operating globally and 90% of all transports go by sea. Furthermore, there are about 1 million leisure boats in Sweden.

1.2 Marine Paints

Since ancient times, man has tried to prevent marine organisms from settling on ship hulls. The oldest antifouling systems known are wax, tar and asphalt coatings. Copper was already used as antifoulant by the Phoenicians and Carthagians, while the Greeks and Romans used led. The first commercial antifouling paints were developed in the mid-19th century and comprised heavy metals dispersed in linseed oil, shellac or rosin[2]. The first organometallic paint systems (comprising led, arsenic, mercury etc) met the market in the early 1960s and the notorious tributyltin self-polishing coating (TBT-SPC) were developed in the 70s[2, 6].

Initially it was believed that the TBT-SPC paint systems had completely solved the problems related to marine fouling. However, the first reports of its negative environmental effects came in the 70s in France where oysters displayed severe shell deformities as a result of exposure to TBT. As the use of TBT containing paints increased, marine life in the vicinity of harbours and marinas was severely affected. The hazardous nature of TBT for the marine environment is ascribed to its weakening of fish immune systems, causing imposex and sterilization of female mollusk organisms (at such low concentration as 1

ng/L) as well as its bioaccumulative properties in mammals[1, 2, 4, 6]. TBT containing paint systems were successively phased out in the 90s and finally banned by IMO (the International Maritime Organization)[b].

A number of tin-free alternatives have been developed due to the restrictive legislation regarding TBT paints. These can crudely be divided into *biocide-release* and *biocide-free* antifouling systems. The biocide release paint systems may be further divided into sub groups depending on the specific mechanism of release: *soluble matrix*, *insoluble matrix* (*contact paint*) or *tin-free SPC paints* [2, 3]. SPC paints are discussed in detail below (since this is the paint system connected to this project).

Biocide-free approaches are dominated by paint systems called *foul-release coatings*. The antifouling mechanism lies in the low surface energy and smoothness of the coating[c]. The binders in these coatings are silicone polymers, e.g. PDMS (polydimethylsiloxane) and to some extent fluoropolymers, both possessing very low surface energy.

Anti-adhesive coatings may also be obtained by microseparated structures in the coating, surface modifications or different kinds of surface microtopographies. These include incorporation of synthetic microfibers in the coating, PEGylation of the surface to increase resistance towards protein adsorption, grafting of enzymes onto the surface with the ability to degenerate the adhesives secreted by the fouling organism etc. Many techniques are inspired by nature, e.g. the skin of dolphins, whales and sharks. For instance, dolphins secrete a hydrophobic glycoprotein of low surface tension, whereas killer whales possess a skin with a certain nanoroughness which is covered with an anti-adhesive gel.

1.2.1 Self-polishing coatings

The reason for the success of the TBT-SPC paints discussed above is that the rate of release can be controlled on a molecular level. Generally, these paints are based on acrylic or methacrylic copolymers. The active substance (TBT) is covalently attached to the carboxylic group of the polymer, which is hydrolytically instable in slightly alkaline conditions (as in seawater)[2, 4, 6].

SPC paints present many advantages in comparison to other antifouling alternatives. The paint system provides control of biocide release with a constant minimum rate. The rate of hydrolysis is easily regulated by the chemical properties of the binder. The lifetime of the coating is directly proportional to the thickness of the coating. The erosion generates a smooth, polished surface which additionally contributes to minimizing the hull roughness and subsequently the fuel consumption. The boat bottom surface may be repainted without removal of the present coating[2-4, 6].

Regarding tin-free SPC paints, tin is replaced by other elements such as copper, zinc, silicon etc. Even though the side group of a few tin-free SPC paint binders also possess biocidal properties, no alternative is nearly as effective as TBT[4, 6]. To maintain antifouling properties of the coating it is necessary to add other biocides, so called *boosters,* generally in combination with copper. The most frequently employed boosters are conventional agrochemicals, some of which, e.g. irgarol, have been under scrutiny due to low rate of biodegradation as well as toxicity towards non target organisms[2, 4, 6]. Since also the use of copper has been under debate recently, a number of other pigments are used such as Zn(II), Fe(III) and T(IV) oxides[2-4, 6].

[b] Production of TBT containing paints was globally banned in 2003 and the use of these paint systems on boats was completely forbidden in 2008.

[c] The fouling organism must first wet the surface in order to adhere to it and this ability is reduced the lower the surface tension.

However, a generic problem with regard to tin-free SPC paints is premature leakage of the booster biocides[1, 3]. These are not anchored to the binder, as TBT is, and are hence subjected to free diffusion within the paint matrix. The immediate effect of premature leakage is loss of antifouling effect prior to the hydrolysis dependent lifetime of the coating.

1.3 Microcapsules

Microencapsulation of active substances (e.g. biocides) is an efficient and robust way for controlling and thereby prolonging the antifouling properties of a coating[7-9]. It has been suggested as a tool for controlling the release and protecting natural antifouling biocides in marine paints[3]. However, microcapsule technology has, as of yet, not been exploited to a large extent within the coating industry[8].

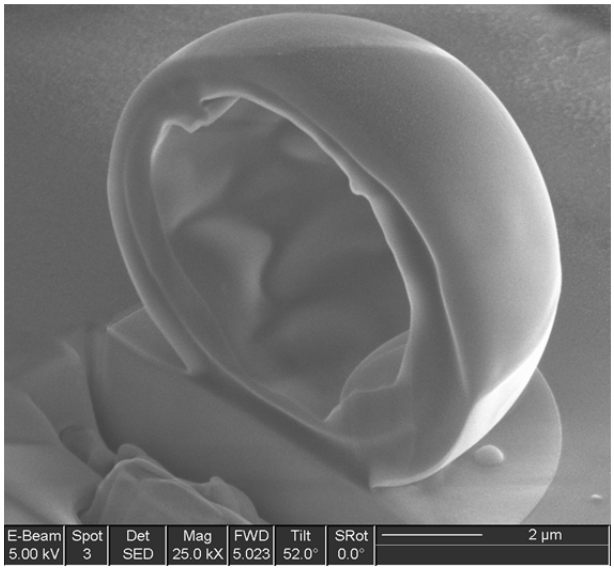

Figure 1.3. SEM image of cross-section of a microcapsule (Image taken by Johan Hurtig).

The first successful commercial employment of microcapsule was encapsulation of dies in carbonless copy paper. Since then, microencapsulation has generally most been associated with and exploited by the pharmaceutical industry to protect actives and provide sustained, controlled and/or enteric release. During the last decade, microencapsulation has also found use in the agricultural, food, cosmetic and textile industry in order to provide functions such as controlled release, masking odors/tastes, provide protection, improve processability etc[7-9].

The definition of a microcapsule is a particle of micrometer size (1-1000 µm) consisting, generally, of a core coated by a shell. The specific morphology may vary and the actual core is sometimes absent (see chapter 3.4.2). Such a homogenous particle is called *microsphere*. The active substance is typically residing in the core (or dispersed in the shell matrix). The capsule is, apart from morphology and size, characterized by its size distribution, actives content and distribution, surface charge as well as release mechanism and profile[7, 9].

Microcapsules provide an enormous flexibility with regard to choice of core and shell material. Most gaseous, liquid or solid materials may be encapsulated, regardless of the hydrophlicity/hydrophobicity.

Yet, the core is usually a solution, dispersion or emulsion. Regarding the shell, any coating material is a potential shell/matrix material (e.g. synthetic polymers, biopolymers, sugars, waxes, fats, metals, inorganic oxides etc.) although polymers and lipids are by far the most common[7-9]. With regard to microcapsules incorporated in coatings such as antifouling paints, it is of outmost importance for the shell to be compatible with the binder in order to prevent phase separation (see Figure 1.4)[8].

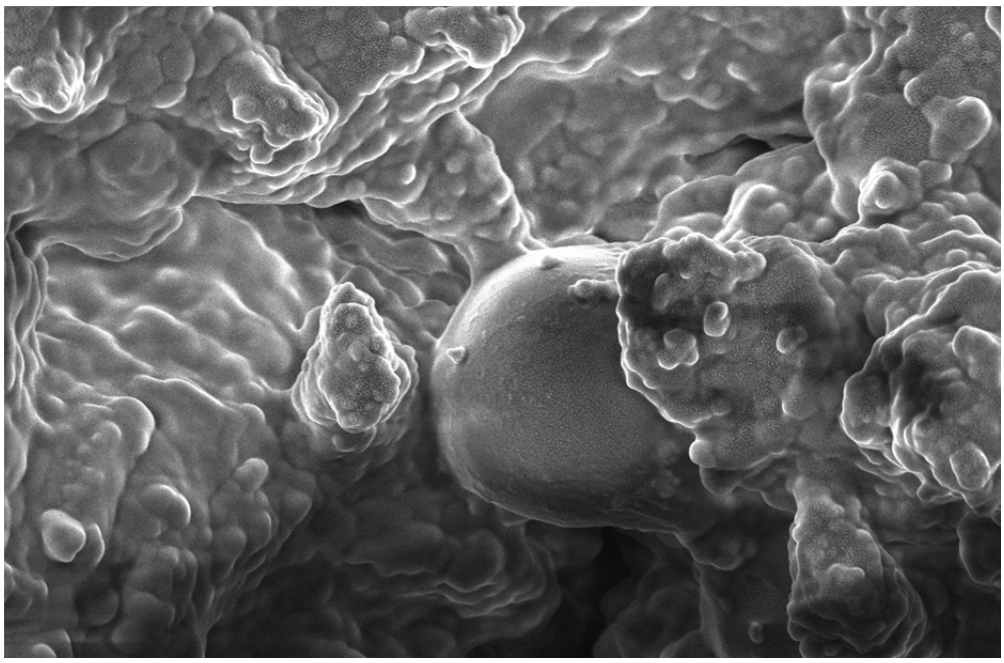

Figure 1.4. SEM (Scanning Electron Microscopy) image of a microcapsule dispersed in a SPC-paint matrix (Image taken by Lars Nordstierna).

As discussed in the previous chapter, acrylic or methacrylic copolymers usually constitute the binder in SPC paints. Hence, it is logical to choose similar polymers with regards to the shell/matrix material. The picture displays an intact microcapsule with a PMMA (polymethylmethacrylate) shell which is satisfactorily dispersed within the paint matrix.

There is a variety of different microencapsulation techniques available[d], each resulting in unique microcapsule characteristics[7-9]. The microcapsules explored in this project are generally core-shell particles or so called microspheres, synthesized by the solvent evaporation procedure developed by Vincent et al. (see chapter 3.4.2 for details)[10-13]. Solvent evaporation is an encapsulation technique especially suited for biocide loaded microcapsules with sizes ranging from <1 μm to several 100 μm[9].

The most recent research concerning microcapsules is focused on the properties of the shell[7]. By tailoring the chemical and physical properties of the shell material, the shell may be rendered permeable, semipermeable, impermeable or enteric, depending on application[7, 9].

[d] Phase separation techniques (simple, salting out and complex coacervation), interfacial and in situ polymerization/polycondensation, polyelectrolyte layer by layer techniques, spray drying and spray congealing, solvent evaporation techniques, rapid expansion of supercritical fluids, co-extrusion and different coating techniques (e.g. fluidized bed techniques such as Wurster coater) to mention a few.

CHAPTER 2

Objectives

The overall vision of this project is to prevent fouling of marine organisms on ship hulls as described in the introduction. In this work, two intrinsically different approaches to achieve antifouling marine coatings and/or controlled release have been developed and investigated. In the following subchapters, the background for each approach is outlined including the background for the change of approach.

2.1 Triggered Release and Imidazole-Cu^{2+} Coordination

At an early stage, the microcapsules discussed earlier were believed to be inert in the coating and more or less impermeable. The release of the antifouling substance should therefore be triggered by some physical or chemical parameter at the ship-water interface. Subsequently, the aim of the first approach was to achieve *triggered release* by incorporating salt in the otherwise rather hydrophobic microcapsule shell. The salt would initiate swelling of the shell and hence trigger the release from the microcapsule shell as a function of contact with water or moisture (see Scheme 2.1). The functionalization of the microcapsule shell with salt was to be realized using a shell forming polymer with a fraction of imidazole-type ligands. Imidazole-ligands interact, very strongly with the transition metal ion Cu^{2+} and Zn^{2+} which subsequently enables the incorporation of salts into the shell.

Scheme 2.1. Triggered release mechanism of microcapsule in SPC-paint

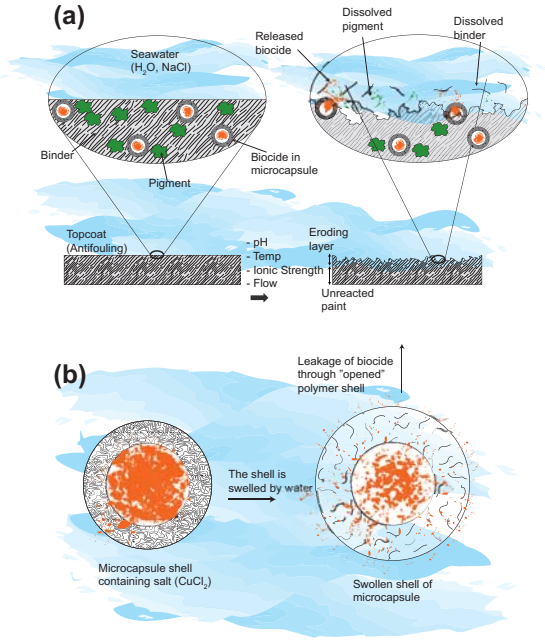

This coordinating ligand-transition metal ion approach has been further developed to encompass the more generic concept of *biocide-free* antifouling coatings. By incorporating imidazole-type ligands in the antifouling coating, natural abundant Cu^{2+} from the sea may be absorbed. Furthermore, the presence of strongly Cu^{+} stabilizing ligands, e.g. nitriles and sulphur containing ligands, may catalyse the reduction of Cu^{2+} to Cu^{+}. This will produce high concentrations of Cu^{2+} and Cu^{+}, both of which are efficient antifouling agents, at the coating interface without any net addition of biocides to the environment (see Scheme 2.2).

The synthesis and characterization of such coordinating materials was the main focus of the first part of this thesis (**Paper I-IV**). However, the work concerning redox reaction of Cu^{2+}/Cu^{+} is not included in this thesis.

Scheme 2.2. Mechanism for ligand mediated absorption and redox-reaction.

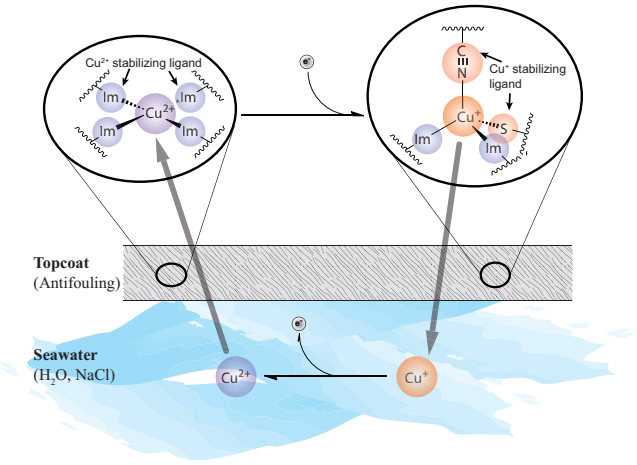

2.2 Sustained Release, Charged Hydrophilic Barriers and Lipid Bilayers

As the work on the release from microcapsules progressed, it was found that the notion of the microcapsule as a impermeable, inert entity was not at all a realistic picture. The microcapsules were leaking actives at a much higher rate than anticipated. Consequently, the challenge was not to trigger the release but rather controlling a slow release.

Scheme 2.3. Doublebarrier release system.

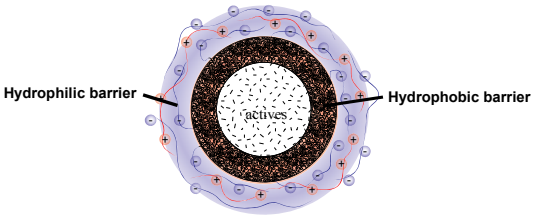

This background led to the second approach comprising *sustained release*, which is discussed on a theoretical basis in chapter 3.6. We believe that the underachievement of the microcapsule as well as the potential solution may be thermodynamic in nature. If one first considers the inability of the capsule to prevent premature leakage, we believe that this is due to the poor barrier properties of the hydrophobic PMMA shell against the typically rather hydrophobic actives (antifouling agents). In some cases, almost all biocide is distributed in the shell rather than the core. One of many potential solutions (discussed in chapter 3.3.4 and 3.6) to this problem would be to have an additional hydrophilic, and in particular, charged barrier against the hydrophobic actives. A promising hydrophilic barrier is a polyelectrolyte multilayer. In addition to a polyelectrolyte multilayer, a lipid bilayer is also a plausible type of barrier, commonly found in nature as barrier material. Lipid bilayer formation of ionic lipids is strongly promoted on highly and oppositely charged surfaces. The polyelectrolyte multilayer discussed above could subsequently constitute such a charged surface. However, polyelectrolyte multilayers are only realizable on charged particles.

Therefore, the goal of the second part of this thesis has been synthesis of ionic microcapsules (**Paper V-VII**) and surface modification (**Paper VIII**) of the microcapsules with polyelectrolyte multilayers and lipid bilayers in order to reduce the release of actives (**Paper IX**).

CHAPTER 3

Theoretical Considerations

3.1 Imidazole Coordination Chemistry

3.1.1 HSAB principles and σ-interaction

The strong metal-ligand bonding between the metal ions Zn^{2+} (diamagnetic d^{10} full d-shell configuration), Cu^{2+} (paramagnetic d^9 configuration) and the imidazole ligand (see Scheme 3.1) may be explained by HSAB (Hard Soft Acid Base) principles[14-16]. To begin with, only the electron lone pair donation from the base (ligand) to the acid (metal), σ-bonding, will be considered.

Hard bases preferentially bond to hard acids via ionic bonding whereas soft bases favourably bonds to soft acids via covalent bonding[14, 15]. In the ligand field depiction (see Scheme 3.4) this implies that the energy levels of the metal (M) and ligand (L) orbitals (the d_σ- and σ-levels) will be similar[17, 18]. The ensuing M-L molecular orbitals will have almost equivalent proportions of metal and ligand character respectively and the electrons spend their time at the metal and ligand equally[17]. Ionic bonding denotes large orbital energy differences with essentially no electron sharing[14, 15, 17].

Scheme 3.1. Structure and numbering of imidazole.

N_1 is labelled pyrolle nitrogen and N_3 is labelled pyridine nitrogen. Note that N_1 is also sp^2 hybridized and the free electron pair is donated to the ring π-orbital system in order to obtain aromaticity. The lone electron pair of N_3 is however free rendering this nitrogen basic and the predominant site for coordination[16].

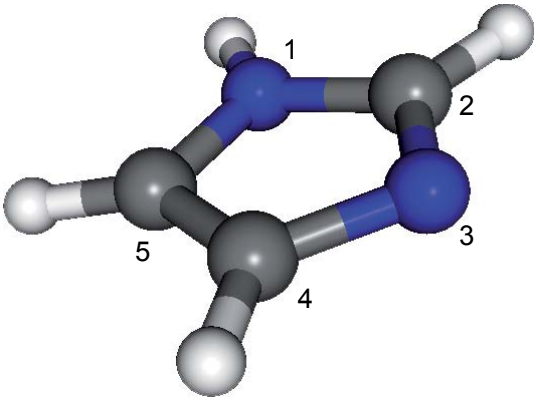

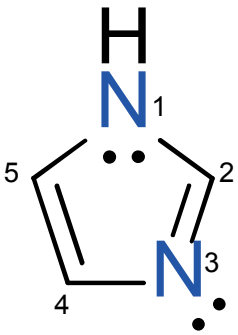

Hard acids and bases are small, hard to polarize with low and high electronegativity respectively[14, 15]. They possess large HOMO-LUMO (Highest Occupied Molecular Orbital, Lowest Unoccupied Molecular Orbital) gaps, favouring ionic bonding[17]. Soft acids and bases are large and polarizable with intermediate electronegativity and with small HOMO-LUMO gaps[14, 15]. A high oxidation state usually renders the transition metal hard whereas a low (≤2) renders it soft[17]. With regards to bases, unsaturation usually makes the base softer[15]. For regular σ-donors, the coordinate bond may be viewed as polar covalent, especially with regards to borderline acids and bases (see below)[15, 17]. The selectivity of different metal-ligand pairs in polymers has been treated in **Paper I**.

Scheme 3.2. Coordinate bonding modes envisaged for imidazole-Cu(II) in square planar symmetry (**Paper II**). The bonding principles are generic and applies also for Zn(II) complexes.

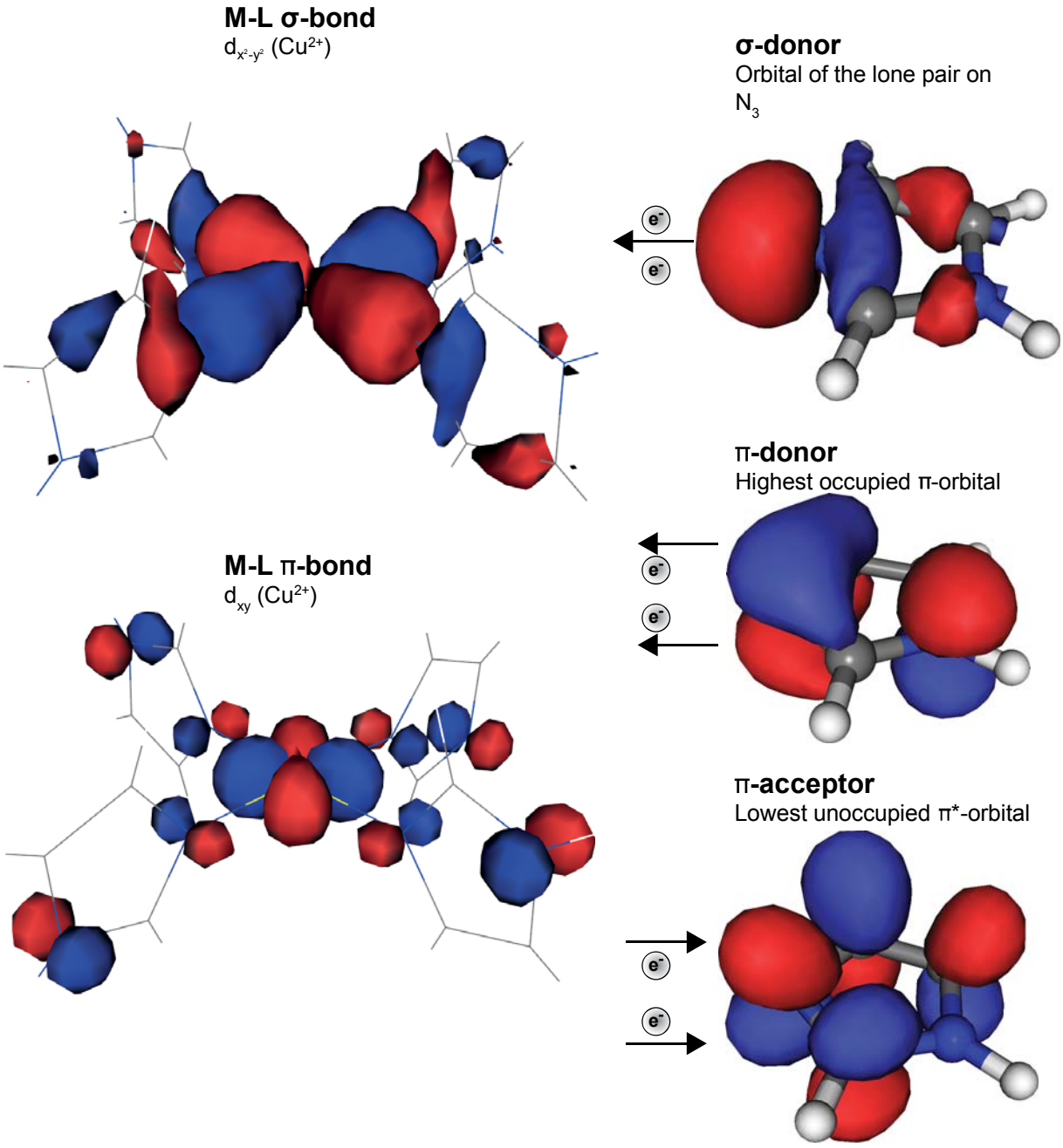

3.1.2 π-interaction

Another important interaction besides σ-bonding in transition metal complexes is π-bonding (see Scheme 3.2 and Scheme 3.4)[17]. Ligands with more than one lone pair, labelled π-donors or π-bases, e.g. Cl^-, RO^-, may donate additional electron density to a metal d orbital (π-acid) of proper symmetry (see Scheme 3.4, π-bond)[17]. This interaction is typically considered hard and destabilizes the metal d-orbitals but will be favourable for hard, electropositive (especially d^0) transition metals[17]. Certain ligands, labelled π-acceptor or π-acid have low lying vacant LUMO:s of proper symmetry with regard to the metal dπ-orbitals (π-base) susceptible for metal to ligand π-bonding (back donation) an interaction typically considered soft. This interaction may be favourable since it alleviates the metal of some electron density in the coordination

compound. For unsaturated ligands, the antibonding π*-orbital typically accepts electron from the metal dπ-orbitals which is favourable for electron-rich metals in low oxidation states with high energy d-orbitals that are basic in character[17].

3.1.3 Coordination geometry

Imidazole coordinates to Cu^{2+} in essentially square planar symmetry, $Cu(Im)_4^{2+}\cdot X^-_2$, similar to pyridine (see Scheme 3.3a and Scheme 3.4c) with the imidazole rings occupying coplanar positions with respect to Cu(II)[16]. This favours π-interaction between the imidazole ring orbitals and metal d_π orbitals and locates the electron hole in a distinctly separated orbital (see Scheme 3.4a)[16, 19]. In the case of Zn^{2+}, tetrahedral symmetry (common for d^{10} metals[18]), $Zn(Im)_4^{2+}\cdot X^-_2$ (see Scheme 3.3A)and/or octahedral symmetry (see Scheme 3.3B), $Zn(Im)_6^{2+}\cdot X^-_2$, is possible (see Scheme 3.4b). The coordination is less dependent on electronic factors and more on steric in contrast to Cu^{2+} complexes[16, 18]. The coordination geometry of imidazole ligands with respect to Cu^{2+} and Zn^{2+} has been studied in **Paper II**.

Scheme 3.3. Coordination geometries for imidazole-Cu(II) or –Zn(II) complexes. (a) Square planar $[Cu(Im)4]^{2+}$. (b) Tetrahedral $[Zn(Im)_4]^{2+}$. (c) Octahedral $[Zn(Im)_6]^{2+}$.

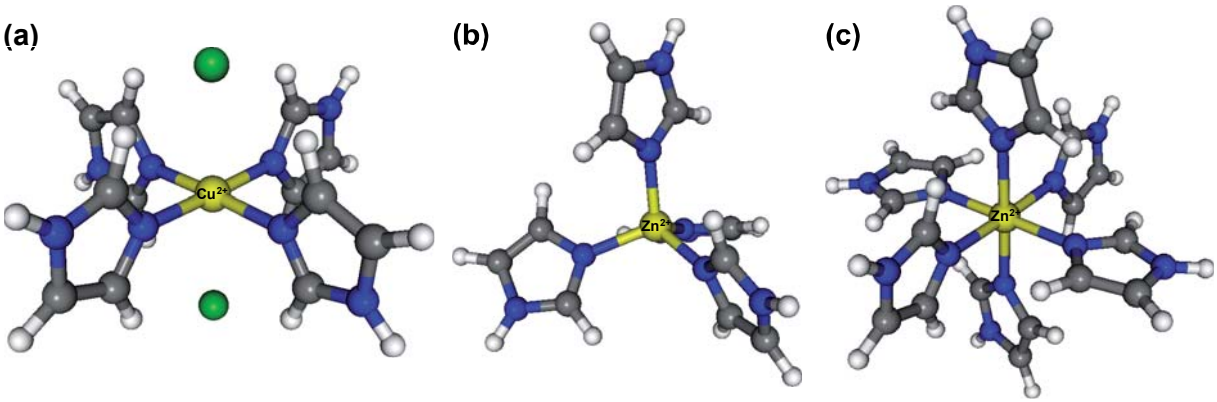

3.1.4 Comparison with other nitrogen ligands

Imidazole and other unsaturated nitrogen ligands, e.g. pyridine are categorized as a borderline base and Cu^{2+} and Zn^{2+} are borderline acids (in contrast to Cu^+ which is labelled soft)[14-16]. They consequently form favourable bonds with each other with properties intermediate of soft and hard acids and bases[14, 15, 17]. Imidazole is generally considered to be a moderate σ-donor and a weak π-acceptor, with σ-donor and π-acceptor abilities in between saturated amines such as ammonia (NH_3) and unsaturated amines such as pyridine[16]. This positions imidazole above oxygen donors and below ammonia and pyridine in the spectrochemical series[16, 20]. In rare cases, π-donor abilities from the imidazole ring π-orbital have been reported as well[21, 22].

The series of nitrogen donor ligands with increasing basicity follows the order NH_3>Im>Pyridine whereas the order of increasing π-acceptor ability follows the reverse order[16]. For Cu(II) and Zn(II) the bond strength (as presented by the stability constants, see the Appendix, Table A.1) follows the order Im>NH_3>Pyridine, reflecting a dominating importance of σ-bonding but also a significant contribution from π-bonding[16].

Scheme 3.4. (a) Molecular orbitals and ligand field splitting of Cu(II) in a square planar complex and (b) Zn(II) in a tetrahedral complex [23].

(a) With regards to cupric complexes, there is possibility for weakly bound counterions or coordinating solvent molecules in axial position and the symmetry is then labelled tetragonal (distorted octahedral symmetry). The ligand field splitting will however be similar in tetragonal and square planar symmetry if one accounts for the important 4s-3d_{z^2} mixing, which effectively lowers the metal d_{z^2} orbital in both symmetries[24]. (b) The ligand field splitting in tetrahedral complexes is the inverse of an octahedral one but with some mixing of the d_σ and p-orbitals. The situation with π-interaction is however more complicated since the π-interacting ligand orbitals may form both σ- and π-bonds and the effect on the ligand field splitting will be a reflection of both bonding modes[23, 24].

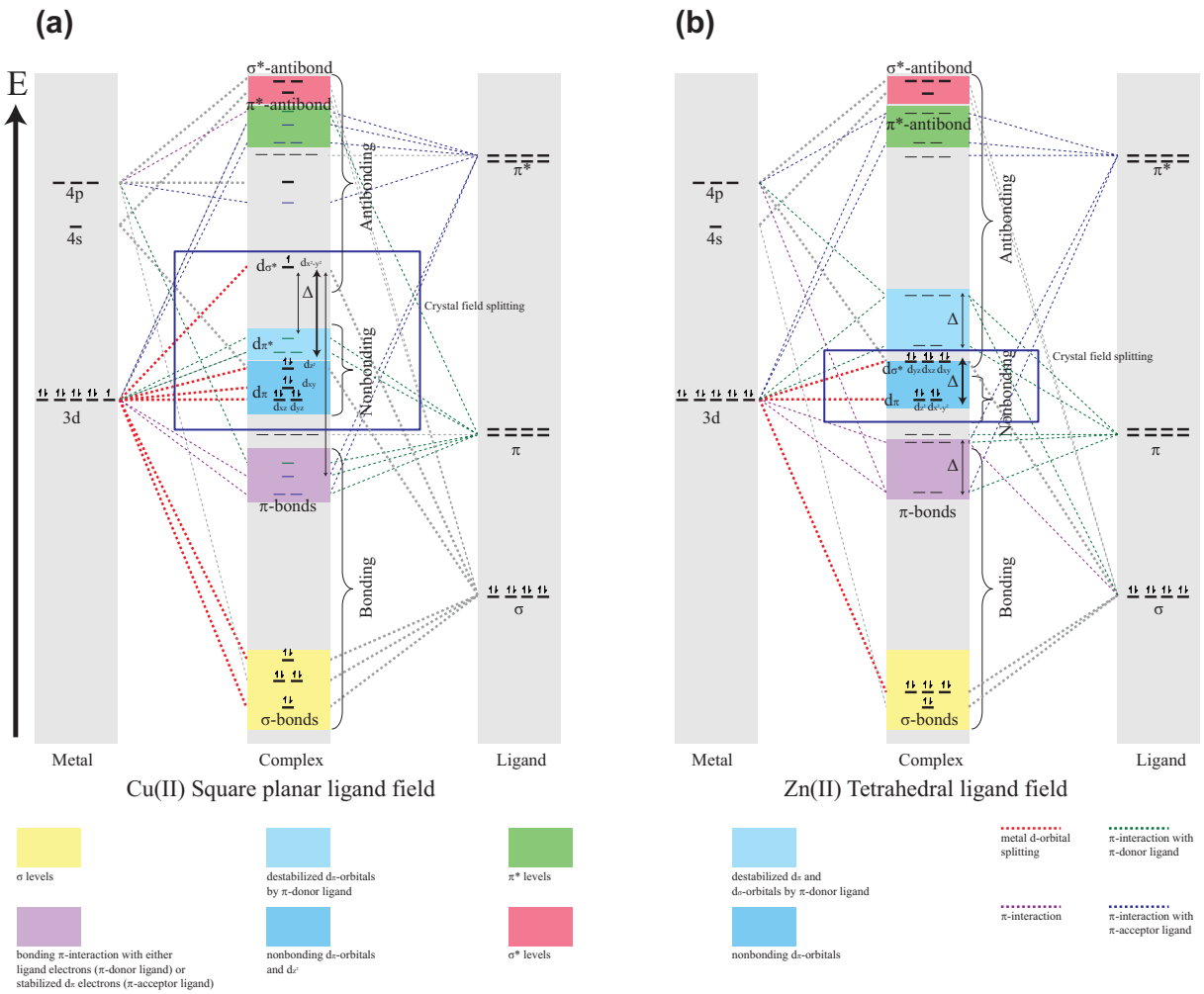

3.2 Polymers and Surfactants in Solution

3.2.1 Surfactants and lipids

Surfactants are amphiphilic molecules consisting of a polar head or heads and a hydrophobic tail or tails[25]. In solution, the surfactants self-assemble due to the hydrophobic effect into a variety of different structures (micelles, liquid crystals etc.) above a certain well-defined concentration called the critical micelle concentration (CMC)[25, 26]. The type of assembled structure depends on external parameters such as salt concentration, temperature and surfactant concentration as well as on geometrical factors with respect to the molecular structure of the surfactant[25]. This is described by the so called critical packing parameter (CPP) which relates the volume of the hydrocarbon chain v to the effective head group area a and the length of the extended chain l_{max} (Equation 3.1 and Scheme 3.5)[25, 27].

$$\mathrm{CPP} = \frac{v}{l_{\max} a} \qquad 3.1$$

Scheme 3.5. Some different types of surfactants used in this work and their respective packing parameters.

(a) Polyoxyethylene(23) laurylether, with the product name Brij® 35, is a nonionic water-soluble and micelle forming surfactant. It was used in this work to solubilize a hydrophobic release agent. (b) *N,N*-dimethyl-*N,N*-dioctadecylammonium chloride is a cationic lipid which was used to assemble lipid bilayers on microcapsules. (c) The branched sulphonate (anionic) surfactant, abbreviated TC4, is water insoluble but readily soluble in oils due to the three methylated hydrophobic tails. TC4 was used to create a negative charge density on the surface of emulsion oil droplets during the microencapsulation.

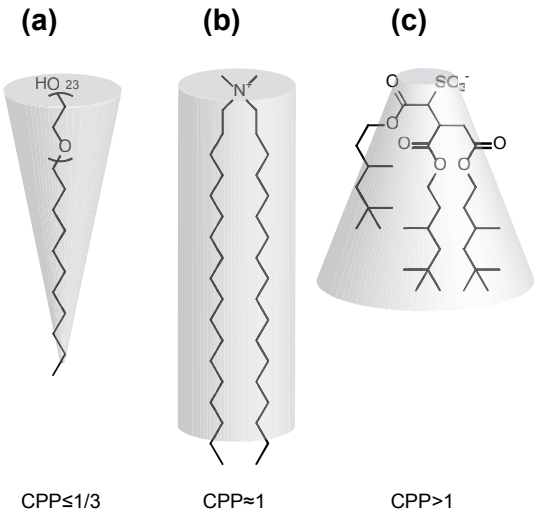

Lipids, together with double chained surfactants, are a class of amphiphiles with a CCP≈1[25, 27]. In this work, we have also chosen to call double chained quaternary amines (Scheme 3.5b) lipids. Due to the packing parameter, these types of surfactants preferentially form lamellar phases, in which the surfactants on a molecular scale are packed close together in bilayers[25, 27, 28]. The bilayer is fluid at high temperature (liquid crystalline, L_α phase) but solidifies below a certain transition or melting temperature T_m[27-29]. Symmetrical saturated lipids with a headgroup area of the same size as the cross-sectional area of the double chains crystallizes below T_m in a tight-packed L_β phase[27, 28]. If there is a mismatch, a gel-phase ($L_{\beta'}$ or $P_{\beta'}$) where the head-group maintain a certain degree mobility may form[27-29].

The lamellar liquid crystals in coexistence with a dilute water phase may be dispersed in the aqueous phase by applying energy to the system (e.g. sonification). The dispersed structure called *vesicle* or *liposome* comprises a spherical bilayer encapsulating an aqueous core. Depending on the size and morphology, the vesicle is categorized as; small unilamellar (SUV, <0.1 μm), large unilamellar (LUV, >0.1 μm), or multilamellar (MLV)[27].

Lipid bilayers, in their fluid state, are generally impermeable to ions and larger polar molecules but permeable to hydrophobic molecules and even water. However, bilayers comprising lipids with long saturated symmetrical double-chains are rendered impermeably even for water below T_m[30, 31]. Saturated lipids with hydrophobic chains comprising more than 14-16 carbons are solid at room temperature[28, 30, 31].

3.2.2 Homopolymers and random copolymers

The general solubility of a polymer in solvent may be described by the traditional Flory Huggins theory for binary mixtures where ϕ_i is the volume fraction, V is the volume and V_0 is the molar volume (assumed to be equal for monomer and solvent[32, 33].

$$\Delta G^{M} = \frac{RTV}{V_0}\left(\phi_1 \ln(\phi_1) + \frac{\phi_2}{N}\ln(\phi_2) + \phi_1\phi_2\chi_{12}\right) \quad 3.2$$

If the polymer is large (represented by the degree of polymerization, N), the entropic contribution upon solvation disappears (which is very different compared to small molecules such as surfactants). In the polymer-solvent binary system, χ_{12} defines the efficiency of polymer segment interaction with the solvent[32, 33]. The Flory Huggins interaction parameter is defined as;

$$kT\chi_{12} = z\Delta\varepsilon_{12} \quad 3.3$$

where; $\Delta U=\Delta\varepsilon_{12}=\varepsilon_{12}-\frac{1}{2}(\varepsilon_{11}+\varepsilon_{22})$ is the change of interaction as a result of new polymer-solvent interactions upon solvation[32, 33]. ΔU is the internal energy and may be replaced by ΔH if $\Delta H\approx 0$;

$$\Delta H^{M} = \frac{V}{V_0} RT\chi_{12}\phi_1\phi_2 \quad 3.4$$

The interaction parameter χ_{12} may be defined as the energy difference when 1 mol solvent is immersed in pure polymer compared to pure solvent. As the interaction parameter approaches $\chi_{12}=0.5$, the solvent quality for the polymer becomes poor. A good solvent obtains values down to $\chi_{12}=-1$.[33]

The size of the polymer coil (Scheme 3.6) will depend on the solvency which is important for colloidal stability as discussed in chapter 3.5. In dilute solution, the radius of gyration R_g scales as in Equation 3.5 where M is the molecular weight and v is the Flory interaction parameter[27, 33, 34]. In a θ-solvent ($\chi_{12}=0.5$), the polymer coil scales as $v=0.5$ in accordance with a random walk model[33, 34]. In a good solvent ($\chi_{12}<0.5$), the polymer coil swells due to the excluded volume effect and scales as $v=0.6$ for long flexible polymers[25, 33, 34]. In a bad solvent ($\chi_{12}>0.5$), the coil collapses to a compact globule (followed by phase separation) and scales as $v=1/3$[33, 34].

Scheme 3.6. Some different types of polymers used in this work.

Homopolymer

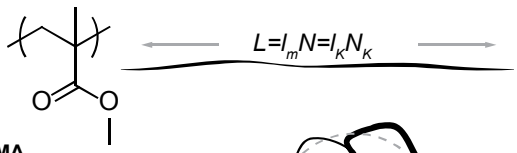

PMMA
Polymethylmethacrylate

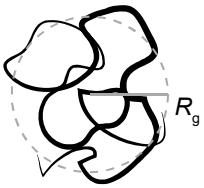

Random copolymer

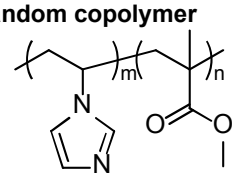

PVM or P(1-Vim-*co*-MMA)
Poly(1-vinylimidazole-*co*-methyl methacrylate)

Block copolymer

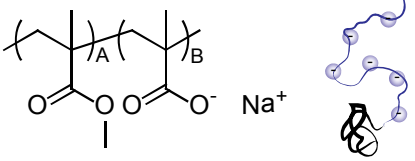

PMMA-*b*-PMANa
Poly(methyl methacrylate)-*block*-poly(sodium methacrylate)

Strong polyelectrolyte

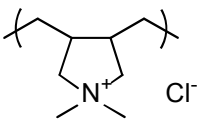

PDADMAC
Poly[diallyldimethylammonium chloride]

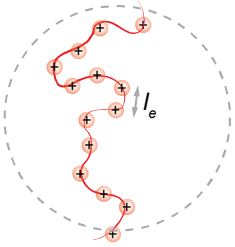

Weak polyelectrolyte

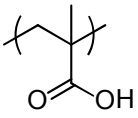

PMAA
Poly(methacrylic acid)

The solvency and stiffness of the polymer may be described by the persistence length l_p (defined at θ-conditions in Equation 3.6) and the Kuhn segment length l_K according to Equation 3.7 where l_m is the monomer length (see Scheme 3.6) and $l_K=2l_p$ at θ-conditions. Note that Equation 3.7 is always valid (for $l_m N >> l_K$) independent of solvent quality[27, 34]. As the solvency increases, l_K increases and N_K decreases.

$$R_g \propto M^v \quad \textbf{3.5}$$

$$l_p = \frac{3R_g^2}{l_m N} \quad \textbf{3.6}$$

$$l_K = \frac{6R_g^2}{\underbrace{N_K}_{\frac{l_m N}{l_K}}} \quad \textbf{3.7}$$

Regarding random copolymers, the situation is more difficult since the different chemical nature of the polymer segment must be taken into account with respect to the interaction parameter. Yet, for random copolymers (and alternating copolymers), the solution properties are usually the weighted average with respect to the monomer composition[33, 34]. However, *hypercoiling* may occur if the solvent is bad for one segment[34].

3.2.3 Block copolymers

Block copolymers consisting of two blocks (A and B, see Scheme 3.6) behave in many respects similar to surfactants as discussed earlier. It is here important to make a distinction between *non-selective* and *selective* solvents. In the following discussion we consider block copolymers in aqueous solution where water is a selective solvent. In a non-selective solvent, both blocks are in a good solvent and behave similar to homopolymers[27, 34]. On the other hand, in a selective solvent (e.g. $\chi_A>0.5$ and $\chi_B<0.5$), the polymers self-assemble above a well-defined CMC equivalent to the self-assembly of surfactants, although the CMC is usually much lower for block copolymers given their large sizes[27, 35, 36]. The type of aggregate formed depends on the relative lengths of the blocks, the attraction of the A-block and the repulsion between the B-block, just as for surfactants[35, 36]. Depending on the block-block interaction parameter χ_{AB}, there may also be a substantial amount of block interpenetration[34]. For block copolymers where the hydrophilic block is a highly charged polyelectrolyte, single micelles are usually formed[35, 36].

The micellar aggregates in solution are not necessarily at thermodynamical equilibrium. The hydrophobic block in a block copolymer micelle is often kinetically frozen (in contrast to surfactants) and the structure formed depend on the process history[35, 36]. The glass transition temperature (T_g) of for instance PMMA is 105 °C rendering the polymer frozen at room temperature. In order to obtain structures corresponding to thermodynamic equilibrium, the block copolymer is usually dissolved in a non-selective solvent (e.g. dimethylformamide) which is subsequently exchanged with water[35, 36].

3.2.4 Polyelectrolytes

Polyelectrolytes are generally very water-soluble polymers. The water-solubility arises from the entropic gain due to released counter ions upon solvation rather than ion-dipole interaction with water molecules[25, 27]. This entropic contribution is well accounted for by an extended (yet simplified) Flory Huggins theory (Equation 3.8)[37]. Here it is assumed that all monomers release counter ions which clearly increases the entropic contribution. This effect diminishes as salt is added[37].

$$\Delta G^{M} = \frac{RTV}{V_0}\left(\phi_1 \ln(\phi_1) + \frac{N+1}{N}\phi_2 \ln(\phi_2) + \phi_1\phi_2\chi_{12}\right) \quad \textbf{3.8}$$

The polyelectrolyte chain is very extended due to the intermolecular repulsion[25, 27, 34]. The electrostatic contribution l_{EL} to l_p is accounted for in Equation 3.9 and Equation 3.10 where l_p^0 is the persistence length at zero charge l_B is the *Bjerrum length* (the distance at which the ion-ion interaction equals kT) and l_e is the distance between the polymer charges, ε_0 and ε_r are the dielectric permittivity of vacuum and the medium[27, 34]. The electrostatic contribution is through the Debye length κ^{-1} (Equation 3.11) dependent on the salt concentration c_0 (z is the valence of the ith type of ion).

$$l_p = l_p^0 + l_p^{EL} \quad \textbf{3.9}$$

$$l_p^{EL} = \frac{l_B}{4\kappa^2 l_e^2} \quad \textbf{3.10}$$

$$\kappa^2 = \frac{\sum_i c_{i0} z_i^2 e^2}{\varepsilon_0 \varepsilon_r kT} \quad \textbf{3.11}$$

Clearly, the electrostatic contribution will be screened by added salt. In a salt free solution, R_g scales as a rigid rod with ν=1 in Equation 3.5 when $l_p \approx N l_m$[25, 34]. Very long chains will still scale as ν=0.6, as will polyelectrolytes in salt solution[25].

The discussion above has so far only concerned *strong polyelectrolytes* with a permanent charge density. The situation for *weak polyelectrolytes* is more complex. The entropic contribution in Equation 3.8 will now depend on the degree of dissociation α (Equation 3.12 and Equation 3.13) which in turn depend on the concentration of counter-ions. α may be described according to the extended Henderson-Hasselbalch equation (Equation 3.13 for weak polyacids). pK'_a is the apparent acid dissociation constant and n, which is ≥ 1, is a constant that depends on the type of polyacid and on the ionic strength. HA and A^- are the protonated and deprotonated acid respectively. The equation is directly applicable to most weak polyacids, for which the pK_a is a monotonously increasing function of α[38]. Some polyacids, such as poly(methacrylic acid) in Scheme 3.6, undergoes a change in chain conformation in the bulk as a function of α, and as a consequence, the extended Henderson-Hasselbalch equation should be used with more caution[39]. Nonetheless, in the limit of $K_a \to 0$ and $\alpha \to 0$, the regular Flory Huggins solution theory and scaling may be applied. In the limit $K_a \to \infty$ and $\alpha \to 1$, the polymer behaves as a regular strong polyelectrolyte as described above[25, 34].

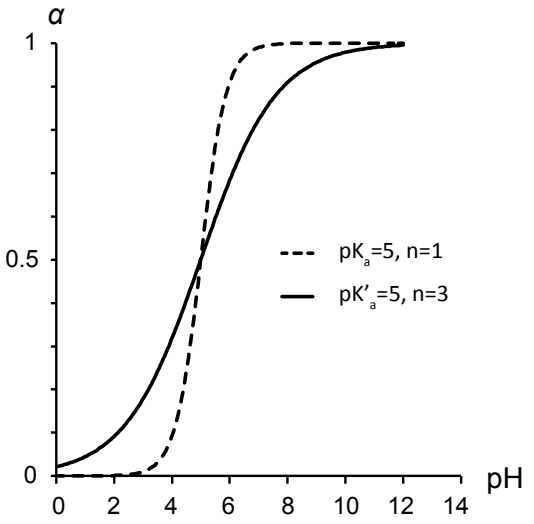

Figure 3.1. Plot of a vs pH for a small molecular acid with pK_a=5 (dashed line) and a polyacid with an pK'_a=5 and n=3 (solid line).

Note that the corresponding monomer of the polyacid is more acidic than small molecular acid since α starts to increase at lower pH.

$$HA \xrightarrow{K_a(\alpha)} H^+ + A^- \quad \textbf{3.12}$$

$$\alpha = \frac{1}{1 + 10^{\left(-\frac{pH - pK'_a}{n}\right)}} \quad \textbf{3.13}$$

3.3 Polymers and Surfactants at Interfaces

Surfactants and many polymers are surface active[25-27]. As a consequence the interfacial tension, discussed in more detail in chapter 3.4, will be affected. If there is a net adsorption from the bulk phase the interfacial tension will be reduced. If there is negative adsorption relative the bulk phase, called *depletion*, the interfacial tension will be increased[27, 34]. These properties are very important for colloidal stability as discussed in chapter 3.5.

3.3.1 Vesicle adsorption and supported lipid bilayers

Surfactants generally adsorb (from aqueous solution) as monolayers on hydrophobic surfaces. Regarding polar surfaces, monolayers are formed at low concentrations if there is a sufficiently strong head group-surface attraction[25]. At higher concentrations, the surfactants adsorb as bilayers or intact micelles depending on the head group-surface interactions[25].

As described in chapter 3.2.1, lipids have a CPP≈1 and will subsequently form bilayers on polar surfaces[25, 40]. The first lipid bilayer adhered to a substrate was reported by Mueller et al[41] and are often referred to as *supported lipid bilayers*[42-44]. The supported lipid bilayers may be prepared by monolayer transfer of *Langmuir Blodget films* or by *vesicle spreading*[40, 42, 43]. The following discussion will only concern the latter process.

Vesicle rupture and subsequent bilayer spreading on a surface is achieved by impairing the integrity of the vesicle[29, 42]. This may be realized by subjecting the vesicles to high tension (osmotic pressure or Ca^{2+} intercalation) or by strong adhesion to the surface or both[29, 42]. If the vesicle is not under tension or the adhesion between the vesicle and the surface is not sufficiently strong, intact vesicles will adsorb[40, 43, 45, 46]. However, bilayers may still form if there is a vesicle-vesicle attraction[29, 44]. The attraction is usually increased as the vesicles adsorb and above a certain critical surface coverage, bilayers may form[29, 40, 43, 44]. This so *called two-step process* is temperature activated and is often inhibited as $T \rightarrow T_m$ or $T < T_m$[44]. In contrast, a *one-step process* entails spontaneous vesicle rupture and spreading upon adsorption[40, 43] (see Scheme 3.7). This is predicted when the adsorption energy is very high and subsequently overcomes the elastic energy (rigidity) of the bilayer[28, 29], e.g. for vesicles and a surfaces of opposite charges[45-47].

The formation of supported lipid bilayers has also been expanded from planar surfaces to encompass colloidal surfaces[48-50]. Usually, vesicle spreading driven by electrostatics is employed[48, 50]. However, adsorption of free monomeric lipid on colloidal surfaces from organic solution has also been investigated[49].

Scheme 3.7. Supported lipid bilayer formation from liposomes *via* one step process mediated by electrostatic attraction.

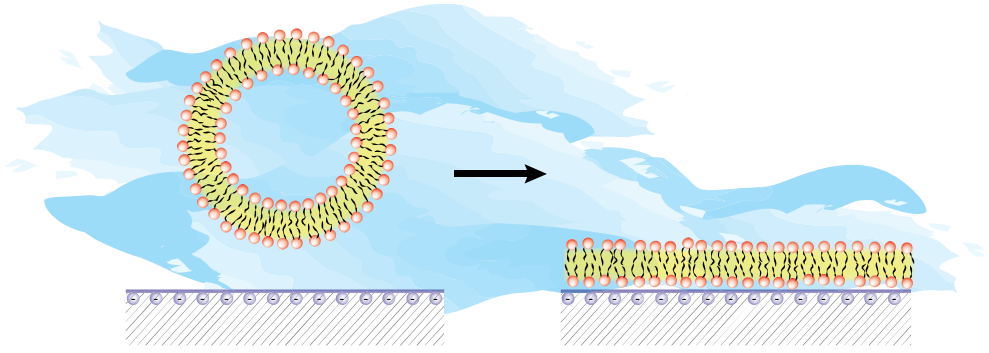

3.3.2 Homopolymers

In vicinity of a surface, the configurational entropy of the polymer is reduced. Therefore, a requirement for adsorption is a net attraction between the surface and the polymer[27, 34]. If there is no net attraction, the polymer will be *depleted* from the surface[34]. The net polymer-surface interaction is defined by χ_S in Equation 3.14 where ε^a_1 and ε^a_2 are the pair interactions of the solvent and the polymer with the surface respectively[34].

$$\chi_S = \left(\varepsilon_1^a - \varepsilon_2^a\right)/kT \qquad 3.14$$

Here, the quantity $kT\chi_S$ can be identified as the surface pressure $\pi=\gamma_0-\gamma$ where γ and γ_0 are the interfacial tensions with and without adsorbing polymer respectively[34]. If $\chi_S<0$, the polymer will be depleted from the surface. Moreover, due to the entropic constraints, χ_S must exceed a certain critical value $\chi_S>\chi_S^{Crit}\approx 0.1$ if the polymer is to adsorb[34].

The conformation of the adsorbed polymer is very important for colloidal stability as discussed in chapter 3.5.2. The adsorbed polymer is usually described as consisting of *trains*, *loops* and *tails* (see Scheme 3.8a)[27, 34]. With respect to steric stabilization, the tails are most important since they determine the *hydrodynamic thickness*. The fraction of tails and their extension is very dependent on solvency[25, 34]. If the solvency is decreased and the bulk polymer concentration is maintained, more polymers will adsorb and the thickness will remain constant[34]. However, in dilute solutions when the bulk reservoir of polymers is exhausted, the thickness will drop due to a conversion of tails to loops[34]. These effects are discussed to some extent in **Paper V**.

Scheme 3.8. Polymers at interfaces. (a) Adsorbed homopolymer consisting of trains, loops and tails. (b) Adsorbed block copolymers in a selective solvent (aqueous) with a hydrophobic *anchor* block and a hydrophilic *buoy* block. Polyelectrolyte adsorption on an oppositely charged surface at low salt concentration (c) and high salt concentrations (d).

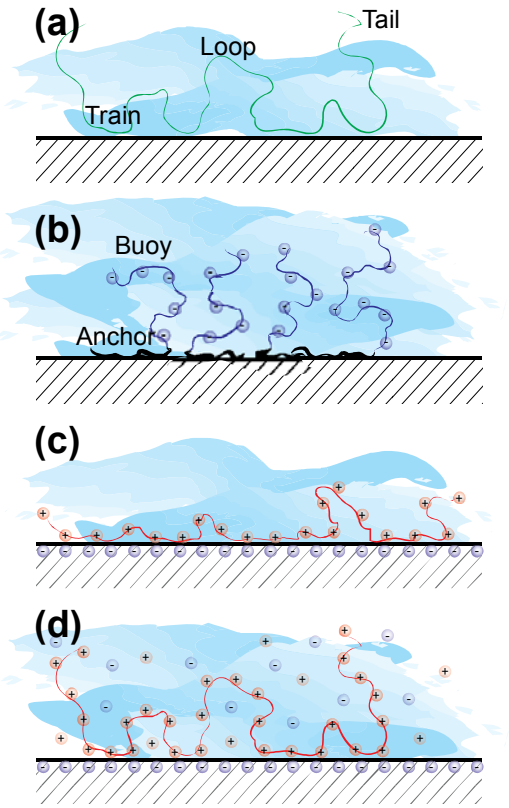

Apart from solvency, the molecular weight of the polymer has a profound effect on adsorption[25, 27, 34]. Generally, high molecular weight polymers are more prone to adsorb than low molecular weight polymers from thermodynamic arguments[25, 27]. However, smaller polymers are able to diffuse more rapidly to the surface[25, 34]. Consequently, kinetics are very important for polymer adsorption, especially for polydisperse polymers[25, 27, 34].

3.3.3 Block copolymers

Regarding adsorption of block copolymers, the distinction between selective and non-selective solvents is important as discussed in chapter 3.2.3. Nonetheless, one block is usually preferentially adsorbed even in non-selective solvents[34]. Already at small differences in χ_S between the blocks, one block act as *anchor* to the second *buoy* block (see Scheme 3.8b). In selective solvents, the adsorption is affected by the presence of micelles. The amount of free polymer available for adsorption is consequently constant above CMC. As

discussed in chapter 3.2.3, the micelles are often kinetically frozen and thermodynamic equilibrium is not necessarily reached in the three phase system (bulk, micelle, surface)[27, 34].

In a selective solvent, the anchor blocks (A) are assumed to form a melt on the surface[27, 34]. This is called the *van der Waals brush regime*[34]. The buoy blocks (B) forms so called polymer brushes due to the close packing of the block copolymers driven by the strong attraction between the anchor block and the surface. In a polymer brush where the buoy block are extended, the thickness of the adsorbed layer scales with M_B^1 and the fraction of tails is very high[27, 34, 51]. In contrast, in the so called *mushroom regime* at low surface coverage, the thickness of the adsorbed block copolymers is determined by R_{gB} and scales as M_B^v according to the solution theory described in chapter 3.2.2[27, 34, 51]. Regarding steric stabilization as discussed in chapter 3.5.2, especially good stabilization is obtained if the buoy block is depleted from the surface[27, 34].

3.3.4 Polyelectrolytes and multilayers

The adsorption behaviour of polyelectrolytes is, similar to the bulk properties of polyelectrolytes, governed by electrostatics and subsequently very dependent on salt concentration[52-56]. We will first consider adsorption at low salt concentrations. Regarding surfaces with the same sign of the charge as that of the polyelectrolyte, depletion is to be expected[10, 19]. On neutral surfaces, electrostatic segment repulsion results in weak adsorption[25, 34].

In contrast, the adsorption of polyelectrolytes on oppositely charged surfaces is very strong due to the entropy gain from the release of surface bound counter ions[25]. The polyelectrolyte adsorbs in a flat manner dominated by trains (see Scheme 3.8c) in order to compensate the surface charge[25, 34, 52, 53]. For large polyelectrolytes, the surface charge is always slightly overcompensated[25, 52].

At high salt concentrations, the entropy gain with respect to counter-ions will diminish, the electrostatic interaction is screened and the added ions compete with the polyelectrolyte for adsorption sites[25, 34]. The adsorption will proceed as if the charges were absent in the system[34]. Consequently, without a non-electrostatic attraction ($\chi_S > \chi_S^{Crit}$) between the polymer and the surface, the polymer will be depleted from the surface[34, 52]. We will now consider the adsorption of polyelectrolyte on oppositely charged surfaces where there is an additional van der Waals contribution to the adsorption ($\chi_S > \chi_S^{Crit}$). The polyelectrolyte will adsorb in much higher amounts with a more coiled conformation containing higher fractions of loops and tails (see Scheme 3.8d)[34]. Theory predicts that the surface charge density will be inverted to the same absolute value of charge density or even higher at high salt concentrations[52].

Regarding weak polyelectrolytes, the adsorption is naturally dependent on the degree of dissociation α. Following the discussion above with $\chi_S > \chi_S^{Crit}$, more polymer will adsorb with decreasing α at low salt concentrations and this trend is inverted at high salt concentrations[34].

Polyelectrolyte multilayers

The assembly of polyelectrolyte multilayers (PEM) by alternating Layer-by-Layer (LbL) adsorption of oppositely charged polyelectrolytes is an achievable possibility given the charge inversion discussed above. The LbL adsorption was first proposed by Iler[57] and later developed by Decher on planar macroscopic substrates[58, 59]. The PEM assembly usually entails cycles of polyelectrolyte adsorption from salt solution followed by rinsing with water, with or without salt[54, 56].

There are some requirements that need to be fulfilled in order for the PEM assembly to be successful. The charge overcompensation[52, 54] is one such requirement that has been discussed above. In addition, the first charged layer must be sufficiently anchored[54]. This may be achieved by using intrinsically charged surfaces or by functionalizing the surface with surfactants or polymers where there is a strong non-electrostatic attraction χ_S as previously discussed. Functionalising non-charged microcapsules with anchored charged layers has been the scope of **Paper V-VII**.

The structure and growth of the PEM is usually described by the *zone model*[54]. According to the zone model, the PEM consists of three zones as depicted in Scheme 3.9. Zone I consists of one or a few layers, where the conformation, adsorbed amount and net charge depend on the underlying surface. Zone II is assumed to be more or less homogenous due to interpenetration of oppositely charged polyelectrolytes and therefore neutral. The growth of zone II during the LbL adsorption does not depend on the substrate but rather on the polyanion/polycation pair and salt concentration. Strong polyelectrolytes usually display a linear growth as a function of layer number[54]. On the other hand, weak polyelectrolytes may display an exponential growth at low α due to diffusion of chains into the interior of the PEM[54, 60]. However, when the weak polyelectrolytes are fully charged, a linear growth is observed[60]. Zone III consists of the outermost layers and is to a larger extent affected by the solvent. The sign of the surface charge is determined by Zone III[54].

Scheme 3.9. The zone model and the variation of electrical potential over the PEM.

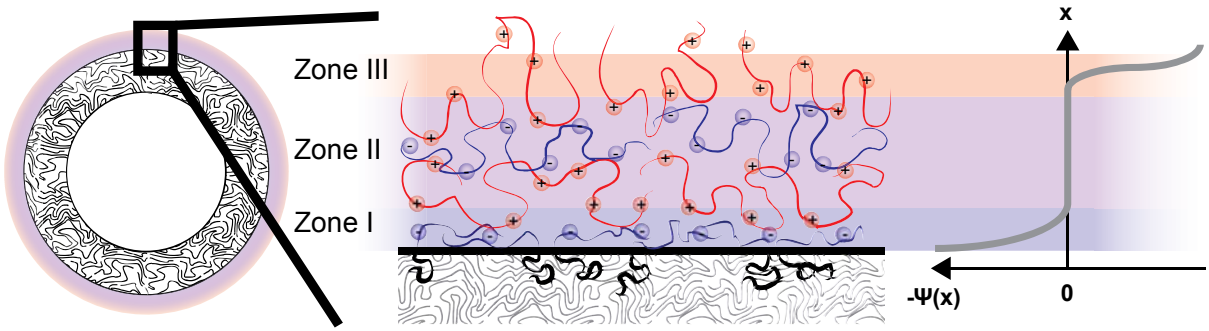

Salt has a profound effect on the structure and growth of the PEM as mentioned above. The adsorbed amount per layer typically increases with the salt concentration[56]. Furthermore, the PEM swells at higher salt concentrations due to the screening of the *electrostatic attraction* (compare with the screening of the *electrostatic repulsion* discussed in chapter 3.2.4)[54]. This may be utilized to *anneal* the PEM since the LbL adsorption is not necessarily an equilibrium process and the individual polyelectrolyte layers are usually kinetically trapped[54].

Following the pioneering work of Möhwald and coworkers[61-65], the PEM assembly has been expanded from planar macroscopic surfaces to microscopic colloidal surfaces[61-68]. The LbL adsorption on colloidal surfaces is more challenging compared to planar macroscopic surfaces since excess polyelectrolytes must be separated from the colloidal particles and bridging flocculation must be avoided[61, 63]. This PEM assembly is usually a prerequisite for the subsequent formation of supported lipid bilayers as discussed in chapter 3.3.1.

The permeability of PEMs requires a short comment. Usually, the higher the charge density of the polyelectrolytes, the denser the polar PEM network will be[69, 70]. Most release applications are involving large polar macromolecules for which the PEM network is semipermeable. Regarding small neutral molecules, the permeability is usually large[55]. Regarding reduced release of small hydrophobic molecules, the requirement of a dense PEM with high charge density is especially important[69, 70]

3.4 Surface and Interfacial Tension

Surface tension, γ, is often explained in terms of the force imbalance at the surface (see Scheme 3.10 and Equation 3.15)[26]. The directional anisotropy of the intermolecular interactions at the surface results in a force acting along the surface normal. The surface tension or energy may also be defined from the *free energy of cohesion*[25, 27].

$$\Delta G^c = -2\gamma_i \qquad 3.15$$

The interfacial tension (a general term including also surface tension) arises also from a force imbalance at the interface, however, with a possible net interaction across the interface. The interfacial tension or interfacial energy may be related to the *free energy of adhesion* (see Scheme 3.10 and Equation 3.16)[25, 27].

$$\Delta G^a = \gamma_{ij} - \left(\gamma_i + \gamma_j\right)$$
$$\gamma_{ij} = \Delta G^a + \gamma_i + \gamma_j \qquad 3.16$$

3.4.1 The van Oss formalism

As explained above, the interfacial energy is a result of intermolecular forces and can therefore be separated into additive contributions (ion-ion, ion-dipole, Keesom, Debey, London dispersion)[71] in a similar manner as for the bulk[27].

Scheme 3.10. Free energy of cohesion of phase *i* and adhesion of phase *i* and *j*. In the present case, *i* represents water and *j* represents an alkane. Water, being bipolar interacts with both Lifshitz and acid-base components. The interaction energy is therefore denoted ε_{ii}^{LW+AB}, following the van Oss formalism. The alkane possesses only London dispersion forces ε_{jj}^{LW} and the interaction between water and alkane can therefore only contain London dispersion components.

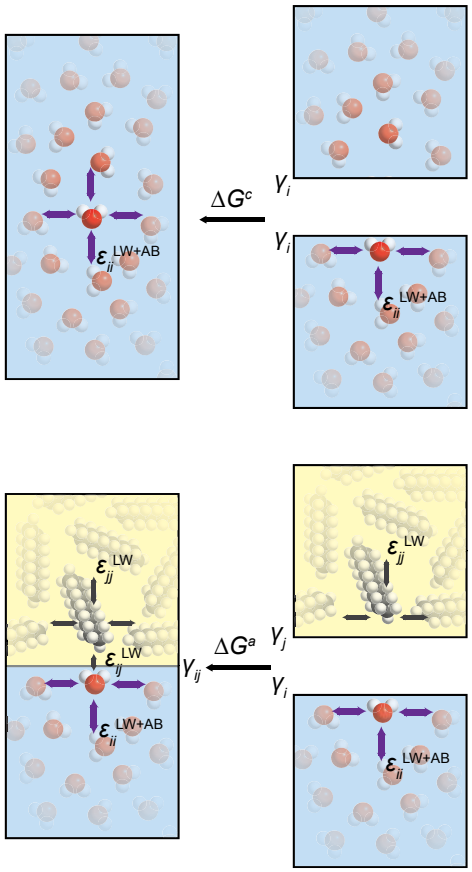

The most simple representation is the separation of the interfacial energy into a dispersive part γ^d and a polar part γ^p as proposed by Fowkes[72]. However, it has been demonstrated that the Debey and Keesom contributions are very small towards the polar contribution[71, 73]. Moreover, the polar contribution is usually overestimated and neglects the more complicated but important contribution from H-bonding[71, 73]. Following the van Oss formalism (Equation 3.17), the apolar γ^{LW} contribution is expressed as the total Lifshitz or van der Waals force and the polar term γ^{AB} accounts only for Lewis acid-base interaction. The polar term is expressed by an acid component γ^+ and a base component γ^- (see Equation 3.18)[71].

$$\gamma_i = \gamma_i^{LW} + \gamma_i^{AB} \qquad 3.17$$

$$\gamma_i^{AB} = 2\sqrt{\gamma_i^+ \gamma_i^-} \qquad 3.18$$

The interfacial tension components may now be expressed by the geometric mean of the usually known surface tension components.

$$\gamma_{ij}^{LW} = \left(\sqrt{\gamma_i^{LW}} + \sqrt{\gamma_j^{LW}}\right)^2 \quad \textbf{3.19}$$

$$\gamma_{ij}^{AB} = 2\left(\sqrt{\gamma_i^+} - \sqrt{\gamma_j^+}\right)\left(\sqrt{\gamma_i^-} - \sqrt{\gamma_j^-}\right) \quad \textbf{3.20}$$

Clearly, γ_{ij}^{LW} will always be positive. However, γ_{ij}^{AB} may attain negative values if *i* is a strong Lewis base and *j* is a strong Lewis acid or vice versa[71]. Such a system comprising a hydrophobic anionic surfactant[74] and a water soluble polycation is discussed in **Paper VII**.

With respect to liquids, a negative interfacial free energy is impossible since the liquid interface cannot store energy (zero shear stress)[71]. In contrast, solid surfaces (nonzero shear stress) may obtain negative interfacial free energies with liquids which is even anticipated for strong Lewis acid-base pairs[71] as described above.

3.4.2 The spreading coefficient and microcapsule formation

For microencapsulation and *core-shell* formation, it is necessary that the polymer (index p) wets the oil (index o) and aqueous phase (index w), i.e. spreads between the oil and water (see Scheme 3.11). The spreading coefficient S_p is defined as;

$$S_p = \Delta G_p^c - \Delta G_p^a = \gamma_{ow} - \left(\gamma_{pw} + \gamma_{op}\right) \quad \textbf{3.21}$$

Scheme 3.11. The microencapsulation process *via* solvent evaporation.

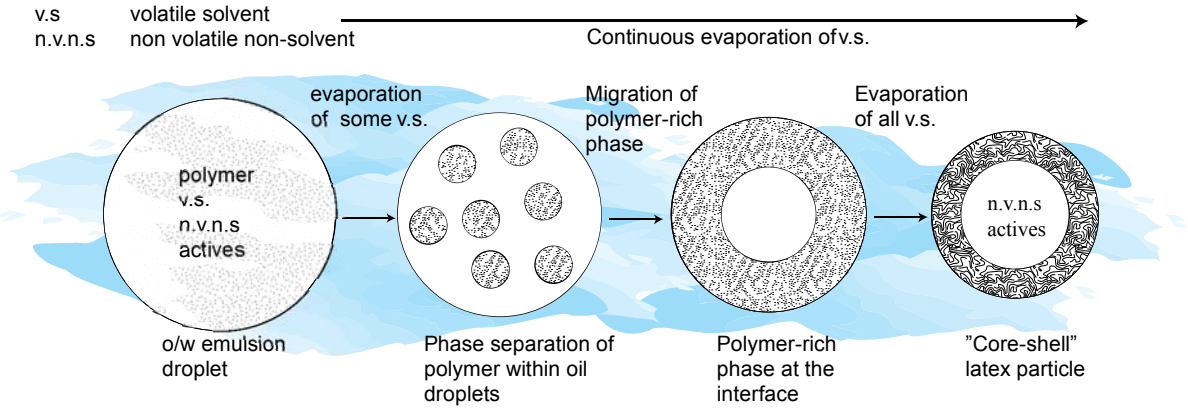

If $S_p>0$, the polymer will spread between the water and oil. The spreading coefficients for the oil and water phase may be derived in a similar manner. Traditionally, it is assumed that $\gamma_{ow}>\gamma_{ow}$ which leads to three possible sets of spreading conditions[13, 75];

$$S_o<0; \quad S_w<0; \quad S_p>0, \quad \textbf{3.22}$$

$$S_o<0; \quad S_w<0; \quad S_p<0, \quad \textbf{3.23}$$

$$S_o<0; \quad S_w>0; \quad S_p<0, \quad \textbf{3.24}$$

The core-shell morphology can only be obtained if the conditions in Equation 3.22 are satisfied. Equation 3.23 will generate so called *acorn particles* (usually formed when surfactants are used as dispersants[13]) and Equation 3.24 will result in separate oil and polymer droplets[12]. It has been suggested that multiple core-shell particles may form when $S_p>>0$[76]. If no oil is added during the encapsulation, a homogenous polymer particle or microsphere will form and the spreading conditions have no meaning.

Scheme 3.12. Possible morphologies and outcomes of the microencapsulation; microsphere or matrix type (a), core-shell particle (b), multiple core-shell particle (c), acorn-shaped particle (d) and droplet separation.

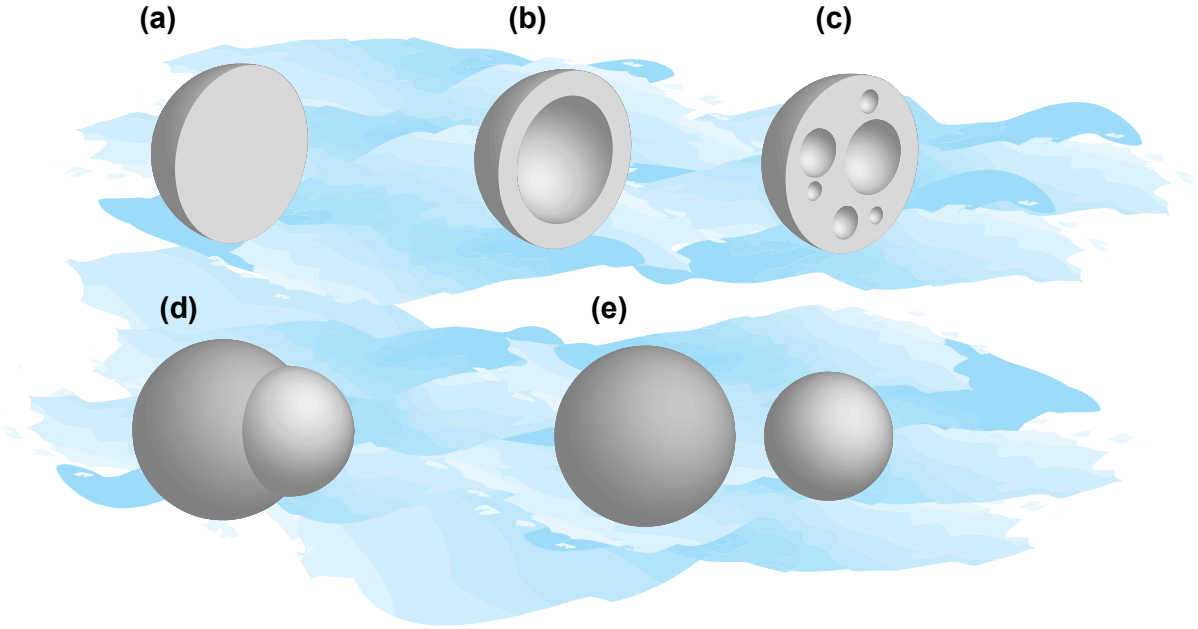

3.5 Colloidal Stability

In this section, only the main contributions to colloidal stability which are relevant to the microcapsule systems are discussed, i.e. electrostatic repulsion, steric repulsion and effect of free polymer. The effects of these interactions for microcapsule have been investigated in **Paper V**, **VI** and **VII**. Other forces such as structural, solvation, hydrodynamic, protrusion and undulation forces have been omitted. The interested reader is referred to the literature[25-27].

3.5.1 Electrostatic stabilization and DLVO theory

The classical DLVO theory, independently elaborated by Deryagin and Landau[77] and Verwey and Overbeek[78], describes the colloidal stability as the interplay between the *attractive van der Waals or Lifshitz interaction* G_{LW} and the *repulsive electrostatic interaction*[25, 27]. The van der Waals interaction for two chemically equivalent spheres with radii r at a closest distance x as displayed in Equation 3.25 is always attractive[28, 29] where H is the Hamaker constant[26].

The electrostatic repulsion arises from the Boltzmann distribution of ions close to a charged surface and is described by the *electric double layer* theory (see Scheme 3.13)[25, 26]. As two spheres of equal size and surface charge density σ_0 approach each other, the diffuse parts of their electric double layer will overlap resulting in a net *osmotic repulsion*[26, 27]. The osmotic repulsion may be obtained through the *Gouy-Chapman* treatment of the ion distribution in the electric double layer[27]. The corresponding interaction energy is displayed in Equation 3.26 following the *Debey-Hückel* approximation[26, 27]. The repulsion is through κ (Equation 3.11) dependent on the salt concentration where κ^{-1} is the thickness (*Debye screening length*) of the diffuse double layer[26]. Added salt will subsequently screen the electrostatic repulsion[25, 26].

$$G_{LW} = -\frac{Hr}{12x} \qquad 3.25$$

$$G_{EL} = 2\pi\varepsilon_0\varepsilon_r\Psi_d^2 \exp(-\kappa x) \qquad 3.26$$

Scheme 3.13. The electric double layer at a charged surface according to Stern theory.

The inner part or the *Stern plane* consists of adsorbed counter ions and the outer, so called *diffuse layer*, consists of Bolzmann distributed ions[26]. The surface charge density σ_0 (Equation 3.27) results in an electrical potential Ψ_0 at the surface which at the Stern plane has decreased to Ψ_d and thereafter decays exponentially with distance (Equation 3.28) according to the *Debey Hückel theory* from the *linearized Poisson-Boltzmann equation* (relevant for low surface potentials, Ψ<26.7 mV at 25°C)[26, 27]. Ψ_0 is normally difficult to measure but Ψ_d may be obtained through electrokinetic measurements[26, 27] (described in chapter 4.5). The electrokinetical potential or ζ-potential is measured at the *surface of shear* x=ζ which is slightly outside the Stern plane[26]. However, the ζ-potential and Ψ_d are usually assumed to be equivalent[26].

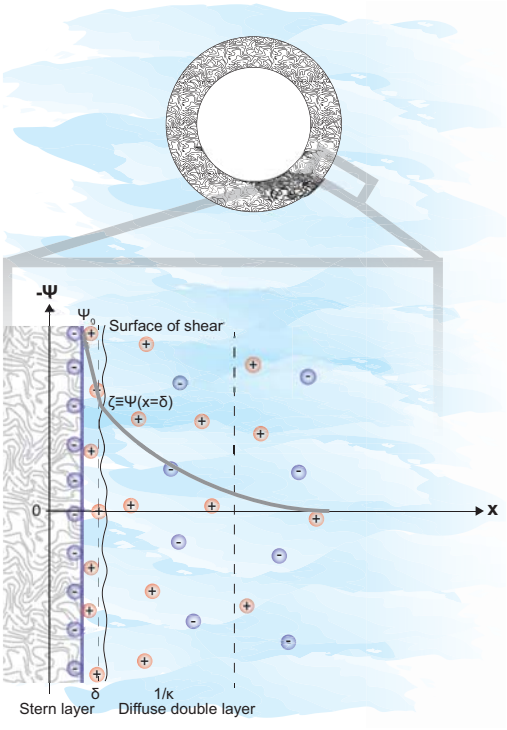

$$\sigma_0 = \varepsilon_0\varepsilon_r\kappa\Psi_0 \qquad 3.27$$

$$\Psi(x) = \Psi_0 \exp(-\kappa x) \qquad 3.28$$

3.5.2 Steric stabilization

Colloidal surfaces with physisorbed or grafted polymers will repel or attract each other depending on the solvent quality when the polymers chains start to overlap In a good solvent, the chains segments repel each other at a distance corresponding to $2R_g$ (Equation 3.5) due to excluded volume effects[34, 51]. The repulsion may be of enthalpic (dehydration) or entropic (reduced conformational freedom) origin or both[26, 51]. This will affect the temperature dependence of the colloidal flocculation. Regarding the polymers used in this work, the dispersants poly(vinyl alcohol) and poly(methacrylic acid) have both been ascribed as enthalpic steric stabilizers (common for aqueous dispersions) indicating that flocculation is to be expected upon heating.

Note that the discussion above is based on polymers at interfaces in *restricted equilibrium*, i.e. the adsorption is irreversible. This is an appropriate assumption for most practical situations. In full equilibrium, a monotonic attraction is predicted at all inter-particle distances[79].

Scheme 3.14. Illustration of polymer interaction at surfaces.

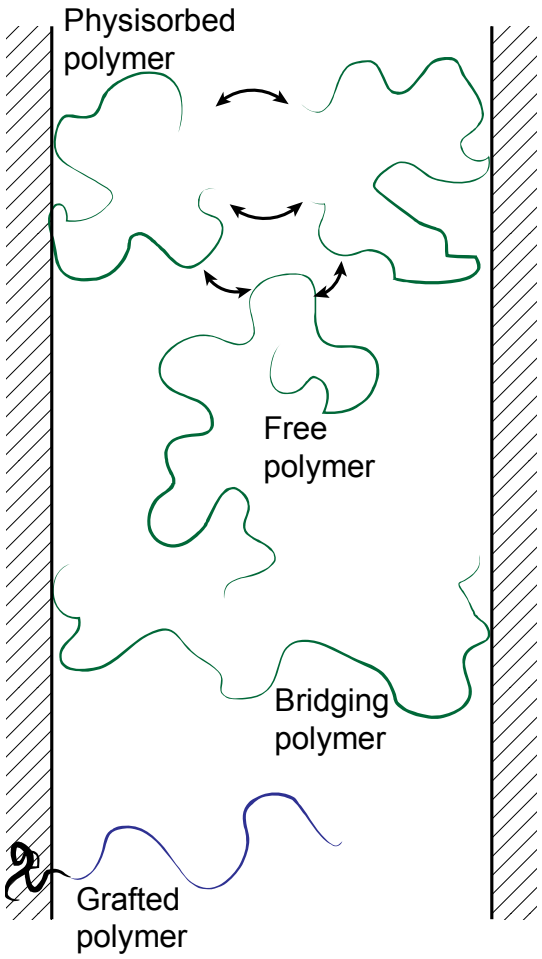

Strong polymer adsorption from a good solvent is to some extent a paradox. The better the solvent, the less prone the polymer will be for adsorption[34, 51]. This problem may be circumvented by using block copolymers[51] as discussed in chapter 3.3.3. The anchor block provides proper adsorption and the buoy block provides good steric stabilization.

A combination of steric and electrostatic stabilization is an efficient avenue to obtain colloidal stability and may be achieved through the use of polyelectrolyte brushes[51]. The long range electrostatic repulsion is attained from the charges introduced by the polymer. In addition, colloidal stability is maintained at high salt concentration through the steric stabilization.

3.5.3 Effect of free polymers

Free polymers in solution will also affect the colloidal stability. It is necessary to here make a distinction between adsorbing and non-adsorbing polymers. Nevertheless, the outcome with respect to colloidal stability is very similar[80].

We will start the discussion with adsorbing polymers. At *low concentrations*, there is a substantial amount of bridge formation (see Scheme 3.14) due to osmotic pressure difference between the surface and the bulk as well as vacant adsorption sites. This will lead to flocculation as two colloidal surfaces approach each

other[80]. At *higher concentrations*, the steric repulsion discussed above will prevent bridge formation[34, 79, 80]. In addition, as two surfaces approach each other, polymer coils trapped in between must contract and leave the inter-particle space[80]. This results in an entropic repulsive barrier due to the reduced conformational freedom of the polymer as well as an osmotic pressure as the polymer is squeezed out[80].

For non-adsorbing polymers, the low concentration regime predicts a net attraction between two colloidal particles due to the depletion force in contrast to the formation of bridges for adsorbing polymers[34, 81, 82]. This is called *depletion flocculation*[34, 81, 82]. However, at higher polymer concentrations, a repulsive barrier will result due to the same reason as for adsorbing polymer[80-82]. This repulsive interaction is therefore often called *depletion stabilization* since it originates from the necessity to deplete the inter-particle space of free polymer in order for two colloidal particles to make contact[81, 82].

3.6 Controlled Release

Controlled release is a concept developed, and most often used, within the pharmacy community[7, 83]. It encompasses a spectrum of different kinetic mechanisms such as *triggered release*, *sustained* or *extended release*, *pulsed release* just to name a few[83]. However, this theoretical section will only cover the subject of sustained release, since this is the mechanism directly connected to the second part of the thesis.

The purpose of sustained release is to let the minimum required amount of the actives be released in order to have a desirable effect. The most efficient and obvious way, in many ways the holy grail of controlled release, to achieve this goal is *zero order release*, i.e. a constant release rate, independent of loading concentration and time[83]. For microcapsules, this is theoretically possible if the actives are dispersed as crystals in the core surrounded by a rate-determining shell[83]. This situation would lead to a core with a constant chemical activity, i.e. concentration, of the active and hence a constant steady-state release (see Scheme 3.15). However, most often the release kinetics follow an initial $\sqrt{t}$ dependence (excluding possible burst or lag releases) followed by conventional exponential first order release[83].

Scheme 3.15. Controlled release from a microcapsule system.

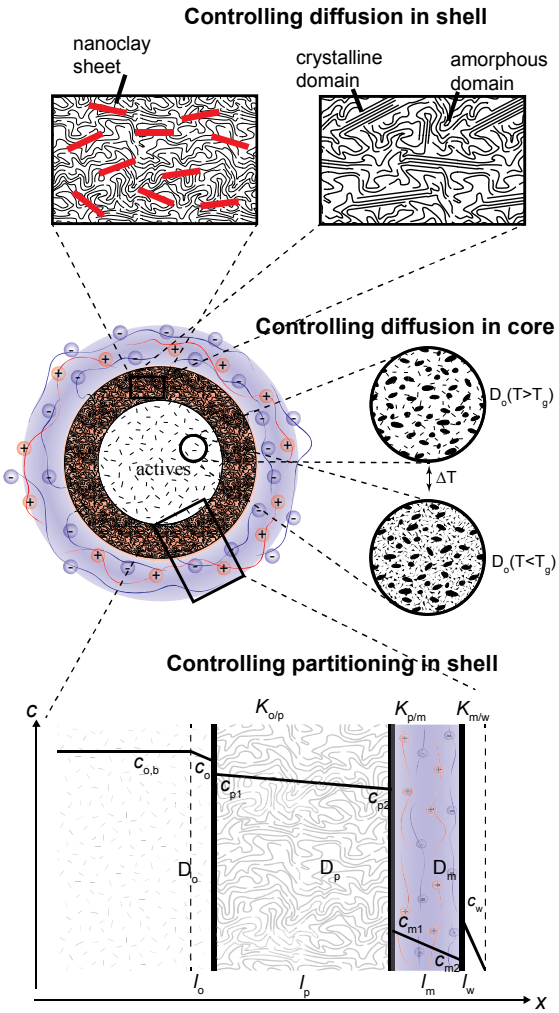

In order to control, or extend, the release from microcapsules the most important parameters controlling the flux of actives must be understood. For convenience, let us model the release of a very hydrophobic substance, *i*, from the microcapsule as a diffusional flux over two membranes (see Scheme 3.15). Under steady state conditions, Fick's first law may be applied and the total flux may be defined by the flux over an arbitrary membrane where D is the diffusion coefficient, Δc is the concentration difference and l is the thickness of the x membrane:

$$J = D_x^i \frac{\Delta c_x^i}{l_x} = \qquad 3.29$$

Moreover, the hydrophobic agent will be distributed between the different phases (core, shells, water). The distribution is determined by the distribution coefficient[c] K which is a thermodynamical constant related to the solubility of the agent[c]. Assuming perfect sink conditions, Equation 3.29 may be rewritten as in Equation 3.30; where r_{TOT} is the total resistance over the membranes (Equation 3.31) where the *permeation*, P, in the membrane is defined as the product of the diffusion coefficient of the agent in the membrane and the distribution coefficient of the agent between the membrane phase and the adjacent phase.

$$J = \frac{c_{o,b}}{r_{TOT}} \qquad \textbf{3.30}$$

$$r_{TOT} = r_o + r_p + r_m + r_w = \frac{l_o}{D_o^i} + \frac{l_p}{D_p^i K_{p/o}^i} + \frac{l_m}{D_m^i K_{m/o}^i} + \frac{l_w}{D_w^i K_{w/o}^i} \qquad \textbf{3.31}$$

$$= \frac{l_o}{P_o^i} + \frac{l_p}{P_p^i} + \frac{l_m}{P_m^i} + \frac{l_w}{P_w^i}$$

With this definition in mind, it is clear that the permeation of agent *i* may be altered either kinetically through the diffusion constant and/or thermodynamically by the solubility in the membrane.

The diffusion in a polymer membrane may be reduced for instance by cross-linking the polymer or by increasing the crystallinity[84] (see Scheme 3.15). Within our group, we have evaluated the incorporation of hydrophobically modified nanoclays[85] as means for obstructing the diffusion (unpublished), yet with minor improvement. In contrast, an improvement is observed when using solid oils instead of liquid oils[86] (see Scheme 3.15).

As discussed in chapter 3.3.4, the use of PEMs as hydrophilic barrier against hydrophobic molecules is intended to affect the K rather than D (see Scheme 3.15). Therefore, this method for extended release investigated in this work may be regarded as a thermodynamic approach in contrast to the kinetical approaches discussed above.

---

[c]The distribution coefficient is defined as;

$$K_{A/B}^i = \frac{c_A^i}{c_B^i} = \frac{1}{K_{B/A}^i}$$

The chemical potential for a saturated solution of agent *i* in phase A is:

$$\mu_l^i = \mu_A^{\circ,i} + RT \ln c_A^{s,i}$$

Where $\mu^i{}_l$ is the chemical potential of pure agent i, $\mu^{o,i}{}_A$ is the standard chemical potential and $c^{s,i}{}_A$ is the saturation concentration. The chemical potential of agent *i* distributed between two phases A and B is given by:

$$\mu_A^{\circ,i} + RT \ln c_A^i = \mu_B^{\circ,i} + RT \ln c_B^i$$

Combination of the equations above leads to:

$$\ln \frac{1}{c_A^{s,i}} = \ln K_{A/B}^i + \frac{\mu_B^{\circ,i} - \mu_l^i}{RT}$$

CHAPTER 4

Experimental Considerations

In this thesis, the materials related to coordination chemistry have been characterized using EPR, vibrational spectroscopy (far-FTIR and mid-FTIR), *ab initio* and DFT calculations. The polymeric properties have been characterized using mainly DSC and vibrational spectroscopy.

The microcapsules in the second part of the thesis have been directly characterized using in particular microelectrophoresis in addition to standard analytical techniques such as optical microscopy. Moreover, the microcapsule system and models thereof have been analysed using optical tensiometry and QCM-D measurements.

4.1 Electron Paramagnetic Resonance Spectroscopy

A charged object subjected to movement, such as a spinning electron, is associated with a magnetic moment. Most substances contain orbital paired electrons in chemical bonds etc. Since the spins of paired electron are opposed, the net magnetic moment is cancelled out. However, radicals and transition metals with unpaired electrons may have a net magnetic moment and are often labelled *paramagnetic*[87, 88]. The EPR resonance conditions is fulfilled when the spin excitation energy ΔE in a magnetic field H_r equals electromagnetic radiation energy $h\nu$ according to $\Delta E = g\beta H_r = h\nu$ where β is the Bohr magneton and g is the so called g-factor described below. Usually the magnetic field is sweeped and the radiation frequency is kept constant[87, 88].

Some features are generic for the EPR spectra, e.g. the g-factor and hyperfine splitting, and will be discussed below and related to the specific case of Cu^{2+} ions. Furthermore, the delocalization of the unpaired electron in Cu^{2+} and it's interaction with the ligand nuclei will be covered to some extent.

Scheme 4.1. Major EPR related interaction in Cu^{2+} complexes.

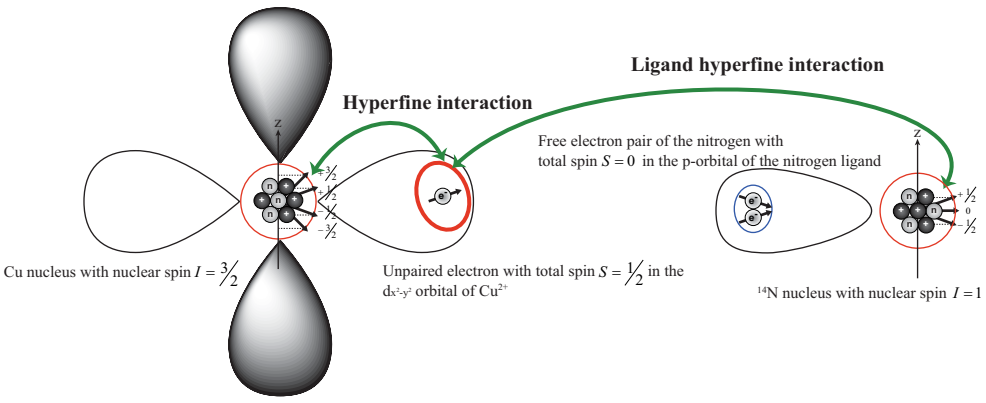

Scheme 4.2. EPR resonance condition and effect of nuclear hyperfine interaction.

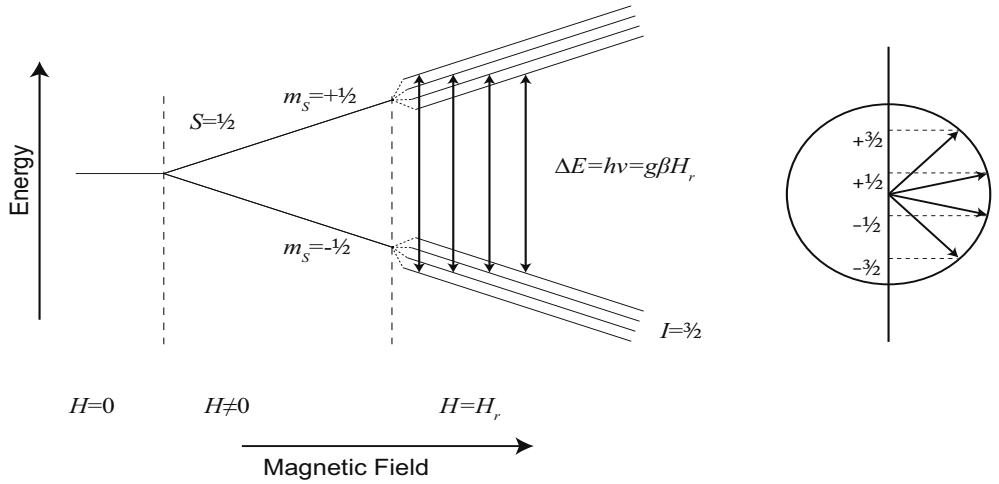

4.1.1 The *g*-factor

The *g*-factor of a free electron, g_e=2.00232, is a universal constant and characteristic of the electron. The external magnetic field will however induce an *internal* magnetic field in the sample, causing the *g*-factor to deviate[87, 88]. The *g*-factor of a specific species may hence be considered as characteristic of the chemical surrounding, similar to the chemical shift in NMR, and transition metal ions are to a large extent affected by the surrounding ligands[19, 87, 88].

The main source of deviation from g_e is due to the coupling with the electron orbital magnetic moment[87]. This effect, called *spin orbit coupling* is very strong for transition metal ions and is characterized by the *spin orbit coupling constant* λ_0 (-830 cm^{-1} for Cu^{2+})[19, 87]. If the atomic shell is less than half full, then $\lambda_0>0$ and $g<g_e$. Conversely, if the atomic shell is more than half full, then $\lambda_0<0$ and $g>g_e$. The ligand field splitting, Δ_{max}, discussed in chapter 3.1, is approximately 600 nm for Cu^{2+} but is strongly dependant on the chemical nature of the surrounding ligands[19]. The *g*-factor may be expressed as in Equation 4.1 where *k* is a constant.

$$g = g_e\left(1 - k\frac{\lambda_0}{\Delta_{max}}\right) \qquad \textbf{4.1}$$

The spin orbit coupling usually renders the *g*-factor anisotropic, especially for transition metal ions where the unpaired electrons are residing in d-orbitals[87]. The *g*-factor is therefore represented by a tensor; g=[g_{XX}, g_{YY}, g_{ZZ}]

Axial symmetry is found in many transition metals, where $g_{XX}=g_{YY}\neq g_{ZZ}$. Since g_{XX} and g_{YY} are perpendicular and g_{ZZ} is parallel to the symmetry axis, the perpendicular contribution is by convention designated as $g_\perp= g_{XX}=g_{YY}$ and the parallel contribution as $g_\parallel=g_{ZZ}$. Lower symmetry, when $g_{XX}\neq g_{YY}\neq g_{ZZ}$, is labelled rhombic symmetry[19, 87]. The *g*-factor may be isotropic, i.e. $g_{XX}=g_{YY}=g_{ZZ}$, in low viscous liquids if the molecular tumbling is fast enough[87].

Regarding Cu^{2+}, *k*=4 or 1 when the external magnetic field is parallel ($g_\parallel$) or perpendicular ($g_\perp$) to the symmetry axis resulting in $g_\parallel>g_\perp$[19].

The larger deviation of $g_{\|}$ (from g_e) compared to $g_{\perp}$ is due to the difference in orbital angular moment. The unpaired electron in $d_{x^2-y^2}$ may gain angular moment around the z-axis (axis of symmetry) by spending some time in d_{xy}. Angular moment around the x or y-axis is possible by mixing of d_{xz} or d_{yz} with $d_{x^2-y^2}$ but this is not at all as effective[19].

4.1.2 Hyperfine interaction and delocalization

As discussed above, the g-factor deviates due to local magnetic fields induced by the external magnetic field. There are however also *permanent* magnetic fields, which are not dependant on the external field, generated by e.g. other electron magnetic moments but most often nuclear magnetic moments. The interaction between the unpaired electron and the nuclear magnetic moment is termed hyperfine interaction[87, 88].

The nucleus has a characteristic nuclear spin, I, which for odd atomic number and even atomic mass is an integer while an odd atomic mass generates a half odd integer[f]. The nuclear spin quantum number may obtain $2I+1$ number of spin states (m_I=$-I$, $-I+1$, …, $I-1$, I) and subsequently generates the same number of local magnetic fields, H_{local} (see Scheme 4.2)[87, 88]. The local magnetic fields split the signal in $2I+1$ number of signals which is termed hyperfine splitting and the interval between the signals is typically designated as the *hyperfine splitting constant*[87].

$$H_r = H' - H_{\text{local}} = H' - am_I \qquad \textbf{4.2}$$

The same considerations regarding the anisotropy of the g-factor apply for the anisotropy of the hyperfine interaction. The hyperfine interaction is defined by the hyperfine tensor $\boldsymbol{A}$, which for axial symmetry contains $A_{\perp}=A_{XX}=A_{YY}$ and $A_{\|}=A_{ZZ}$[87, 88]. In liquid solutions the anisotropic value vanishes due to averaging and only the isotropic hyperfine splitting remains. If the hyperfine splitting is not large enough in comparison with the line broadening, a lot of structure will be lost in a poorly resolved signal[87]. Regarding copper, the two isotopes ^{63}Cu and ^{65}Cu have both I=3/2 and approximately the same magnetic moment[g]. Normally $|A_{\|}|>|A_{\perp}|$ and the $A_{\perp}$ features are generally poorly resolved in the perpendicular region of the spectrum[19].

Ligand hyperfine interaction

Ligand hyperfine coupling, sometimes labelled super hyperfine coupling, may arise due to dipole-dipol and Fermi contact interaction between the unpaired electron of the transition metal and the ligand nucleus. Since the unpaired electron is residing in $d_{x^2-y^2}$, only coupling to equatorial ligands is to be expected[19, 87]. Paramagnetic Cu(II) with a net electron spin of S=1/2 surrounded by n equivalent ligands with nuclear spin I will result in a total number of signals[87, 88];

$$2nI+1 \qquad \textbf{4.3}$$

[f] A nucleus with even atomic number and mass has I=0 resulting in absence of hyperfine interaction.

[g] The magnetogyric ratios of ^{63}Cu and ^{65}Cu are slightly different. Fine structure may be lost if not isotope pure Cu is being used..

with the relative intensity given by the binomial coefficient of the expansion where $c_i = n!/[(n-i)!i!]$;

$$(a+b)^{2nI} = \sum_{i=0}^{i=2nI} c_i a^{2nI-i} b^i \qquad \textbf{4.4}$$

Regarding four equivalent ^{14}N ligand with nuclear spin $I=1$, nine signals are to be expected with the relative intensity [1:8:28:56:70:56:28:8:1]. This large number of signals may be hard to resolve. More intricate studies of the ligand hyperfine interaction subsequently utilizes ^{15}N ligand ($I=1/2$) resulting in five, better resolved signals [1:4:6:4:1][19, 88, 89].

Delocalization

The ligand hyperfine interaction discussed above is closely related to the delocalization of the unpaired electron to the surrounding ligands. An increased covalence between the metal and ligand indicate more delocalization of the unpaired electron to the ligand and hence more hyperfine interaction with the coordinating ligand nuclei[19].

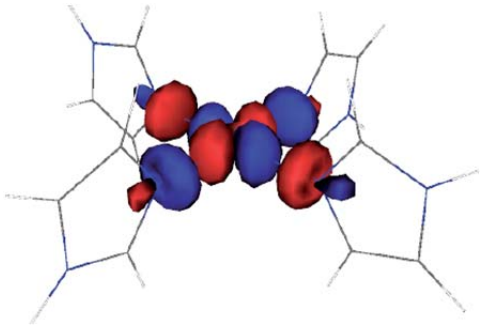

Figure 4.1. Molecular orbital of the unpaired electron in $[CuIm_4Cl_2]$ (**Paper II**).

The delocalization effect has implication on the g-factor. Typical g-values are usually lower than the ones predicted by Equation 4.1 which is a result of delocalization of the unpaired electron[19]. Equation 4.1 may hence be extended to incorporate the degree of covalence, i.e. delocalization where α^2 is a measure of the extent of $d_{x^2-y^2}$ character in the molecular orbital formed between the metal and ligand. More covalence in the σ-bond denotes more delocalization, i.e. lower α-value, of the unpaired electron to the ligand and hence a smaller $g_{\|}$ value[19].

$$g_{\|} = g_e\left(1 - k\frac{\alpha^2\lambda_0}{\Delta_{\max}}\right) \qquad \textbf{4.5}$$

A more elaborate model to obtain the covalency was developed by Kievelson and Nieman[90].

$$\alpha^2 = -\left(\frac{A_{\|}}{P}\right) + \left(g_{\|} - 2.0023\right) + \frac{3}{7}\left(g_{\perp} - 2.0023\right) + 0.04 \qquad \textbf{4.6}$$

P denotes the interaction dipolar term of the free ion (0.036 cm^{-1}). $\alpha^2=1$ for a completely ionic bond whereas $\alpha^2=0.5$ for a completely covalent bond. The in plane and out of plane π-bond coefficient, β and γ, may be obtained from Equation 4.7 and 4.8[2, 4].

$$\alpha^2\beta^2 = \left[\left(g_{\|} - 2.0023\right)\Delta_{\|}\right]/8\lambda_0 \qquad \textbf{4.7}$$

$$\alpha^2\gamma^2 = \left[\left(g_{\perp} - 2.0023\right)\Delta_{\perp}\right]/2\lambda_0 \qquad \textbf{4.8}$$

Here, $\Delta_{\|}$ and $\Delta_{\perp}$ are the orbital electronic excitation energy $B_{2g} \leftarrow B_{1g}$ or $d_{x^2-y^2} \leftarrow d_{xy}$ and $B_{2g} \leftarrow E_{1g}$ or $d_{x^2-y^2} \leftarrow d_{xz}$ which may be obtained from UV-vis measurements.

4.2 Differential Scanning Calorimetry

Differential scanning calorimetry (DSC) is tool for thermal analysis of materials. Phase transitions such as; glass transitions, crystallization, melting, curing processes etc. may be monitored qualitatively and quantitatively (see Scheme 4.3a)[33, 91]. In this project a *power compensated* DSC has been used. Unlike DTA (differential thermal analysis) or *heat flux* DSC which measures the temperature difference between the sample and a reference sample, DSC measures the heat input[h] required to keep the sample and the reference in thermal equilibrium (see Scheme 4.3b). Pure changes in thermodynamic energy are hence probed and the area under the peaks in the thermogram is directly proportional to the enthalpic change in the sample[33, 91].

$$\Delta q(T) \approx -\Delta H(T) \qquad \textbf{4.9}$$

Scheme 4.3. (a) Schematic DSC thermogram, (b) DSC measurement cell

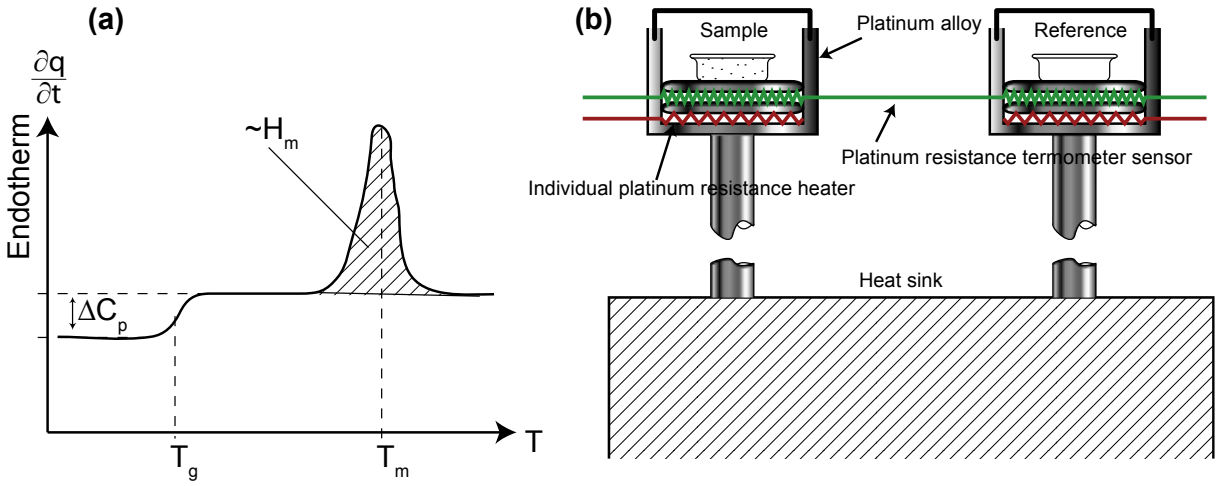

The glass transition is typically accompanied with a change in specific heat capacity, C_p[i] (see Scheme 4.3a). This is due to the increased rotational and at even higher temperature, translational freedom[33, 91, 92]. The glass transition temperature, T_g, is subsequently monitored as a heat capacity jump in the thermogram (see Scheme 4.3).

$$dq(T) = C_p dT \qquad \textbf{4.10}$$

Since the heat flux corresponding to the enthalpy change depends on the heating rate, v=dT/dt, the signal may be enhanced by increasing the heating rate (see eq. 5.18). However, as the heating rate is increased, an increased *thermal lag* is introduced which raises the measured T_g from the true T_g. The thermal lag has

[h] To be more precise, the heat flow rate, $\frac{dq(T)}{dt}$ is measured with DSC.

[i] The conditions during a DSC measurement may be considered to be under constant pressure, and $\mathbf{C_p}$ is subsequently probed.

instrumental origins[i] as well as physical due to the kinetic nature of the glass transition (unlike true, 1:st order transitions such as melting). To obtain true transition temperatures, the thermogram may be extrapolated to zero heating rate. However, for standard measurements such as T_g determination, it is often sufficient to measure at low heating rates (0-10 K/min)[91].

$$H(T) - H(T_0) = \int_{T_0}^{T} C_p(T)dT = \int_{T_0}^{T} \frac{dq(T)}{dt}\frac{dT}{v} = \Delta H \qquad \textbf{4.11}$$

[i] $\frac{dH}{dt} = -\frac{dq}{dt} + \overbrace{(C_s - C_r)\frac{dT}{dt}}^{\text{Baseline displacement}} - \overbrace{RC_s\frac{d^2q}{dt^2}}^{\text{Thermal lag}}$

The baseline displacement is easily corrected by subtracting the thermogram with a baseline, i.e. the thermogram of an empty sample. The thermal lag is reduced by using low thermal masses (reduces R, the thermal resistance) and small sample masses (reduces C_s, the heat capacity of the sample).

4.3 Vibrational Spectroscopy

A molecule possesses three types of motion; *translation*, *rotation* and *vibration*. The molecular vibration is quantisized in discrete energy levels (see Scheme 4.4) and the vibrational motion may be described as a harmonic oscillation of atoms connected by springs obeying Hooke's law[93, 94].

Scheme 4.4. (a) Model for molecular vibrations. (b) Potential well

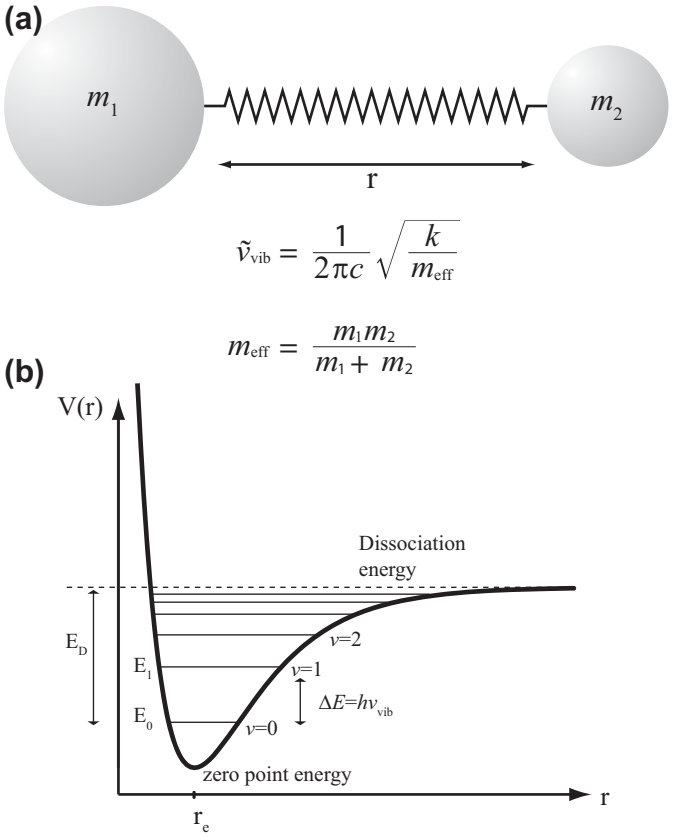

The resonance condition for a vibrational excitation requires that the frequency of the radiation equals that of the vibration and that the dipole moment of the atoms involved in the vibration changes (Equation 4.12).

$$\frac{\partial \mu}{\partial r} \neq 0 \qquad \textbf{4.12}$$

A vibrating molecule with an oscillating dipole moment μ induces an electrical field, oscillating with the same frequency as the frequency of the vibration. The oscillating electric field of the vibrating dipole will then interact with the electric component of the radiation field. Moreover, only transitions v=0⟶1 (see Scheme 4.4) are relevant due to selection rules and Bolzmann distribution[k,93,94]

A non-linear molecule possesses 3N-6[l] modes of vibration (a linear possesses 3N-5 modes of vibration) where N is the number of atoms. A polymer possesses 3n or less vibration modes where n is the number of atoms in the repeating unit which significantly simplifies the spectrum. The vibrations are usually designated according to the specific mode of deformation (see Table 4.1). The vibrational energies usually follow the order; $v>\delta>\gamma>\tau$ (see Table 4.1). As a result of the resonance condition discussed above, polar bonds usually display high signal intensity I of absorption[93] according to Equation 4.12.

$$I \propto \left(\frac{\partial \mu}{\partial r}\right)^2 \qquad \textbf{4.13}$$

Table 4.1. Vibrational designations.

Vibrational modes		
Symbol	Name	Mode of deformation
v	Stretch	Stretching of valence bond
δ	In plane bend	1 or more bond angle changes, constant bond length.
γ	Out of plane bend	1 atom oscillates through a plane of at least 3 atoms.
τ	Torsion	Dihedral angle is changed

The force constant k (see Scheme 4.4) as a measure of the bond strength requires a short comment. k is measure of the curvature of the potential well describing the bond stiffness whereas the bond strength is related to the dissociation energy E_d, i.e. the depth of the well (see Scheme 4.4). There's however a relationship between E_d and k, and within the same series of bonding atoms, k is a measure of bond strength[94].

Within this work, the molecular vibrations have been studied by FTIR (Fourier Transform Infrared Spectroscopy). FTIR is usually, due to instrumental/technical reasons divided into near- (4000-14000 cm^{-1}), mid- (400-4000 cm^{-1}) and far-FTIR (10-400 cm^{-1}) and the prefix is related to the frequency of the infrared light. The difference in frequency-intervals between the three methods implies that different sources of light as well as sample preparation methods are needed. Typically, normal vibrational modes are studied with mid-FTIR, near-FTIR studies normal vibrational modes, overtones and low energy electronic excitation whereas far-FTIR studies rotaion, low energy deformation modes and vibration of weaker bonds such as ionic bonds, coordinate bonds etc[95].

[k] The harmonic approximation allows only $v\pm1$ transitions and the slight anharmonic distortion results in only weak intensities of excitations corresponding to $\Delta v>1$. At room temperature, $kT/hc\approx200$ cm^{-1} which is far below most mid-IR vibration and most molecules will hence be in the vibrational ground state $\upsilon=0$.

[l] Three are pure translational and three are pure rotational modes of motion. A linear molecule has only two modes of rotation.

4.4 *Ab Initio* Calculations

Ab initio models are pure quantum mechanical models used to calculate e.g. binding and reaction energies, molecular geometries (bond lengths, bond vibrations) acidity, bond strength and covalence[96]. As pure quantum mechanical models containing no empirical data (*ab inito*="from the beginning"), their construction traces back to the many-body Schrödinger equation (Equation 4.14) where $\hat{H}$ is the Hameltonian describing the kinetic and potential energy of electrons and nuclei, Ψ is the many-electron wave function and E is the total energy of the system[96, 97].

$$\hat{H}\Psi = E\Psi \qquad 4.14$$

Equation 4.14 cannot be solved for a many-electron system so approximations must be applied. The first, so called *Born-Oppenheimer approximation* assumes that the nuclei are stationary, which is reasonably due to the much larger mass of the nucleus compared to the electron, leading to the electronic Schrödinger equation[97].

4.4.1 Hartree-Fock methods

The second, so called *Hartree-Fock approximation*, replaces the many-electron wave function with a single electron wave function which is the product of a space part, also termed molecular orbital, Ψ, and a spin part, α or β. Each molecular orbital may contain no more than two electrons of opposite spins[96]. The resulting set of coupled differential equations may be solved numerically but typically, the classical *LCAO approximation* (Linear Combination of Atomic Orbitals) is introduced[96, 97]. The LCAO approximation assumes that the molecular orbitals are linear combinations of the atomic orbitals φ also called *basis functions*, from the solutions to the Schrödinger equation for the hydrogen atom. In practice during calculations, a finite set of basis functions are used called *basis set* (see below).

$$\Psi_i = \sum_{\mu}^{\text{basis function}} c_{\mu i}\varphi_{\mu} \qquad 4.15$$

The resulting total Hartree-Fock (HF) energy:

$$E^{HF} = E^{\text{nuclear}} + E^{\text{core}} + E^{\text{Coloumb}} + E^{\text{exchange}} \qquad 4.16$$

contains a part accounting for the nuclei, E^{nuclear}, for the kinetic and potential energies of individual electrons, E^{core}, and for the Coloumbic interaction between electrons, E^{Coloumb}. The last term, E^{exchange}, is an *electron correlation* term called *electron exchange* and purely quantum mechanical in nature. The electron exchange accounts for the reduction of the electron-electron repulsion derived from a classical Coloumbic interaction. However all electron correlations are not taken into account in HF methods leading to a resulting total energy of the system that is higher than the experimental one[97]. Consequently, HF methods are limited for calculation of reaction energies involving bond breaking/formation or transition metal compound structures, but excellent for calculation of ground state conformation and conformational energy differences[97].

4.4.2 Density functional theory methods

Density functional theory (DFT) is not an *ab initio* method *per se* since it takes electron correlations into account using a semi-empirical approach[98]. The density functional theory states that the energy of a system may be described by the electron density (rather than the sum of single electron wave functions)[98]. This was proven by the *Hohenberg-Kohn theorem*[99] and later developed using the *Kohn-Sham formalism*[100] with the introduction of atomic orbitals. The electron density $p(\mathrm{r})$ is described by a set of one electron molecular orbitals called Kohn-Sham orbitals Ψ[97, 98]:

$$\rho(r) = \sum_{i=1}^{n} |\Psi_i(r_i)|^2 \qquad \textbf{4.17}$$

The Kohn-Sham orbitals are linear combination of the same basis functions, i.e. atomic orbitals, used in the HF calculation. The resulting DFT energy:

$$\mathrm{E}^{\mathrm{DFT}} = \mathrm{E}^{\mathrm{nuclear}} + \mathrm{E}^{\mathrm{core}} + \mathrm{E}^{\mathrm{Coloumb}} + \mathrm{E}^{\mathrm{XC}} \qquad \textbf{4.18}$$

contains the same terms as the HF counterpart but the pure electron exchange term is replaced with an electron correlation term as discussed above[97, 98]. Since electron correlations are taken into account, DFT methods are well suited for equilibrium geometries, reaction energies involving bond breaking/formation[98].

4.4.3 Hybrid functionals

The DFT hybrid functionals are a certain type of functionals containing a term of exact exchange from HF theory and hence *ab initio* in the electron exchange-correlation function[98]. An example is the B3LYP functional[101, 102] (Becke, Lee, Yang, Parr and 3 parameters in the exchange-correlation term) which is very popular within the chemistry community due to its versatile performance[98]. Bond lengths and vibrations for neutral molecules are estimated with excellent precision and the accuracy of geometry and binding energy calculations for transition metal compounds is very high[98].

4.4.4 Basis sets

In this work, both regarding HF and DFT calculations, a Gaussian basis set has been used which is closely related to the exact solution of the Schrödinger equation for the hydrogen atom as described above. The functions are polynomials of Cartesian coordinates followed by an exponential in r^2. [96-98]

The *polarization basis set* 6-31G* was used for ligands calculated using HF and ligands and coordination complexes calculated using DFT, A polarization basis set includes six d-type orbitals and allows for electron distribution centred away from the nucleus as well as hybrid orbitals in contrast to the minimal basis sets or split-valence basis sets[96].

The *pseudopotential basis set* LACVP[103] (Los Alamos National Library) was used for coordination complexes calculated using HF. This is useful since the calculations are simplified by only taking the valence electrons into account and replacing the core electrons with a potential[103]. The LACVP basis set include in addition to the valence electron (3d4s orbital for Cu and Zn) also the highest outermost core orbitals (4p5s4d5p for Cu and Zn)[103].

4.5 Microelectrophoresis

Electrophoresis is the study of the movement of charged surfaces, defined by the ζ-potential (see chapter 3.5.1), relative a stationary liquid[26, 27]. For large particles (such as microcapsules), the measurements are typically performed in a microelectrophoresis cell[26] as depicted in Scheme 4.5. The detection of the particle movement is somewhat complicated by the simultaneous electroosmotic flow and compensating counter flow since the wall is usually charged (see Scheme 4.5)[26, 27]. The particle movement of large particles is usually detected by dark field microscopy (>0.6 μm, see Scheme 4.5) whereas the particle movement of smaller particles (<0.6 μm) may be obtained by measuring the laser Doppler shift from dynamic light scattering (DLS)[26].

The ζ-potential is calculated from the Hückel equation (Equation 4.19) or the Smoluchowski equation (Equation 4.20) where u_E is the electrophoretic mobility, v_E the particle velocity in a liquid with viscosity η and an applied field E[26, 27]. The radius of the particle is r and the remaining parameters have been defined in chapter 3.2.4. The Hückel equation is derived by balancing the viscous forces obtained from the Stokes-Einstein equation with the electrical forces[26, 27]. The equation is only valid for $\kappa r<0.1$ and is subsequently rather inapplicable even for nanoparticles in aqueous media since the requirement for extremely low salt concentrations is difficult to accomplish[26]. The Smoluchowski equation may be used when the particle radius is much larger than the Debye screening length ($\kappa r>100$). The equation is obtained by balancing the viscous and electrical forces at a planar surface[26, 27].

Scheme 4.5. Electrophoresis cell.

The movement of the particles has in this work been measured using dark field microscopy. Only scattered light is obtained which increases the contrast of the image. The focus of the microscope must be placed at the *stationary point* where the electro-osmotic flow is cancelled by the counter-flow. The position of the stationary point depends on the tube geometry and is for cylinders 0.146 of the inner tube diameter[26].

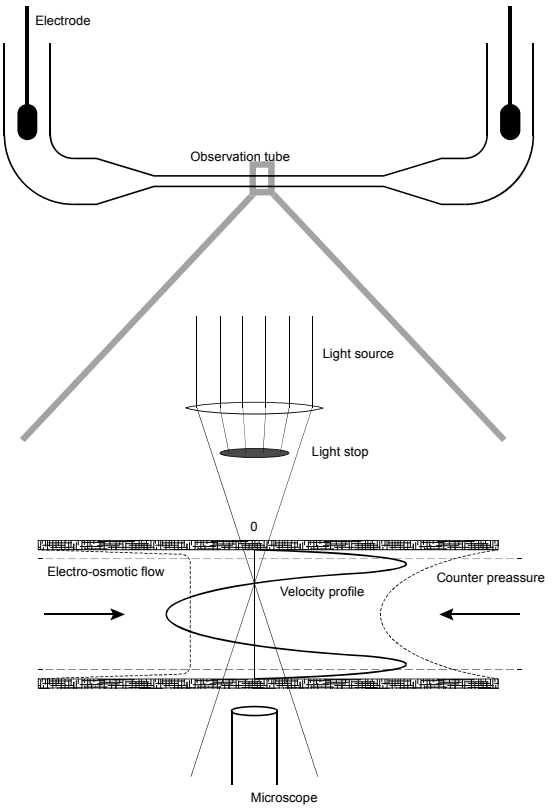

$$u_E = \frac{v_E}{E} = \frac{\varepsilon_r \varepsilon_0 \zeta}{\eta} \qquad \textbf{4.19}$$

$$\frac{v_E}{E} = \frac{\varepsilon_r \varepsilon_0 \zeta}{1.5\eta} \qquad \textbf{4.20}$$

4.6 Optical Tensiometry

Surface, interfacial tensions, contact angles and surface free energies may be obtained using optical tensiometry through image analysis[25, 26]. Regarding surface and interfacial tensions of liquids, the method is usually referred to as the *pendant drop technique*[25, 26, 104]. The surface/interfacial tension γ_{LF} is obtained by fitting the shape of the droplet with Equation 4.21 where $\Delta\rho$ is the density difference between the drop and the surrounding fluid, g the gravitational constant, R_0 the radius at the drop apex and β the shape factor[26, 104].

$$\gamma_{LF} = \Delta\rho g \frac{R_0^2}{\beta} \qquad 4.21$$

4.6.1 Contact Angle

Using the image analysis as described above, the contact angle between a liquid drop and a solid or liquid substrate in a fluid (liquid or vapour) may be measured. For smooth and flat solid surfaces (index S), the contact angle of a liquid (index L) in a fluid (index F) is related to the interfacial tensions/free energies γ_{SF}, γ_{SL} and γ_{LF}, through the force balance known as the *Young equation* (Equation 4.22 and Scheme 4.6). If the fluid is vapour/air, the index F is usually omitted.

$$\gamma_{SF} = \gamma_{SL} + \gamma_{LF}\cos\phi \qquad 4.22$$

4.6.2 Surface Free Energy Calculations

Contact angle measurements as described above may be used to determine the surface/interfacial free energy of solids. However, regarding an unspecified solid, Equation 4.22 contains two unknowns, i.e. γ_{SF} and γ_{SL}. For low energy surface, a *Zisman plot*[105] may be used where the critical surface tension $\gamma_c \approx \gamma_S$ is obtained by extrapolating $\gamma(\cos\phi)$ to $\cos\phi \rightarrow 1$ for a set of non-wetting liquids.

Scheme 4.6. Illustration of a pendant drop and a drop on a solid surface with contact angle ϕ.

Equation 4.22 is based on the Young-Laplace equation (Equation 4.23) where R_1 and R_2 are the radii of curvature. The shape factor is obtained from the coupled first order differential equations 4.24, 4.25 and 4.26[104].

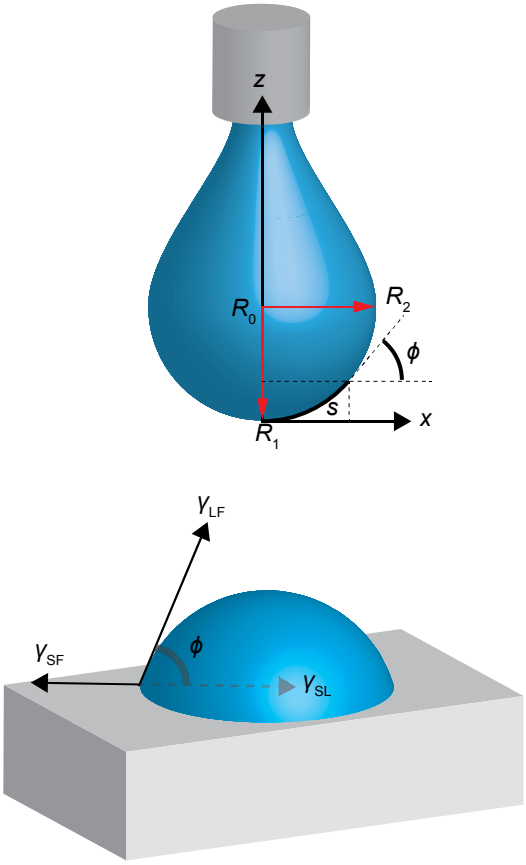

$$\gamma_{LF}\left(\frac{1}{R_1} + \frac{1}{R_2}\right) = \frac{2\gamma_{LF}}{R_0} + \Delta\rho g z \qquad 4.23$$

$$dx/ds = \cos\phi \qquad 4.24$$

$$dz/ds = \sin\phi \qquad 4.25$$

$$d\phi/ds = 2 + \beta z - \frac{\sin\phi}{x} \qquad 4.26$$

The Zisman plot is only applicable as long as the γ_{SL} interfacial free energy is negligible (which is usually the case for low energy surface). For high energy surfaces, a number of different theories may be used to model the γ_{SL} interfacial free energy from the γ_S and γ_L surface free energies[106]. The Fowkes[72, 106] and van Oss[71, 73, 106] formalism have been described in chapter 3.4.1. The γ_{SL} interfacial free energy is expressed by the surface free energy components of the solid and the liquid[71]. Using the van-Oss formalism and combining Equation 3.19, 3.20 and 4.22 yields;

$$(1+\cos\phi)\gamma_L = 2\sqrt{\gamma_L^{LW}\gamma_S^{LW}} + 2\sqrt{\gamma_L^+\gamma_S^-} + 2\sqrt{\gamma_L^-\gamma_S^+} \qquad \textbf{4.27}$$

Equation 4.27 contains the three unknown surface energy components of the solid which may be obtained by measuring the contact angle of three different liquids with known surface energy components[71, 73, 106]. Usually a combination of one completely apolar liquid with two or more strongly bipolar liquids is used[71, 73, 106]. As apolar liquid, diiodomethane is a common choice since it has a very high surface tension due to the strong dispersive intermolecular interactions from the highly polarizable iodine atoms and subsequently poor wetting properties[71, 73]. As bipolar liquids, water, formamide and glycerol are common choices[71, 73].

4.7 Quartz Crystal Microbalance with Dissipation Monitoring

Quartz-crystal microbalance with dissipation monitoring (QCM-D) is a surface sensitive technique where adsorption and other surface events are measured on quartz crystals[107-109]. In addition to the estimation of adsorbed mass (resolution <10ng/cm^2), rheological data may be obtained (shear modulus and viscosity)[107, 109]. The technique utilizes the piezoelectric ability of quartz to mechanically deform in an electric field. Hence, if an AC voltage is applied, the crystal will oscillate with a characteristic frequency. If a small mass is adsorbed on the crystal, the frequency will decrease. There is a linear relationship between the frequency change and the mass change given by the *Sauerbrey equation*[110] (Equation 4.28), provided that the adsorbed mass is much smaller than the mass of the crystal and that the corresponding film is rigid and elastic. Here, $\Delta\Gamma$ is the adsorbed mass per unit area, Δf^n is the frequency shift for a given harmonic n (=1, 3, 5, …)and C is the mass sensitivity constant (17.7 ng/cm^2/Hz for a quartz crystal with f^1=5 Hz).

$$\Delta\Gamma = \frac{\Delta f^n C}{n} \qquad 4.28$$

For viscoelastic films, e.g. a polymer film swelled by water (see Scheme 4.7), the Sauerbrey equation does not hold. The lower the harmonics the higher the corresponding calculated mass which is no longer a linear function with respect to frequency. Regarding solvent swelled films, the associated solvent molecules will couple with the oscillation and will also contribute to the sensed mass[107]. Moreover, in a viscoelastic film, some mechanical energy from the oscillation is *dissipated* to the system due to the viscous properties of the film[107, 109]. Therefore, the mass is underestimated if the Sauerbrey equation is used[107, 109].

However, this dissipation D may be obtained by applying an electrical pulse to the crystal and subsequently measure the attenuation (given by the decay time τ) of the oscillation amplitude A[109]. The dissipation is defined as the ratio of the energy dissipated to the system E_D and the stored energy E_S during one oscillation (Equation 4.29)[107, 108].

$$A \propto \exp(-t/\tau)$$
$$D = \frac{1}{\pi f \tau} = \frac{E_D}{2\pi E_S} \qquad 4.29$$

Scheme 4.7. Representation of a gold covered quartz crystal and specific surface events starting from a bare gold surface. The example illustrates the results from **Paper V** where a polymer is adsorbed and subsequently swelled in water.

The first arrow indicates the addition of a rigid film where only f decreases and the Sauerbrey equation may be used. The second arrow indicate the adsorption of collapsed polymer film where f decreases and there is a small increase in D. The third arrow indicates swelling of the polymer by water where f is further decrease and D is greatly increased.

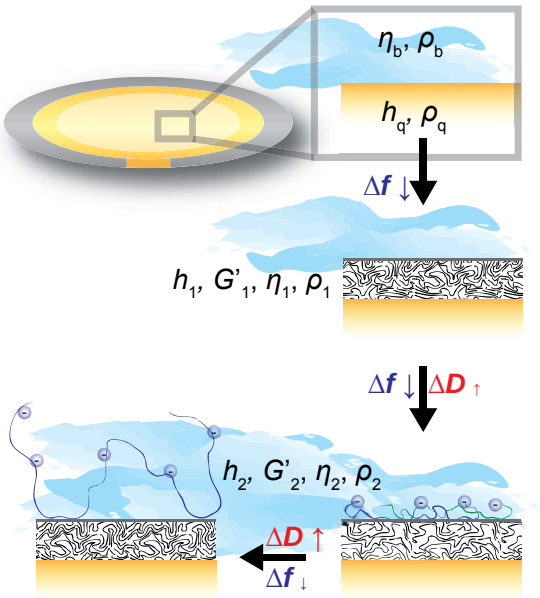

The adsorbed mass and the rheological parameters; G' (shear storage modulus) and $G''=2\pi f\eta$ (shear loss modulus, where η is the viscosity) may be calculated by applying viscoelastic models to the adsorbed film. Usually the *Maxwell* (viscoelastic fluid) or *Voigt element* (viscoelastic solid) is used (see Scheme 4.8)[109]. The latter element is often the most relevant model with respect to adsorbed surfactants and polymers[107, 109].

The final frequency and dissipation shifts will depend on the shear viscosity η_i, shear storage modulus G''_i, density ρ_i, penetration depth of the acoustic wave δ_i and thickness h_i of the quartz disc (i=q), the adsorbed film/films (i=1,2..) and the bulk (i=b) (see Equation 4.30 and 4.31 corresponding to the Voigt model). Normally, the bulk and quartz crystal parameters are known and the film density may be approximated. The remaining parameters are fitted with respect to the chosen model from two or more harmonics of f and D. Regarding rheological properties, it should be noted that traditional rheometry operates at 0.01 Hz< f < 100 Hz whereas the QCM-D operates at >5 MHz. This has a significant impact on the obtained rheological parameters which are frequency dependent in a viscoelastic material.

Scheme 4.8. The Voight (left) and Maxwell (right) viscoelastic elements.

The elements are constructed by a Hookean spring (index S) with elastic modulus E and a dashpot (index D) with viscosity η. Regarding the Voigt element, the deformation γ induced by an applied stress σ will be completely restored (stress relaxation). In contrast, the Maxwell element will be permanently deformed by an applied stress. The corresponding complex moduli G^*, with the storage moduli G' and loss moduli G'', are expressed below.

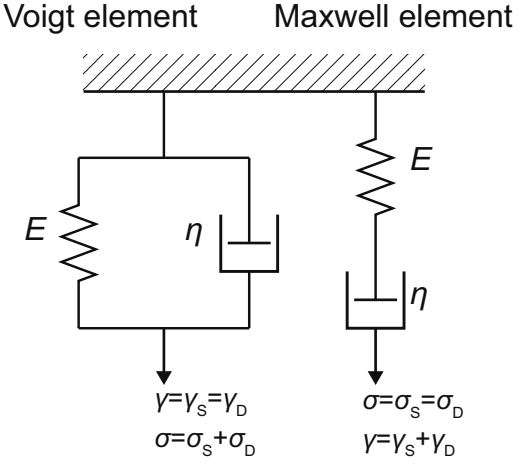

$$G^* = \underbrace{E}_{G'} + \underbrace{i\eta\omega}_{G''}$$

$$G^* = \underbrace{\frac{E\eta^2\omega^2}{\eta^2\omega^2 + E^2}}_{G'} + \underbrace{\frac{iE^2\eta\omega}{\eta^2\omega^2 + E^2}}_{G''}$$

$$\Delta f^n \approx \frac{1}{2\pi\rho_q h_q}\left\{\frac{\eta_b}{\delta_b} + \sum_{i=1,2}\left[h_i\rho_i 2\pi f^n - 2h_i\left(\frac{\eta_b}{\delta_b}\right)^2 \frac{\eta_i\left(2\pi f^n\right)^2}{G_i'^2 + \left(\eta_i 2\pi f^n\right)^2}\right]\right\} \qquad \textbf{4.30}$$

$$\Delta D^n \approx \frac{1}{2\pi f^n \rho_q h_q}\left\{\frac{\eta_b}{\delta_b} + \sum_{i=1,2}\left[2h_i\left(\frac{\eta_b}{\delta_b}\right)^2 \frac{\eta_i 2\pi f^n}{G_i'^2 + \left(\eta_i 2\pi f^n\right)^2}\right]\right\} \qquad \textbf{4.31}$$

CHAPTER 5

Results and Discussion

The results obtained during the progression of this doctoral project have been divided into an *imidazole coordination chemistry* related part and a *charged microcapsule* related part. The imidazole coordination chemistry part has been slightly condensed in this thesis and the interested reader is referred to the corresponding licentiate thesis[111].

5.1 Imidazole Coordination Chemistry

The summary of the results related to imidazole coordination chemistry is crudely divided into three main subsections. The first subsection is purely focused on the synthesis of polymers containing imidazole moieties. Some of these polymers have been coordinated by Cu^{2+} and Zn^{2+} and the effect of this coordination is discussed in the second subsection. These polymers have been saturated with metal ions in contrast to the "monomeric" complexes discussed in the third subsection. Here, the significance of substitution position on imidazole has been evaluated.

5.1.1 Functionalization of polymers with imidazole

A number of polymers containing imidazole groups were synthesized. An epoxide route was used in order to functionalize ethyl(hydoxyethyl)cellulose (EHEC) with imidazole groups (see Scheme 5.1). The modified polymer and its interaction with Cu^{2+} were evaluated in **Paper IV**. The polymers containing the *maleimide* moiety were synthesized with the aim of establishing synthetic routes, utilizing histidine as a "natural" imidazole source, to incorporate imidazole groups substituted at position 4 (**Paper III**). The synthetic routes comprised both grafting onto by maleimide bond formation on a maleic anhydride polymer (see Scheme 5.1) and conventional radical polymerization (see Scheme 5.2).

Both routes were successful but the maleimide route facilitates both grafting onto as well as radical polymerization and is conveniently carried out in one step without the necessity of protective groups.

Scheme 5.1. Imidazole functionalization of polymers and monomers.

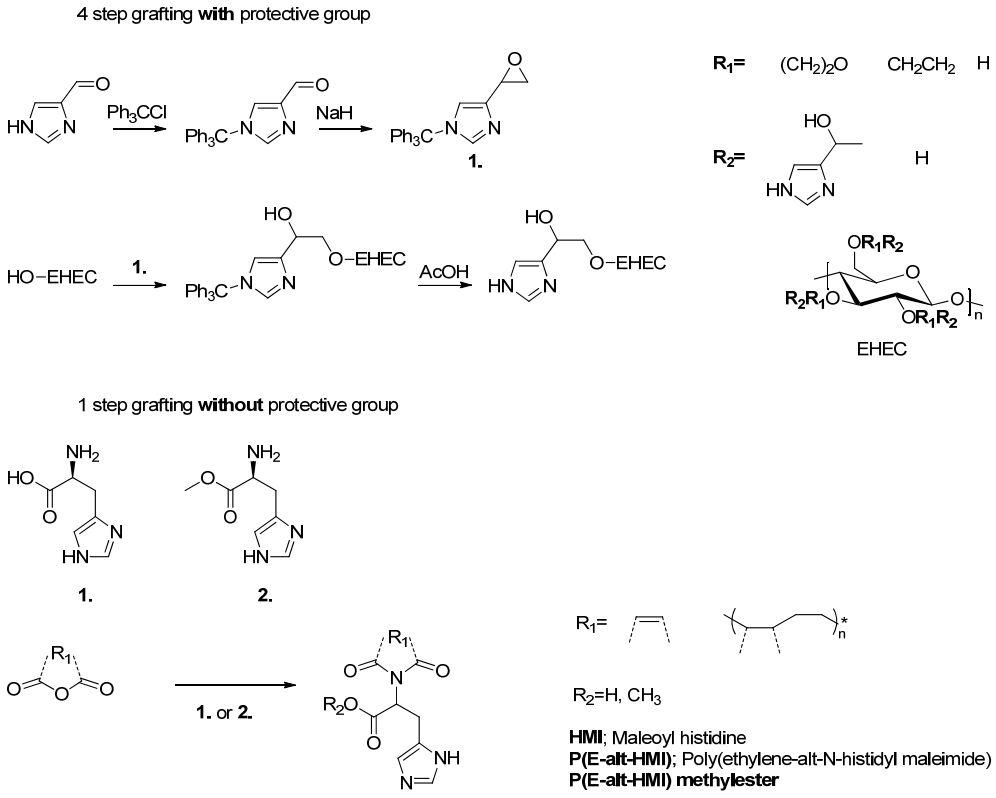

Copolymers of MMA (methylmethacrylate) and 1-VIm (1-vinylimidazole) (poly(1-VIm-*co*-MMA) abbreviated *PVM*) were polymerized with the rationale of functionalizing PMMA which is the most common microcapsule shell material used in this project (**Paper I**). The PVM polymers were furthermore coordinated by Cu and Zn in order to evaluate the coordination chemistry of the material.

Scheme 5.2. AIBN initiated radical polymerization.

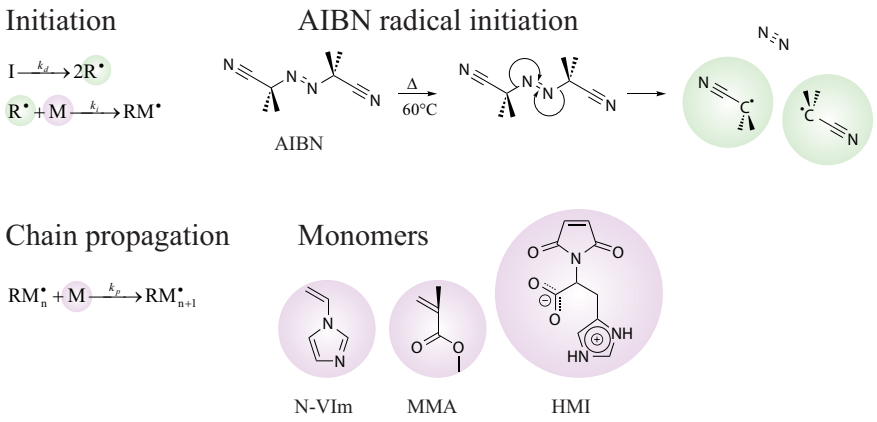

5.1.2 Properties of coordinated polymers

Bond strength and selectivity

Regarding the PVM copolymers (**Paper I**), the polymer contains two possible metal-coordinating ligands; the imidazole and the ester group. However, the metal ions exclusively coordinate the imidazole ligand of the polymer. This is evident since only imidazole bands in FTIR are altered upon coordination (see Figure 5.1). Regarding copper complexes[m], EPR affirms this fact since complex synthesis of PMMA results in no signal (see Figure 5.2c). Furthermore, the environment appears to be square planar (or tetragonal) due to the resemblance between of the EPR spectra of square planar $[Cu(Me(1)\text{-}Im)_4]^{2+}$ and PVM-4-Cu^{2+}. It should be noted that the EPR parameters and spectrum of PVM-4-Cu^{2+} are especially similar to imidazole methylated at position 1 (Me(1)-Im) coordinated by Cu^{2+} (see Table A.1).

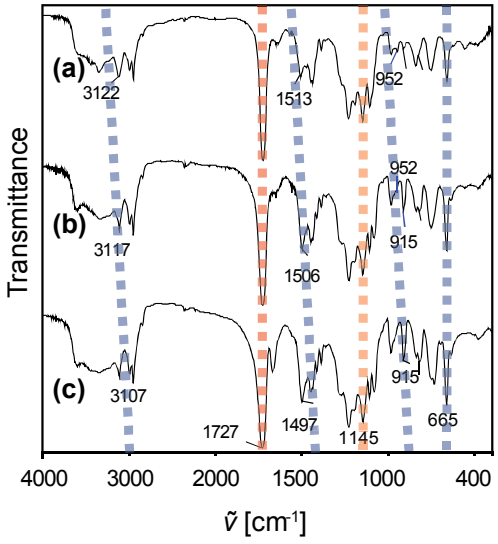

Figure 5.1. FTIR spectra of PVM-44 (c) coordinated by Cu^{2+} (a) or Zn^{2+} (b).

As a result of complexation, some FTIR bands are shifted. In particular, the in-plane skeletal vibrations of the imidazole ring. However, the carbonyl stretch of the MMA methylester remains unaltered.

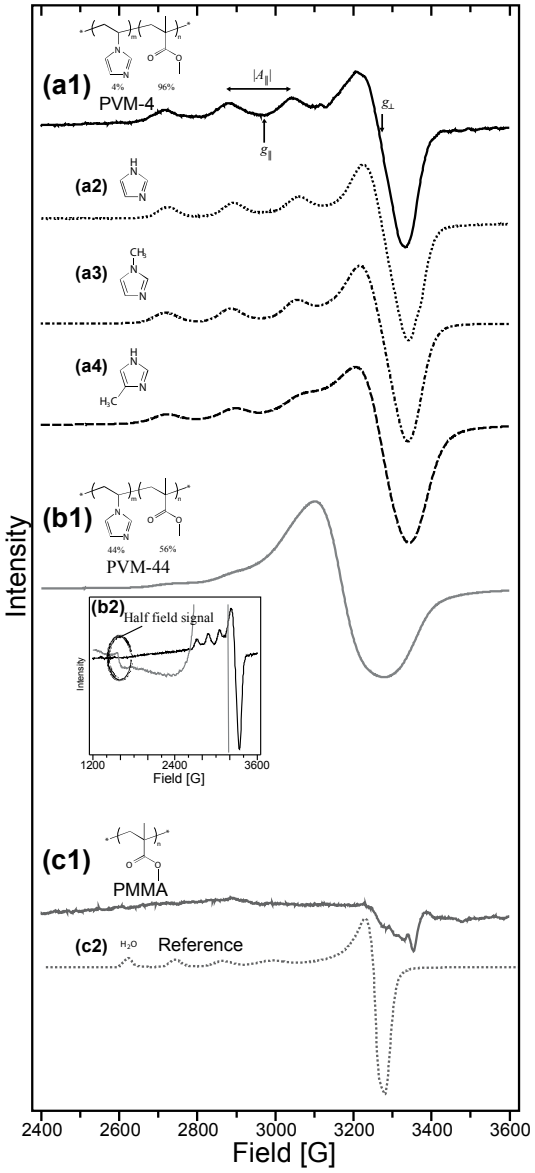

Figure 5.2. Cu^{2+} EPR spectra in MeCN of; (a1) PVM-4, (a2) Im, a3) Me(1)-Im, (a4) Me(4)-Im, (b1) PVM-44, (b2) PVM-44 half field signal, (c1) PMMA, (c2) H_2O.

The paramagnetic centers, i.e. the Cu(II) ions, of PVM-44 are closer together compared to PVM-4 which is reasonable due to the larger fraction of imidazole ligands per polymer chain. To be more precise, the coordination complexes are separated by less than 20 Å (see Figure 6.6) which is indicated by the EPR half field signal (Figure 6.6).

[m] Zn^{2+} is diamagnetic and hence EPR silent. All EPR results concern only Cu^{2+} complexes.

Coordinate crosslinks

The coordinate bonds between the imidazole ligand and the metal ions generate crosslinks between the polymer chains. The crosslinks cause the glass transition temperature, T_g, to increase since the chain segments in proximity of a crosslink are stiffened due to the reduced rotational freedom (see Figure 5.3)[92]. The net increase in T_g is a function of the strength as well as the number of crosslinks and is discussed in **Paper I**. Furthermore, the cross-links facilitate bilayer formation with Cu^{2+} ions binding two EHEC-Im layers together (**Paper IV**).

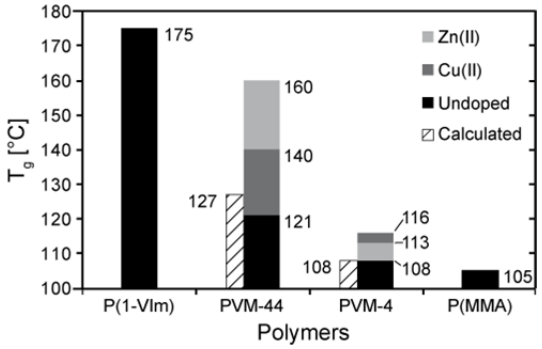

Figure 5.3. Glass transition of polymers and polymer complexes.

The crosslinks introduced in the polymers due to the coordinate bonds to metal ions renders the resulting complex insoluble in conventional solvents (**Paper I**), especially for Cu^{2+} complexes. However, it is possible to dissolve the polymers in strongly coordinating solvents.

This result, with respect to the PVM copolymers, has unfortunately huge implications on the microcapsule synthesis. The solvent evaporation technique (see chapter 3.4.2) relies on a delicate correlation of interfacial tensions between the respective solvents. In contrast to the solvents constituting the oil phase, coordinating solvents are typically rather polar and non-volatile. These properties of the coordinating solvents greatly limit their use as solvents for the polymer complex during microcapsule synthesis.

5.1.3 The effect of the position of a methyl substituent

When inspecting the polymers discussed in the earlier subchapters, it may be observed that the imidazole ligand is attached to the polymer backbone at either position 1 or 4 and this holds for in principle any arbitrary imidazole-containing polymer. Moreover, regarding imidazole from biological sources, such as histidine, the imidazole ring is always substituted at position 4. This is in contrast to synthetic imidazole-containing polymers were the imidazole ring is usually attached to the backbone at position 1, i.e. *via* the pyrolle nitrogen. Subsequently, it may be speculated why Nature has chosen this particular position for substituent attachment. To investigate this, the methylated imidazole model compounds Me(1)-Im and Me(4)-Im (see Scheme 5.3) were analysed in **Paper II** with respect to similarities and differences in coordination strength, coordination geometry, covalency etc.

Scheme 5.3. Molecular structure of the methylated imidazoles.

Ligand	R_1	R_2
Im	H	H
Me(1)-Im	CH_3	H
Me(4)-Im	H	CH_3

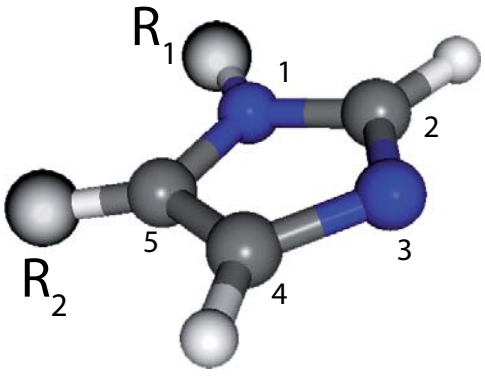

Similarities

There are some similarities in coordination chemistry between Me(1)-Im and Me(4)-Im. For instance, the steric hindrance of the methyl group upon coordination is the same for both methylated imidazoles (see Scheme 5.3 and Scheme 5.4) since Me(4)-Im actually coordinates as Me(5)-Im[112]. As a consequence, the coordination symmetries for the methylated imidazole ligands are very similar, both for Cu^{2+} and Zn^{2+} complexes in contrast to unsubstituted imidazole. (see Scheme 5.4).

Scheme 5.4. Coordination symmetries. (a) Tetrahedral $[Zn(Me\text{-}Im)_2Cl_2]$, (b) Octahedral $[ZnIm_6]^{2+}$ and (c) Tetragonal $[CuIm_4Cl_2]$ and $[Cu(Me\text{-}Im)_4Cl_2]$.
The coordination symmetry for Cu^{2+} complexes is tetragonal D_{4h} symmetry for the methylated imidazoles, equivalent to unsubstituted imidazole. The imidazole ligands are almost perpendicular to the coordination axis and the chlorides are weakly bound axially (see Figure 5.4)[112-114]. However, regarding Zn^{2+} complexes, unsubstituted imidazole forms octahedral complexes[113] $[Zn(Im)_6]^{2+}$, whereas the methylated imidazoles form tetrahedral C_{2v} complexes[114, 115] $[Zn(Me\text{-}Im)_2Cl_2]$ despite the large excess of imidazole ligand. It is not clear if this discrepancy is due to steric or electronic factors.

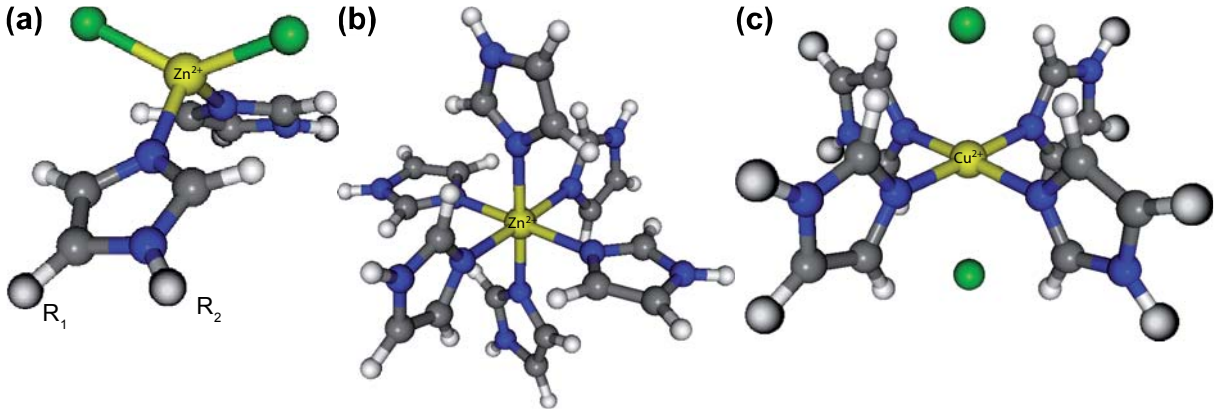

All imidazole Cu complexes display a substantial amount of covalence which is revealed in a variety of ways using far-FTIR, EPR and *ab initio* calculations[n]. The σ-interaction of all complexes obtain values of $\alpha^2 \approx [0.82, 0.87]$ (EPR; calculated using Equation 4.6) or $\alpha^2 = 0.71$ (*ab initio*). An even better indication of the high degree of covalence is the π-interaction coefficient (EPR; $\beta^2 \approx [0.65, 0.69]$, *ab initio*; $\beta^2 \approx [0.51, 0.60]$)[90]. The presence of fine structure in Figure 5.4 is also a direct indication of covalence as explained in chapter 4.1.2.

[n] The importance of covalence in the coordinate bond is revealed since the order of bond strength or bond distance (Me(4)-Im>Im ≥Me(1)-Im)) does not follow the order of pK_a values (Me(4)-Im>Me(1)-Im≥Im)

Differences

An important difference between Me(1)- and Me(4)-Im is the reduced "degrees of freedom" for Me(1)-Im. Me(4)-Im, equivalent to Im, contains two potential sites for coordination or protonation. Consequently, Me(4)-Im and Im may, as a function of ligand metal ratio and pH, form coordination polymers which is restricted for Me(1)-Im.

Regarding the coordinate interaction, the Me-C4 bond appears to be slightly more polarizable than the Me-N1 bond. Since the methyl substituent is an electron donating group (see Scheme 5.5), the Me-C4 bond facilitates the electron transfer to the imidazole ring more efficiently than the Me-N1 bond. Consequently, Me(4)-Im is a stronger base than both Me(1)-Im and Im (see Table A.1). However, the stability constant is lower for the corresponding Me(4)-Im complex compared to Me(1)-Im and Im which suggest a significant π-acceptor interaction in addition to the σ-donor interaction in the coordinate complex.

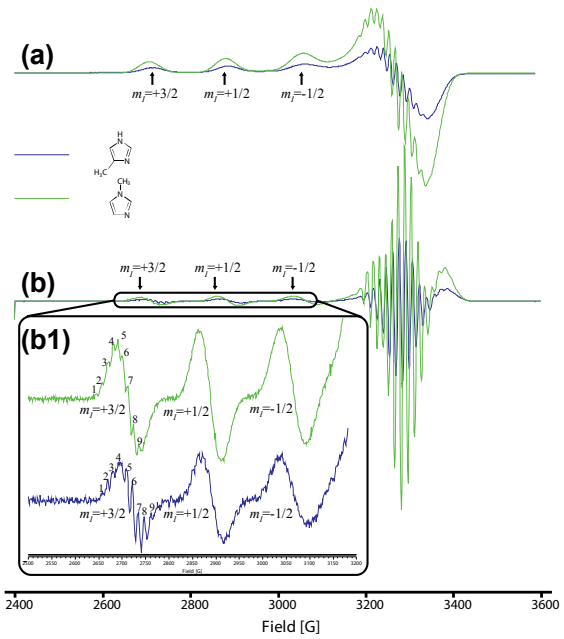

Figure 5.4. Me-Im in water/glycerol. (a) EPR signal of Me(1)-Im (green) and Me(4)-Im (blue). (b) Derivative of the EPR signal with inset (b1) displaying the fine structure at m_I=+3/2.

The fine structure indicate four equivalent ligands according to Equation 4.4. However, some signals appear to be doublets which may be explained by the Cu^{2+} isotope mixture[32, 33].

Yet, if the polymeric imidazole ligands used in this work are compared, that is 1-VIm and histidine, the position of the substituent in the imidazole ring is not the most important factor. The chemical nature of the substituent, more precisely its electron withdrawing or electron donating abilities, is more important with respect to the coordinate interaction.

Scheme 5.5. The effect of the substituent with respect to electron donating/accepting capacity on the coordinate interaction.

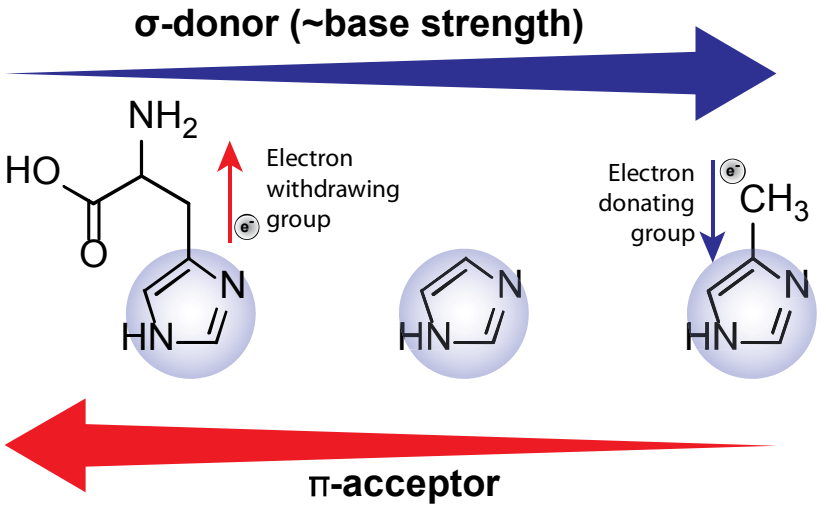

5.2 Charged and Surface Modified Microcapsules

In the following subchapters, the evolution from the synthesis of charged microcapsules (**Paper V-VII**) and their subsequent surface-modification (**Paper VIII**) to release measurements (**Paper IX**) is summarized. All molecules relevant to this work are summarized and categorized in Chart 5.1.

5.2.1 Microencapsulation using ionic dispersants

Three types of ionic dispersants were used in order to charge the microcapsules; a weak polyelectrolyte (PMAA), a small set of amphiphilic block copolymers (PMMA-*b*-P(M)ANa) and a hydrophobic surfactant (TC4) in combination with a polycation (PDADMAC) (see Chart 5.1). All microcapsule systems, except the PMAA based one, are characterized by a high ζ-potential which does not change with time or after washing steps. The PMAA based[13] and the block copolymer based microcapsules have a core-shell morphology (see Figure 5.6). In contrast, the PDADMAC-TC4 based microcapsules display a multicore morphology (see Figure 5.6). The details of each dispersant system are summarized below.

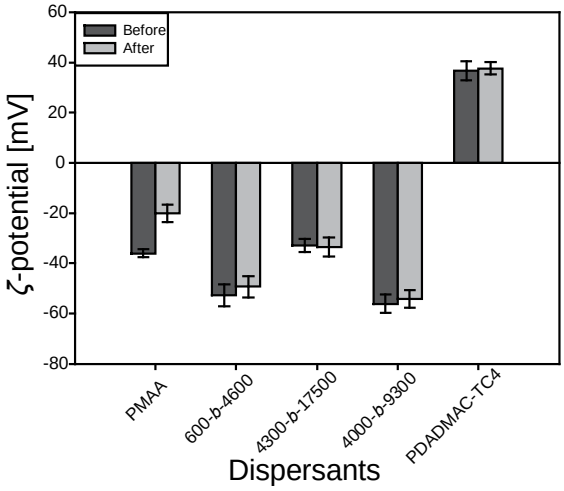

Figure 5.5. ζ-potential of microcapsules based on (from left to right) PMAA, 600-*b*-4600, 4300-*b*-17500, 4000-*b*-9300 and PDADMAC-TC4 before (dark grey) and after (bright grey) washing with centrifugation at neutral pH.

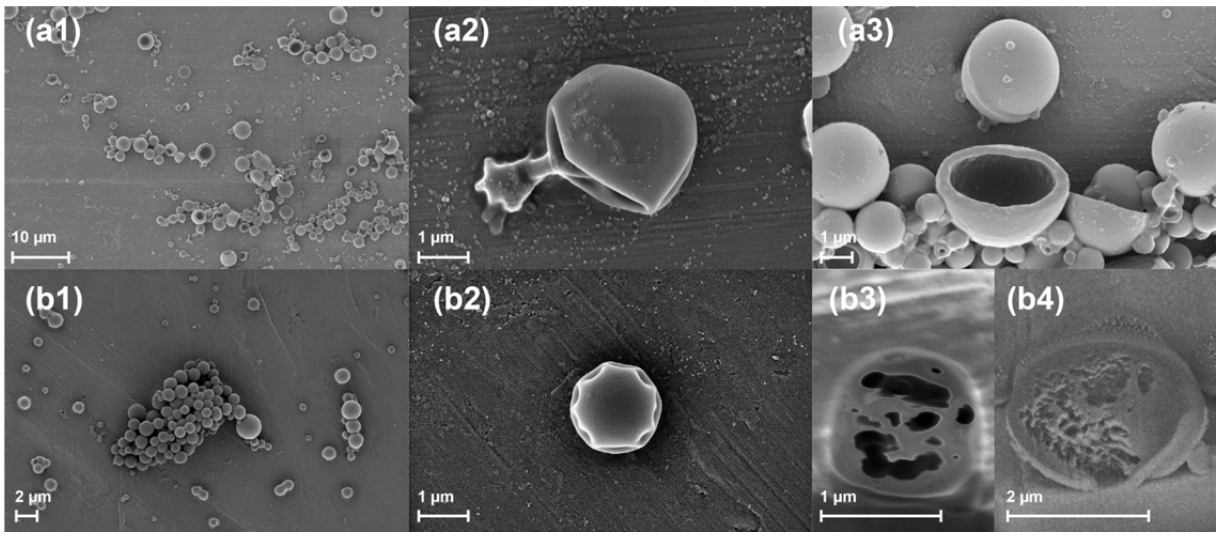

Figure 5.6. SEM images of microcapsules based on (a) 600-*b*-4600 and (b) PDADMAC-TC4 . (a1) and (b1) are overview images of the capsules. The capsules in (a2) and (b2) have been subjected to a gentle heat treatment at 3 kV in order to collapse the PMMA shell. (a3) displays the core-shell morphology of the 600-b-4600 based microcapsules. (b3) and (b4) display cross-sections of 2 weeks old capsules and fresh capsules, respectively cut with a focused ion beam.

Chart 5.1. Summary of all dispersants, lipids, polyelectrolytes and release-related substances used in this work.

Dispersants

Weak polyacid

PMAA

Poly[methacrylic acid]

M_n=100 000 g/mol

Amphiphilic block copolymers

600-*b*-4600

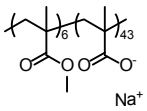

Poly[methyl methacrylate(600)-*block*-sodium methacrylate(4600)]

4000-*b*-9300

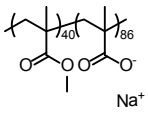

Poly[methyl methacrylate(4000)-*block*-sodium methacrylate(9300)]

4300-*b*-17500

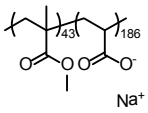

Poly[methyl methacrylate(4300)-*block*-sodium acrylate(17500)]

Lipids

Microcapsule modification

DSPA

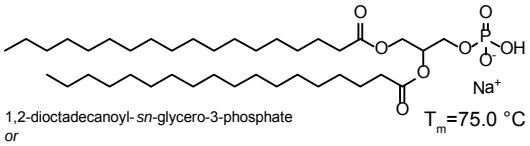

1,2-dioctadecanoyl-*sn*-glycero-3-phosphate
or
1,2-distearoyl-*sn*-glycero-3-phosphate

T_m=75.0 °C

DMDOAC

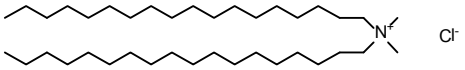

N,*N*-dimethyl-*N*,*N*-dioctadecylammonium chloride
or
N,*N*-dimethyl-*N*,*N*-di(hydrogenated tallow)ammonium chloride

T_m=34.4 °C

QCM-D measurements

DOPA

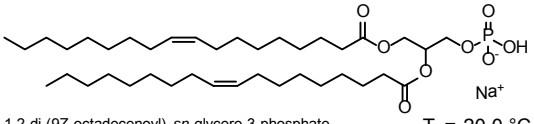

1,2-di-(9Z-octadecenoyl)-*sn*-glycero-3-phosphate
or
1,2-dioleoyl-*sn*-glycero-3-phosphate

T_m=-20.0 °C

DMDOEAC

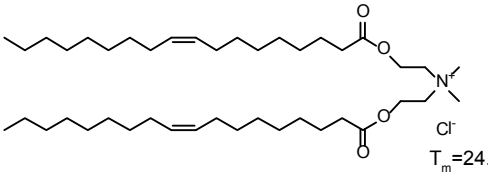

N,*N*-dimethyl-*N*,*N*-bis((9Z-octadecenoyloxy)ethyl)ammonium chloride
or
N,*N*-dimethyl-*N*,*N*-bis((oleoyloxy)ethyl)ammonium chloride
or
N,*N*-dimethyl-*N*,*N*-di(soft tallow)diethylesterammonium chloride

T_m=24.8 °C

Oil soluble anionic surfactant and water soluble polycation

Polyelectrolytes

TC4

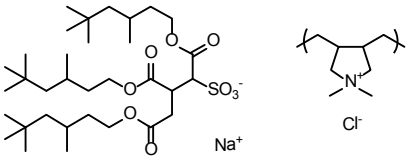

Sodium 1,5-dioxo-1,5-bis(3,5,5-trimethylhexylocy)
-3-((3,5,5 trimethylhexyloxy)carbonyl)pentane-2-sulfonate

PDADMAC

Poly[diallyldimethylammonium chloride]

M_n=350 000 g/mol

PMANa

Poly[sodium methacrylate]

M_n=15 000 g/mol

Substances used in release measurements

Disperse red 13

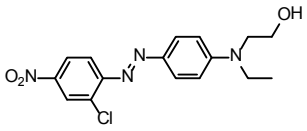

λ_{max}=503 nm

2-(4-(2-Chloro-4-nitrophenylazo)- *N*-ethylphenylamino)ethanol

Brij 35

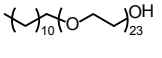

CMC=10^{-4} M

Polyoxyethylene(23) laurylether

Weak polyelectrolyte

The PMAA based microcapsules are only stable with excess dispersant, i.e. PMAA. Under these conditions, the suspension is acidic and the microcapsules are virtually uncharged. However, since PMAA is a weak polyacid, the surface charge density of the microcapsules may be increased by simple alkaline titration (see Scheme 5.6 and Figure 5.5) and limited colloidal stability without excess dispersant may be obtained. The alkaline treatment will increase the degree of dissociation of the PMAA chain (Equation 3.13) but also the water solubility of PMAA. Subsequently, the colloidal stability gained by the electrostatic stabilization is counteracted by desorption which finally leads to irreversible aggregation (**Paper V** and **VII**).

Scheme 5.6. Morphology of the PMAA based microcapsule and structure of the adsorbed PMAA layer at acidic (left) and neutral/alkaline conditions.

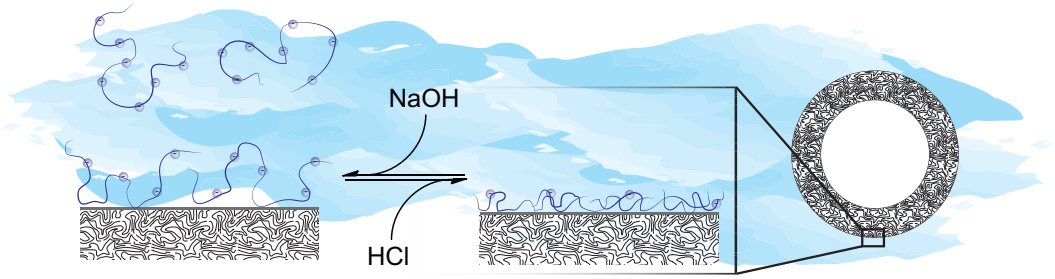

Amphiphilic block copolymers

All block copolymer based microcapsules (see Chart 5.1) are characterized by a high surface charge density which is stable over time and after washing. Furthermore, the anchor block is *embedded* in the underlying PMMA surface (see Scheme 5.7) rather than simply *physisorbed* as revealed from QCM-D measurements (**Paper VI**) and this is a requirement for the good colloidal stability. The block copolymers are most likely forming a polyelectrolyte brush layer (see chapter 3.3.3 and 3.5.2) which stabilizes the microcapsule suspension with electrostatic and steric repulsion.

Scheme 5.7. Morphology of the block copolymer based capsule and structure of the embedded block copolymers on the microcapsule surfaces.

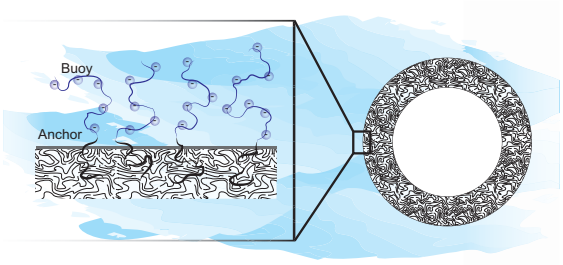

The size distribution and surface charge density of the microcapsule depends on a variety of block copolymer characteristics such as block lengths and block ratio, CMC, diffusion constant, surface activity etc. (**Paper VII**). Nonetheless, a general property of the block copolymers is the ability to efficiently stabilize the PMMA-water interface without affecting the oil-water interface to a large extent. This property makes the block copolymers ideal as dispersants for the microencapsulation process.

Oil-soluble anionic surfactant and water-soluble polycation

The PDADMAC-TC4 based microcapsules are very different from the previously discussed microcapsule systems due to the presence of the surfactant TC4 in the oil phase. It is clear that the anionic surfactant is present in the PMMA shell since the corresponding microcapsules obtain a very high positive ζ-potential (see Figure 5.5) from the promoted PDADMAC adsorption. However, a fraction of TC4 is most likely partitioned into the oil-phase since the morphology of the PDADMAC-TC4 based microcapsules appears to be multicore (see Figure 5.6 and Scheme 5.8) rather than core-shell. The presence of TC4 in the oil phase will result in a large reduction of the oil-water interfacial tension (**Paper VII**). This would explain the partial phase separation observed after the microencapsulation.

The PDADMAC-TC4 microcapsules have a good long-term colloidal stability but aggregate at high salt concentrations. This is a result of the conformation of the adsorbed PDADMAC chain. As discussed in chapter 3.3.4, a strong polyelectrolyte will adsorb in a flat manner on an oppositely charged surface at low salt concentrations. This implies that in contrast to the block copolymer based system, the PDADMAC-TC4 based microcapsules will not be stabilized by steric repulsion.

Scheme 5.8. Morphology of the PDADMAC-TC4 based microcapsules and the structure of the adsorbed PDADMAC layer promoted by the presence of TC4 in the shell.

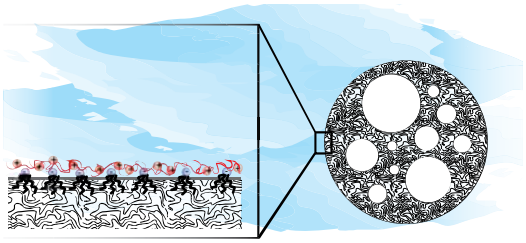

5.2.2 Surface modification

The charged microcapsules described above were surface modified with PEMs and lipid bilayers (**Paper XIII**). The most comprehensive analysis of the PEM and lipid bilayer assembly was performed on the 600-*b*-4600 based (see Chart 5.1) and PDADMAC-TC4 based microcapsule system. Regarding the lipid bilayer formation, the surface of the microcapsule was pre-treated with a few polyelectrolyte layers (see Scheme 5.9). The pre-treatment was intended to reduce the presumed surface roughness of the block copolymer brush layer.

Scheme 5.9. Schematic representation of a microcapsule modified with a PEM and a lipid bilayer.

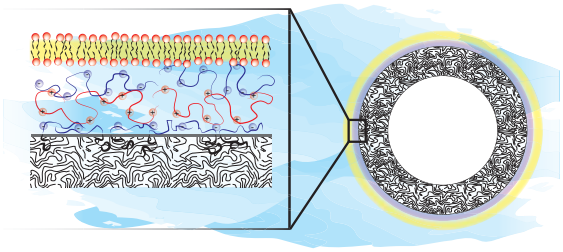

Polyelectrolyte multilayer

The high surface charge density of the microcapsules facilitates the LbL adsorption of the polyelectrolyte pair PDADMAC/PMANa (see Chart 5.1) as followed by the alternating ζ-potential (see Figure 5.7). The data in Figure 5.7 represents microcapsule suspensions (based on 600-*b*-4600 and PDADMAC-TC4) which have been washed by centrifugation in order to remove excess polyelectrolyte. Since the ζ-potential is not altered by the washing step, each adsorbed layer appears to be stable.

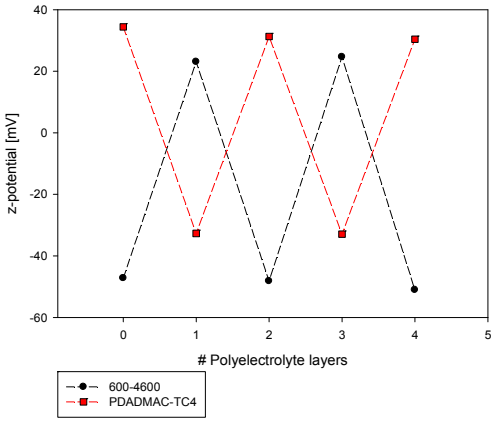

Figure 5.7. ζ-potential as a function of successive adsorption of PDADMAC and PMANa on 600-*b*-4600 based (black, ●) and PDADMAC-TC4 based (red, ■) microcapsules.

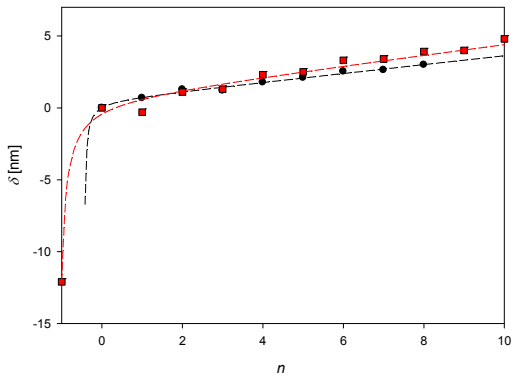

Figure 5.8. LbL adsorption of PDADMAC and PMANa on a PDADMAC-TC4 based (red, ■) and a 600-*b*-4600 based (black, ●) PMMA surface. The PDADMAC-TC4 plot has been normalized so that for the first adsorbed PDADMAC layer n=0 and δ=0. δ is the thickness of the adsorbed film and n is the number of layers that build up the film.

The growth of the PEMs, appears to be linear (Figure 5.8), as measured with QCM-D on TC4 or 600-*b*-4600 functionalized PMMA model surfaces. This growth behaviour is expected for highly charged polyelectrolytes[54, 60] (chapter 3.3.4). Moreover, each successive polyelectrolyte bilayer is very thin, which is most likely a result of the low molecular weight of PMANa[116] (see Chart 5.1).

Lipid bilayer

Lipid bilayers are successfully assembled on microcapsule surfaces. In Figure 5.9, microcapsules based on 600-*b*-4600 modified with one PDADMAC/PMANa bilayer have been treated with positively charged DMDOAC liposomes. After liposome adsorption, the ζ-potential of the microcapsule is inverted to almost the equivalent value corresponding to the DMDOAC liposome itself. However, the adsorbed lipid bilayer is not as stable as the adsorbed polyelectrolyte layer since washing using centrifugation results in a considerable reduction of the ζ-potential. However, the lipid bilayer may be preserved by adopting the gentler ultrafiltration method.

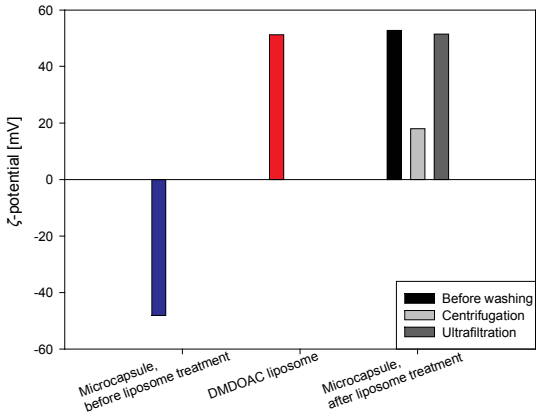

Figure 5.9. ζ-potential of DMDOAC liposome treated microcapsules based on 600-*b*-4600 modified with one PDADMAC/PMANa polyelectrolyte bilayer before liposome adsorption (blue), after liposome adsorption (black) and after washing using centrifugation or ultrafiltration. As reference, the ζ-potential of the DMDOAC liposome is shown (red).

The ζ-potential results presented above reveal that liposomes adsorb on microcapsule but do not distinguish between the adsorption of lipid bilayers or intact vesicles. Therefore, QCM-D measurements were undertaken in order to evaluate the adsorbed lipid structure and adsorption kinetics (see Figure 5.10). Note that the liposome adsorption experiments are performed above the T_m of the lipid. Since the T_m of the lipids used for microcapsule modification (DMDOAC and DSPA) are very high, the model lipids DMDOEAC and DOPA (see Chart 5.1), with lower T_m, were used instead. Figure 5.10 displays liposome adsorption of anionic DOPA and cationic DMDOEAC on 600-b-4600 based PMMA surfaces modified with on PDADMAC layer and one PDADMAC/PMANa bilayer respectively. Both liposomes appear to form bilayers *via* a one-step process. It is reasonable to assume that the corresponding liposomes of DSPA and DMDOAC follow a similar behaviour.

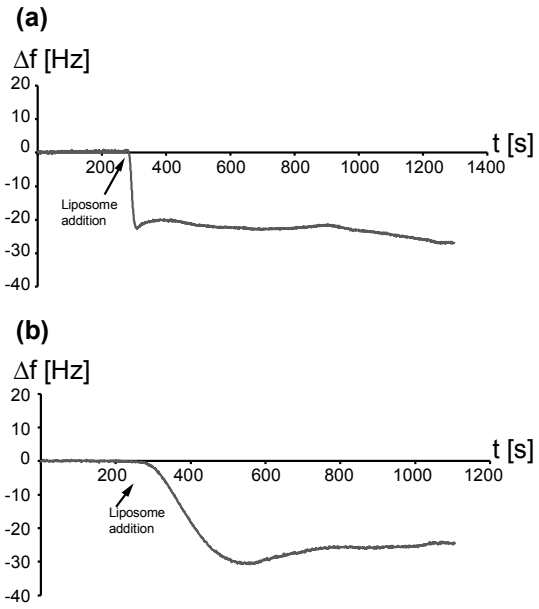

Figure 5.10. Liposome adsorption as indicated by the frequency shift (Δf) of third harmonic as a function of time (t) measured using QCM-D on 600-*b*-4600 modified PMMA model surfaces. **(a)** DOPA adsorption on PDADMAC treated surface. **(b)** DMDOEAC adsorption on a PDADMAC-PMANa bilayer treated surface.

5.2.3 Release measurements

In Figure 5.11, the release of the hydrophobic dye Disperse red 13 (see Chart 5.1) from *microsphere* suspensions in aqueous Brij 35 solution prepared with different dispersants is displayed (**Paper IX**). The surface properties of the microsphere are equivalent to the surface properties of the corresponding microcapsule. Since the release study aims at investigating the effect of dispersant and PEM assembly, the use of microspheres instead of microcapsules is motivated by the ease of handling.

A highly charge surface layer is indeed a good barrier against hydrophobic molecules. The release from microspheres prepared with the highly charged block copolymer 600-*b*-4600 is considerably lower than the release from microspheres prepared with the dispersants PMMA and PVA. A surface modification of the 600-*b*-4600 based microspheres with two PDADMAC/PMANa bilayers results in a further reduction of the release from 15 % to 4% after 600 h.

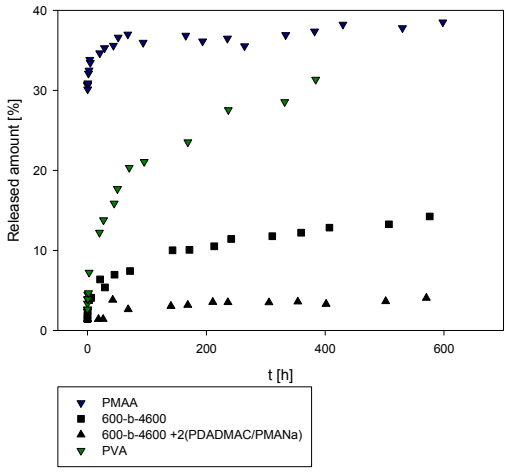

Figure 5.11. Release of the dye Disperse red 13 from microspheres based on PMAA (▼, green), PVA (▼, blue) and 600-*b*-4600 (■, black) and 600-*b*-4600 functionalized with two PDADMAC/PMANa bilayers (▲, black). The release is given as percent of theoretical yield of released dye.

Concluding Remarks

Imidazole Coordination Chemistry

Polymers may be functionalized by imidazole groups in a variety of ways. Simple copolymerization with 1-VIm, as well as grafting of histidine onto a polymer by maleimide bond formation or epoxide ring opening, has been used within this work.

The properties of a polymeric material containing imidazole ligands are strongly affected by the coordination by Cu^{2+} and Zn^{2+}. For instance, only strongly coordinating solvents can be used to dissolve the complex. This implies that microencapsulation of such a complex using the solvent evaporation technique will be problematic. However, it should still be possible to more crudely coordinate the polymer to metal ions by exposing already synthesized microcapsules to concentrated metal salt solutions.

Concerning the effect of ring substitution on the coordination chemistry of imidazole, the results indicate that the inductive effect of the group attached has a much larger effect than the position of the group. This result is not in line with our initial hypothesis. However, it opens opportunities to tailor the coordination chemistry by the chemical properties of the substituent.

Charged and Surface Modified Microcapsules

Highly charged microcapsules may be synthesized *via* the solvent evaporation method using ionic dispersants. Three types of ionic dispersants have been evaluated, a weak polyacid (PMAA), a small set of amphiphilic block copolymers of PMMA-*b*-PMANa type and a hydrophobic anionic surfactant in combination with a polycation (PDADMAC). The block copolymer based microcapsules are especially promising due to long-term colloidal stability provided by electrostatic and steric stabilization. The surfactant-polycation based microcapsules may also be interesting due to the multi-core morphology.

The high surface charge density of the microcapsule enables both the assembly of polyelectrolyte multilayers and lipid bilayer formation.

The polyelectrolyte multilayer is indeed an efficient barrier against hydrophobic molecules and the low permeability is clearly a result of the high charge density. The effect of the lipid bilayers on the release has, as of yet, not been investigated but has a large potential since the permeability may be altered by the lipid composition. A microcapsule consisting of an oil core, a hydrophobic polymer shell, a polyelectrolyte multilayer and a lipid bilayer is a complex release system with large degrees of freedom for tailoring the release behaviour.

Acknowledgement

Mistra, the foundation for strategic and environmental research is acknowledged for Financial Support.

I would like to express my gratitude to everyone at Applied Surface Chemistry:

My supervisor Magnus Nydén and my co-supervisor Krister Holmberg for giving me the opportunity to conduct research within the Marine Paint project as well as many fruitful discussion, enthusiasm, guidance and support.

My excellent master thesis student and project worker Ye Li is acknowledged for all the hard microcapsule work. Without your aid, this thesis would have been considerably shorter…

Adele Khavari, Adriana Trinchero, Ali-Reza Movahedi, Chlor, Andreas Sundblom, Daniel Cederkrantz, Maria Claesson, Björn Elgh, Hanna Gustavsson, my old room-mate Erik Nilsson and my new one Emma Westas, Jonas Nordström, Moheb Nayeri, Ralph, Sören Svan, Ma Yi and Åsa Östlund, are especially acknowledged for garnishing the atmosphere in the coffee room, lunches, conferences, courses and leisure time. The "Innebandy crew" for all rough and vicious mornings at kårhuset.

My co-authors Lars Öhrström, Örjan Hansson, Jesper Hedin, Dan Isaksson, Anders Mårtensson, Anne Wendel, Maria Claesson and Christoffer Abrahamsson are acknowledged for support, advices and many fruitful discussions. Örjan Hansson is greatly acknowledged for all support related to the EPR measurements

Other important people at the department for Chemical and Biological Engineering that need to be acknowledged are Ann Jakobsson, Kurt Löfgren, Mats Andersson, Johan Bergenholtz and Staffan Wall.

I would like to thank all the fine people in the Marine Paint project, especially Hans Blanck, Åsa Arrhenius, Anna Lennquist and Mattias Berglin.

Finally I would like to thank my family and especially my wonderful wife Verena Trojer who has been an unyielding support throughout this entire period.

References

1. *Marine Paint Annual Report 2008*; Gothenburg, 2009.
2. Almeida, E.; Diamantino, T. C.; De Sousa, O. *Prog. Org. Coat.* **2007,** 59, (1), 2-20.
3. Chambers, L. D.; Stokes, K. R.; Walsh, F. C.; Wood, R. J. K. *Surf. Coat. Technol.* **2006,** 201, (6), 3642-3652.
4. Omae, I. *Chem. Rev. (Washington, DC, U. S.)* **2003,** 103, (9), 3431-3448.
5. International Maritime Organization, International Convention on the Control of Harmful Anti-fouling Systems on Ships, 2011, [retrieved: 2011:11:07], http://www.imo.org
6. Omae, I. *Kagaku Kogyo* **2003,** 54, (8), 646-652.
7. Finch, C. A.; Bodmeier, R., Microencapsulation. In *Ullmann's Encyclopedia of Industrial Chemistry*, 6th ed.; Bohnet, M., Ed. Wiley-VCH: Weinheim, 2002.
8. Ghosh, S. K., Functional Coatings and Microencapsulation: A General Perspective. In *Functional Coatings*, 1st ed.; Ghosh, S. K., Ed. Wiley-VCH: Weinheim, 2006.
9. Thies, C., Microencapsulation. In *Kirk-Othmer Encyclopedia of Chemical Technology*, Kroschwitz, J. I., Ed. Wiley: N.Y., 2005.
10. Atkin, R.; Davies, P.; Hardy, J.; Vincent, B. *Macromolecules* **2004,** 37, (21), 7979-7985.
11. Dowding Peter, J.; Atkin, R.; Vincent, B.; Bouillot, P. *Langmuir* **2004,** 20, (26), 11374-9.
12. Dowding, P. J.; Atkin, R.; Vincent, B.; Bouillot, P. *Langmuir* **2005,** 21, (12), 5278-5284.
13. Loxley, A.; Vincent, B. *J. Colloid Interface Sci.* **1998,** 208, (1), 49-62.
14. Pearson, R. G. *J. Am. Chem. Soc.* **1963,** 85, (22), 3533-9.
15. Pearson, R. G. *Proc Natl Acad Sci U S A* **1986,** 83, (22), 8440-8441.
16. Sundberg, R. J.; Martin, R. B. *Chem Rev* **1974,** 74, (4), 471-517.
17. Crabtree, R. H., *The organometallic chemistry of the transition metals*. 4th ed.; John Wiley & Sons: New York, 2005; p xiii, 546 s. : ill.
18. Jean, Y., *Molecular orbitals of transition metal complexes*. Oxford University Press: New York, 2005.
19. Vänngård, T., Copper Proteins. In *Biological applications of electron spin resonance*, Swartz, H. M.; Bolton, J. R.; Borg, D. C., Eds. John Wiley & Sons: New York, 1972.
20. Pearson, R. G. *J Am Chem Soc* **1963,** 85, (22), 3533-9.
21. Epstein, L. M.; Straub, D. K.; Maricondi, C. *Inorg Chem* **1967,** 6, (9), 1720-4.
22. Rannulu, N. S.; Amunugama, R.; Yang, Z.; Rodgers, M. T. *J Phys Chem A* **2004,** 108, (30), 6385 -6396.
23. Jones, C. J., *d- and f-block chemistry*. The Royal Society of Chemistry: Birmingham, 2001.
24. Figgis, B. N.; Hitchman, M. A., *Ligand Field Theory and Its Applications*. Wiley-VCH: Perth, 2000.
25. Holmberg, K.; Lindman, B.; Joensoon, B.; Kronberg, B., *Surfactants and Polymers in Aqueous Solution, 2nd Edition*. 2002; p 544 pp.
26. Shaw, D. J., *Introduction to Colloid and Surface Chemistry. 4th Ed.* 1992; p 288 pp.
27. Evans, D. F.; Wennerström, H., *The Colloidal Domain: Where Physics, Chemistry, Biology, and Technology Meet, 2nd.* 1998; p 640 pp.
28. Israelachvili, J. N., *Intermolecular and Surface Forces*. 2nd ed.; Academic Press: London, 1991; p 291 pp.
29. Seifert, U. *Adv. Phys.* **1997,** 46, (1), 13-137.
30. Groth, C.; Bender, J.; Nyden, M. *Colloids Surf., A* **2003,** 228, (1-3), 64-73.
31. Groth, C.; Tollgerdt, K.; Nyden, M. *Colloids Surf., A* **2006,** 281, (1-3), 23-34.

32. Mark, H.; Bikales, N.; Overberger, C.; Menges, G., *Encyclopedia of Polymer Science and Engineering*. 2nd edition ed.; John Wiley & Sons: 1989; Vol. 15 Scattering to Structural Foams, p 419-478.
33. Cowie, J. M. G., *Polymers: Chemistry & Physics of Modern Materials*. 2nd ed.; CRC Press: 1991.
34. Fleer, G. J.; Stuart, M. A. C.; Scheutjens, J. M. H. M.; Cosgrove, T.; Vincent, B., *Polymers at Interfaces*. 1993; p 502 pp.
35. Cohen Stuart, M. A.; Hofs, B.; Voets, I. K.; De Keizer, A. *Curr. Opin. Colloid Interface Sci.* **2005,** 10, (1,2), 30-36.
36. Yao, J.; Ravi, P.; Tam, K. C.; Gan, L. H. *Langmuir* **2004,** 20, (6), 2157-2163.
37. Warren, P. B. *J. Phys. II* **1997,** 7, (2), 343-361.
38. Mandel, M. *Eur. Polym. J.* **1970,** 6, (6), 807-22.
39. Leyte, J. C.; Mandel, M. *J. Polym. Sci.* **1964,** Pt. A 2, (4), 1879-91.
40. Keller, C. A.; Kasemo, B. *Biophys. J.* **1998,** 75, (3), 1397-1402.
41. Mueller, P.; Rudin, D. O.; Tien, H. T.; Wescott, W. C. *Nature (London, U. K.)* **1962,** 194, 979-80.
42. Sackmann, E. *Science* **1996,** 271, (5245), 43-8.
43. Claesson, M.; Cho, N.-J.; Frank, C. W.; Andersson, M. *Langmuir* **2010,** 26, (22), 16630-16633.
44. Reimhult, E.; Höök, F.; Kasemo, B. *Langmuir* **2003,** 19, (5), 1681-1691.
45. Richter, R.; Mukhopadhyay, A.; Brisson, A. *Biophys. J.* **2003,** 85, (5), 3035-3047.
46. Richter, R. P.; Berat, R.; Brisson, A. R. *Langmuir* **2006,** 22, (8), 3497-3505.
47. Dimitrievski, K.; Kasemo, B. *Langmuir* **2008,** 24, (8), 4077-4091.
48. Moya, S.; Donath, E.; Sukhorukov, G. B.; Auch, M.; Baeumler, H.; Lichtenfeld, H.; Moehwald, H. *Macromolecules* **2000,** 33, (12), 4538-4544.
49. Katagiri, K.; Caruso, F. *Adv. Mater. (Weinheim, Ger.)* **2005,** 17, (6), 738-743.
50. Ge, L.; Mohwald, H.; Li, J. *Biochem. Biophys. Res. Commun.* **2003,** 303, (2), 653-659.
51. Napper, D. H., *Polymeric Stabilization of Colloidal Dispersions*. Academic Press: London, 1983; p 428 pp.
52. Joanny, J. F. *Eur. Phys. J. B* **1999,** 9, (1), 117-122.
53. Van de Steeg, H. G. M.; Cohen Stuart, M. A.; De Keizer, A.; Bijsterbosch, B. H. *Langmuir* **1992,** 8, (10), 2538-46.
54. Decher, G.; Schlenoff, J. B., *Multilayer Thin Films: Sequential Assembly of Nanocomposite Materials*. Wiley: Weinheim, 2003; p 524 pp.
55. Peyratout Claire, S.; Dahne, L. *Angew Chem Int Ed Engl* **2004,** 43, (29), 3762-83.
56. Dubas, S. T.; Schlenoff, J. B. *Macromolecules* **1999,** 32, (24), 8153-8160.
57. Iler, R. K. *J. Colloid Interface Sci.* **1966,** 21, (6), 569-594.
58. Decher, G. *Science* **1997,** 277, (5330), 1232-1237.
59. Decher, G.; Lvov, Y.; Schmitt, J. *Thin Solid Films* **1994,** 244, (1-2), 772-7.
60. Bieker, P.; Schönhoff, M. *Macromolecules* **2010,** 43, (11), 5052-5059.
61. Voigt, A.; Lichtenfeld, H.; Sukhorukov, G. B.; Zastrow, H.; Donath, E.; Baeumler, H.; Moehwald, H. *Ind. Eng. Chem. Res.* **1999,** 38, (10), 4037-4043.
62. Caruso, F.; Caruso, R. A.; Moehwald, H. *Science (Washington, D. C.)* **1998,** 282, (5391), 1111-1114.
63. Donath, E.; Sukhorukov, G. B.; Caruso, F.; Davis, S. A.; Mohwald, H. *Angew. Chem., Int. Ed.* **1998,** 37, (16), 2202-2205.
64. Sukhorukov, G. B.; Donath, E.; Davis, S.; Lichtenfeld, H.; Caruso, F.; Popov, V. I.; Mohwald, H. *Polym. Adv. Technol.* **1998,** 9, (10-11), 759-767.
65. Sukhorukov, G. B.; Donath, E.; Lichtenfeld, H.; Knippel, E.; Knippel, M.; Budde, A.; Mohwald, H. *Colloids Surf., A* **1998,** 137, (1-3), 253-266.
66. Antipov, A. A.; Sukhorukov, G. B.; Donath, E.; Moehwald, H. *J. Phys. Chem. B* **2001,** 105, (12), 2281-2284.
67. Dai, Z.; Voigt, A.; Donath, E.; Mohwald, H. *Macromol. Rapid Commun.* **2001,** 22, (10), 756-762.
68. Antipov, A. A.; Sukhorukov, G. B. *Adv. Colloid Interface Sci.* **2004,** 111, (1-2), 49-61.
69. Krasemann, L.; Tieke, B. *Langmuir* **2000,** 16, (2), 287-290.

70. Krasemann, L.; Toutianoush, A.; Tieke, B. *J. Membr. Sci.* **2001,** 181, (2), 221-228.
71. Good, R. J.; Van Oss, C. J., The modern theory of contact angles and the hydrogen bond components of surface energies. In *Mod. Approaches Wettability*, 1992; pp 1-27.
72. Fowkes, F. M. *J. Phys. Chem.* **1962,** 66, 382.
73. Van Oss, C. J.; Good, R. J.; Chaudhury, M. K. *Langmuir* **1988,** 4, (4), 884-91.
74. Mohamed, A.; Trickett, K.; Chin, S. Y.; Cummings, S.; Sagisaka, M.; Hudson, L.; Nave, S.; Dyer, R.; Rogers, S. E.; Heenan, R. K.; Eastoe, J. *Langmuir* **2010,** 26, (17), 13861-13866.
75. Torza, S.; Mason, S. G. *J. Colloid Interface Sci.* **1970,** 33, (1), 67-83.
76. Trongsatitkul, T.; Budhlall, B. M. *Langmuir* **2011,** 27, (22), 13468-13480.
77. Deryagin, B.; Landau, L. *Acta Physicochim. URSS* **1941,** 14, 633-62.
78. Verwey, E. J. W.; Overbeek, J. T. G., *Theory of the Stability of Lyophobic Colloids*. 1948; p 216 pp.
79. De Gennes, P. G. *Macromolecules* **1982,** 15, (2), 492-500.
80. Scheutjens, J. M. H. M.; Fleer, G. J. *Adv. Colloid Interface Sci.* **1982,** 16, 361-80.
81. Feigin, R. I.; Napper, D. H. *J. Colloid Interface Sci.* **1980,** 75, (2), 525-41.
82. Feigin, R. I.; Napper, D. H. *J. Colloid Interface Sci.* **1980,** 74, (2), 567-71.
83. Paul D, R., Polymers in Controlled Release Technology. In *Controlled Release Polymeric Formulations*, ACS: 1976; Vol. 33, pp 1-14.
84. Florence, A. T.; Halbert, G. W. *Phys. Technol.* **1985,** 16, (4), 164-70, 176.
85. Sterky, K.; Jacobsen, H.; Jakubowicz, I.; Yarahmadi, N.; Hjertberg, T. *Eur. Polym. J.* **2010,** 46, (6), 1203-1209.
86. Masuda, M. Microencapsulation of Pesticides for Controlling Release from Coatings. Doctoral thesis, Chalmers University of Technology, Göteborg, 2011.
87. Bolton, J. R., Electron Spin Resonance. In *Biological applications of electron spin resonance*, Schwartz, H. M.; Bolton, J. R.; Borg, D. C., Eds. John Wiley & Sons: New York, 1972.
88. Campbell, I. D.; Dwek, R. A., Electron Paramagnetic Resonance Spectroscopy. In *Biological Spectroscopy*, Elias, P., Ed. The Benjamin/Cummings Publishing Company, Inc: Oxford, 1984.
89. Scholl, H. J.; Hüttermann, J. *J Phys Chem A* **1992,** 96, (24), 9684-91.
90. Kivelson, D.; Neiman, R. *J. Chem. Phys.* **1961,** 35, 149-55.
91. Berštein, V. A.; Egorov, V. M., *Differential scanning calorimetry of polymers*. Ellis Horwood Limited: Chichester, 1994.
92. Strong, A. B., *Plastics: Materials and Processing*. 3rd ed.; Pearson Education: New Jersey, 2006.
93. Fadini, A.; Schnepel, F.-M., *Vibrational spectroscopy : methods and applications*. John Wiley & Sons: Halsted, 1989.
94. Nakamoto, K., *Infrared and Raman spectra of inorganic and coordination compounds. Part A, Theory and applications in inorganic chemistry*. 6th ed.; John Wiley &Sons: Hoboken, N.J., 2009.
95. Bower, D. I.; Maddams, W. F., *The vibrational spectroscopy of polymers*. Cambridge University Press: Cambridge, 1989.
96. Pople, J. A. *Rev. Mod. Phys.* **1999,** 71, (5), 1267-1274.
97. Hehre, W. J., *A Guide to Molecular Mechanics and Quantum Chemical Calculations*. Wavefunction: Irvine, 2003.
98. Sousa, S. F.; Fernandes, P. A.; Ramos, M. J. *J. Phys. Chem. A* **2007,** 111, (42), 10439-10452.
99. Hohenberg, P.; Kohn, W. *Physical Review* **1964,** 136, (3B), B864-B871.
100. Kohn, W.; Sham, L. J. *Physical Review* **1965,** 140, (4A), A1133-A1138.
101. Becke, A. D. *J. Chem. Phys.* **1993,** 98, (7), 5648-52.
102. Lee, C.; Yang, W.; Parr, R. G. *Phys. Rev. B: Condens. Matter* **1988,** 37, (2), 785-9.
103. Hay, P. J.; Wadt, W. R. *J. Chem. Phys.* **1985,** 82, (1), 299-310.
104. Rotenberg, Y.; Boruvka, L.; Neumann, A. W. *J. Colloid Interface Sci.* **1983,** 93, (1), 169-83.
105. Shafrin, E. G.; Zisman, W. A. *The Journal of Physical Chemistry* **1960,** 64, (5), 519-524.
106. Grundke, K., Wetting, spreading and penetration. In *Handb. Appl. Surf. Colloid Chem.*, 2002; Vol. 2, pp 119-142.
107. Höök, F.; Kasemo, B.; Nylander, T.; Fant, C.; Sott, K.; Elwing, H. *Anal Chem* **2001,** 73, (24), 5796-804.

108. McCubbin, G. A.; Praporski, S.; Piantavigna, S.; Knappe, D.; Hoffmann, R.; Bowie, J. H.; Separovic, F.; Martin, L. L. *Eur. Biophys. J.* **2011,** 40, (4), 437-446.
109. Voinova, M. V.; Rodahl, M.; Jonson, M.; Kasemo, B. *Phys. Scr.* **1999,** 59, (5), 391-396.
110. Sauerbrey, G. *Z. Phys.* **1959,** 155, 206-22.
111. Andersson, M. Imidazole containing polymers complexed with Cu^{2+} and Zn^{2+}. Licentiate thesis, Chalmers University of Technology, Göteborg, 2009.
112. Su, C.-C.; Chen, J. H.; Hwang, K.-Y.; Liu, S.-J.; Wang, S.-W. *Inorganica Chimica Acta* **1992,** 196, (2), 231-40.
113. Cornilsen, B. C.; Nakamoto, K. *J Inorg Nucl Chem* **1974,** 36, (11), 2467-71.
114. Reedijk, J. *Inorg Chim Acta* **1969,** 3, (4), 517-22.
115. Perchard, C.; Novak, A. *Spectrochim Acta A Mol Biomol Spectrosc* **1970,** 26, (4), 871-81.
116. Sui, Z.; Salloum, D.; Schlenoff, J. B. *Langmuir* **2003,** 19, (6), 2491-2495.

Appendix

Table A.1. pK_a values, orbital energy levels, orbital coefficients stability constants, M-L and M-X frequencies and parameters as measured using far-FTIR, EPR and *ab initio* calculations.

				Ligands								
				Im	Me(1)-Im	Me(4)-Im	PV(1)-Im	PV(4)-Im	Histidine	NH_3	MeCN	H_2O
Ligand basicity			pK_a	6.90	6.98	7.35	4.70	5.40	6.10	9.25	-11.0[b]	-1.70[b]
			E_{H-1} [a.u.]	-0.2625	-0.2586	-0.2577						
Cu(II)	Log stability constants	Lit.	K_1	4.20		4.13	2.90		10.1	4.15		
			K_2	3.42		3.49	3.24		8.00	3.50		
			K_3	2.88		2.87	4.06			2.89		
			K_4	2.10		2.00	4.36			2.13		
			$\Delta G°$ [a]	-71.89		-71.25	-83.06		-103.3	-72.28		
		Calc.	ΔE	-522.1	-523.5	-513.9						
Zn(II)		Lit.	K_1	2.52		2.44			6.60	2.37		
			K_2	2.32		2.53			5.40	2.44		
			K_3	2.32		2.64				2.50		
			K_4	2.0		2.4				2.15		
Cu(II)	Covalence	EPR	$g_{\|\|}$	2.268	2.267	2.256	2.270				2.320	2.422
			$A_{\|\|}$ [G]	179	170	175	166				74[c]	134
			a^2	0.850	0.825	0.833						
			β^2	0.657	0.694	0.674						
		Calc.	a^2	0.71	0.71	0.71						
			β^2	0.53	0.6	0.54						
	M-L, M-X vibrations [cm^{-1}]	FTIR	Cu-N	286	282	291	<320				325	440[d]
			Cu-Cl	259	222	224, 212	<<320					
		Calc.	Cu-N	286	282	290	292, 286					
			Cu-Cl	246	211	209	246					
Zn(II)		FTIR	Zn-N	207	239	~237	<<310				214	364[e]
			Zn-Cl	-	310	303	<310					
		Calc.	Zn-N	199	196	235	235, 199					
			Zn-Cl	-	321	321						

[a]Value for pure PV(1)-Im. [b]Value for the corresponding acid. [c]From γ-radiated $CuClO_4$ crystals. [d]$[Cu(H_2O)_4]^{2+}\cdot SO_4^{2-}\cdot H_2O$. [e]$[Zn(H_2O)_6]^{2+}\cdot SO_4^{2-}\cdot H_2O$.